Effects of Spaceflight- and Clinically-relevant Ionizing Radiation Exposure on Bone Biomechanics

By

Megan Marie Pendleton

A dissertation submitted in partial satisfaction of the

requirements for the degree of

Doctor of Philosophy

in

Engineering – Mechanical Engineering

in the

Graduate Division

of the

University of California, Berkeley

Committee in charge:

Professor Tony M. Keaveny, Chair
Professor Grace D. O'Connell
Professor Jasmina L. Vujic
Doctor Joshua S. Alwood

Summer 2018

Effects of Spaceflight- and Clinically-relevant Ionizing Radiation Exposure on Bone Biomechanics

By Megan Marie Pendleton

Abstract

Effects of Spaceflight- and Clinically-relevant Ionizing Radiation Exposure on Bone Biomechanics

by

Megan Marie Pendleton

Doctor of Philosophy in Engineering – Mechanical Engineering

University of California, Berkeley

Professor Tony M. Keaveny, Chair

Bones are exposed to *in vivo* ionizing radiation exposure in applications of spaceflight, clinical radiotherapy, and *ex vivo* ionizing radiation exposure in applications of allograft sterilization. Elevated fracture risk has been shown after irradiation at the higher clinical doses, and it is uncertain if there are similar risks with exposure to spaceflight irradiation. Irradiation leads to an early loss of cancellous bone tissue and microarchitecture quality, and reduced matrix quality in the form of increased collagen crosslinks, but it is unclear which of these radiation-induced changes contribute to reduced bone mechanics. While the effects of space- and clinically-related levels of radiation on bone strength have been studied for monotonic (one-time) loading, much less is known about the effects for cyclic (repeated) loading, also referred to as fatigue. The possible increase in collagen crosslinks may have a larger effect on fatigue life by possibly impeding fibrillar sliding, reducing plasticity, and increasing the rate of microcrack growth during cyclic loading. Therefore, the goal of this research was to characterize the cyclic and monotonic mechanical properties after irradiation at spaceflight- and clinically-relevant doses, and to better understand the factors influencing the resulting mechanical behavior.

To address this, we conducted *in vivo* and *ex vivo* irradiation experiments using a murine model with a range of radiation doses, including spaceflight (≤ 2 Gy), clinically-relevant (≤ 50 Gy), and sterilization (≤ 35,000 Gy). To compare irradiated bone to healthy tissue, we performed micro-CT to analyze bone quantity and microarchitecture, biochemical assays to characterize the collagen network and material quality, and cyclic and monotonic compression testing to characterize the mechanical behavior.

To conduct cyclic mechanical testing on experimental tissue, we first developed a precise method for *ex vivo* cyclic compressive loading of isolated mouse vertebral bodies. In small animals, such as in mice and rats, cyclic loading experiments are particularly challenging to perform in a precise manner due to the small size of the bones and difficult-to-eliminate machine compliance. Our method has three main characteristics: 3D-printed support jigs for machining plano-parallel surfaces of the tiny vertebrae; pivotable loading platens to ensure uniform contact

and loading of specimen surfaces; and specimen-specific micro-CT-based finite element analysis to measure stiffness to prescribe force levels that produce the same specified level of strain for all test specimens. We found reduced scatter of the mechanical behavior for this new method compared to commonly used methods from literature. We conclude that this new method for cyclic loading of small-animal vertebrae produces highly reproducible measurements of fatigue behavior and an effective tissue elastic modulus, potentially important elements of bone quality.

To investigate effects of *in vivo* irradiation, we conducted whole-body, acute, gamma-radiation experiments on 17-week old (skeletally-mature) C57BL/6J, male mice at space- and clinically-relevant doses (1 and 5 Gy) and collected lumbar vertebrae at 11-days and 12-weeks after exposure. We found with a 5 Gy dose, short-term deficits (i.e. 11-days after exposure) in cancellous microarchitecture (-29.7% Conn.D) that persisted into the long term (i.e. 12-weeks) (-49.5% Conn.D) and led to reduced fatigue life (-15.1% cycles to failure) in the long term. Results were similar for aging alone. In contrast, short-term, irradiation-induced deficits in bone quantity (-22.3% bone volume fraction) and elevated non-enzymatic collagen crosslinks (+85.5% AGEs) did not have a significant impact on monotonic or cyclic mechanics. We conclude that degraded trabecular microarchitecture with radiation (or aging) can lead to profound deficits in cyclic mechanical properties, more so than molecular changes via collagen crosslinks or reduced bone volume fraction.

Lastly, to assess the non-cellular effects of irradiation on whole-bone and to determine the type of collagen network degradation which primarily impacts the mechanical properties, we conducted an *ex vivo* x-ray radiation experiment spanning doses from radiotherapy up to sterilization of bone allografts. Excised mouse lumbar vertebrae from 20-week old, female, C57BL/6J mice were irradiated with doses of 0, 50, 1,000, 17,000, and 35,000 Gy. We found lower collagen molecular weight at 17,000 Gy and above (≥ 74%) compared to the control, indicating collagen backbone fragmentation, which coincided with a loss in monotonic strength (≥ 50%) and cyclic mechanical properties at 17,000 Gy and above. In contrast, AGEs, representing non-enzymatic collagen crosslinks, was greater for all radiation doses (67%, 95%, 96%, and 108% for 50, 1,000, 17,000 and 35,000 Gy, respectively), but did not coincide with a reduction in strength or any other mechanical property for 50 and 1000 Gy. We conclude that mechanical properties of *ex vivo* irradiation are dominated by the direct effects of irradiation through fragmentation of the collagen backbone, and are negligibly influenced by the indirect effects of non-enzymatic crosslinks. Our findings suggest that to maintain mechanical integrity following exposure to ionizing radiation, bone allograft specimens should be sterilized at a dose below 17,000 Gy.

In summary, we have provided the field with a novel and precise methodology for fatigue testing of small animal bone. To our knowledge, this research was the first to conduct fatigue testing after radiation exposure related to spaceflight and clinical radiotherapy. Our *in vivo* irradiation results highlighted the critical role of bone microarchitecture, compared to bone quantity or collagen crosslinks, in maintaining cyclic mechanical behavior with radiation exposure and aging. Our *ex vivo* irradiation results clarified primary mechanisms of collagen fragmentation, compared to collagen crosslinks, that led to deficits in monotonic and cyclic mechanics.

To my mom, dad, and Bruce Lynn – who all, in some way, taught me to fly.

Table of Contents

ABSTRACT **1**

TABLE OF CONTENTS ..... **ii**

ACKNOWLEDGEMENTS ..... **iv**

CHAPTER 1 – Introduction **1**

1.1 Ionizing Radiation *4*

1.2 Bone Composition *6*

1.3 Bone Remodeling *8*

1.4 Bone Mechanics *9*

1.5 Objectives *11*

CHAPTER 2 – High-Precision Method for Cyclic Loading of Small-Animal Vertebrae to Assess Bone Quality **12**

2.1 Introduction *12*

2.2 Materials and Methods *12*

2.3 Results *18*

2.4 Discussion *20*

2.5 Supplemental Material *22*

CHAPTER 3 – Short- and Long-term Effects of *in vivo* Ionizing Radiation Exposure on Monotonic and Cyclic Loading Strength of Mouse Vertebrae **24**

3.1 Introduction *24*

3.2 Materials and Methods *24*

3.3 Results *27*

3.4 Discussion *32*

3.5 Supplemental Material *35*

CHAPTER 4 – Effects of *ex vivo* Ionizing Radiation Exposure on Collagen Structure and Mechanical Properties of Mouse Vertebrae **38**

4.1 Introduction *38*

4.2 Materials and Methods *39*

4.3 Results *42*

4.4 Discussion *46*

4.5 Supplemental Material *49*

CHAPTER 5 – Conclusions 51
REFERENCES 54
APPENDIX A – Supplemental Figures & Tables 65
APPENDIX B – Standard Operating Procedures & Engineering Drawings 76

Acknowledgments

My dad used to call me his “Little Mad Scientist” when I was just a 6-month old baby with some crazy Einstein-hair; who knew, 29-years later, it would become true. But, it would have not been possible without the numerous professors, mentors, lab mates, friends, and family that have supported me along the way. This PhD journey has been the most rewarding and epic adventure of my life thus far, and I am forever grateful that my life has been touched by theirs.

To my advisor and mentor, Tony Keaveny: First, thank you for introducing me to the world of bone. In one of your first lectures in Orthopaedic Biomechanics, you spoke about the remarkable properties of bone: “Did you know, you have a completely new skeleton every 7-10 years?!” I was hooked. Joining your lab set me along a trajectory I could have never predicted, and forever changed my life and career for the best. Second, thank you for passing along your impeccable data analysis and technical writing skills (I’ll keep working to improve mine!) And lastly, thank you for your support in my pursuit of a research topic that I was truly passionate about. Your continued encouragement and willingness to help is what made this research possible.

To my co-advisor and mentor, Grace O’Connell: Thank you for being an exemplarily role model for women in engineering. Your immense success as a Berkeley professor are a testament to your work ethic and creative research ideas. I cannot wait to see the impact your work will have on the medical community!

To my NASA mentors, Josh Alwood and Jean Sibonga: Thank you both for providing the framework and resources to conduct this dissertation research. Josh – this dissertation would not have been possible without you. Thank you for taking a chance on me, welcoming me into your lab, and teaching me numerous technical skills in animal handling and radiation research. I am incredibly grateful for my time at NASA Ames under your tutelage. Jean – thank you for introducing me to the exciting field of spaceflight radiation research in the first place and always helping me keep sight of the big picture with respect to astronaut health. You have been a wonderful and encouraging NSTRF mentor.

To my other Berkeley professors, Lisa Pruitt, Jasmina Vujic, Alice Agogino, and Tom Carlson: UC Berkeley is a world-renowned (and special) university because of smart and dedicated professors like yourselves. Thank you for taking the time to teach me in class and serve as members of my qualifying exam and dissertation committees.

To the NASA Science and Technology Research Fellowship (NSTRF) NNX14AM56H: Thank you for funding my education and research. I am so grateful to have been granted the opportunity to conduct research I am passionate about and contribute to our collective goal of putting humankind’s first footsteps on Mars.

To my research collaborators at UCSF, Washington University in St. Louis, LBNL, and industry (Alfred Li, Tamara Alliston, Simon Tang, Jennifer Liu, Dula Parkinson, and Elumalai Rangasamy): Your mentorship, training, and hard work were such an integral part of this dissertation research. Thank you for your dedication and effort! Also thank you to Tongge Wu for carrying on this research from a computation perspective, I am excited to see where it goes!

To my lab mates/collaborators/best friends, Saghi and Shannon: I cannot imagine Berkeley without you two. Not everyone gets to the end of their PhD journey with lab mates that have become life-long best friends, so I consider myself extremely blessed. Saghi – thank you for providing your computational expertise to this research. The novelty of the methods would not have been possible without you. Thank you for our Menchie's breaks, strolls around campus, and all your life advice; you are wise beyond your years. Shannon – thank you for the *tremendous* amount of time and effort you dedicated to the *ex vivo* irradiation study, all of Chapter 4 would not exist without your work. Thank you for sticking out those late nights of LBNL and bone crushing with my country playlist on repeat; the sign of a true friend. You will make an inspirational and revered professor someday. I look forward to seeing the wildly successful careers that unfold for you both. I will miss you every day across the bay.

To all my other lab mates (and PIs) in Berkeley Biomechanics Lab (Tonnge, Noah, Jonathan, Annie, Bo, Semih, Ben, Minhao, Gabriel, Emily, Farzana, Louis, Audrey, and Sofia) and the Bone and Signaling Lab at NASA Ames (Ruth, Eduardo, Candice, Ann-Sofie, Yasaman, Liz, Masahiro, Ryan, Nick, Catherine, Meg, Luan, Eric, Sam, and Sonette): I am thankful for the memories I have made in these labs that involve each and every one of you. In particular, Bo – thank you for being my scuba diving buddy, and an inspiring friend, whose work ethic is unparalleled. Thank you for keeping me company in lab during late lab nights. Ryan – thank you for your friendship, overall wealth of knowledge (i.e. in anatomy, bone, music, etc.), and for always encouraging your peers, students, and friends to "talk science".

To my roommates in Berkeley (Romain, Jasmine, and Doug) and in Santa Clara (Brian and Vivian): Thank you for the wonderful memories I have from our little house on the hill, and cooking such good food! Also, Brian and Vivian – thank you for sharing your home with me and my trusty duffle bag. You saved me many hours of commuting and traffic rants, so thank you!

To Michael: I will never meet a more patient, kind-hearted, and selfless person in my whole life. Thank you for teaching me to "sit-down and look at the sample under the light" before giving up. Your advice saved my biochem-related research, and also turned out to be very applicable to life in general. You also are wise beyond your years. Thank you for runs out by the Marina, dinners at Lo Coco's, and making Berkeley home with me.

And lastly, to my family: Thank you for providing all the opportunities I had to learn and grow as a kid (i.e. pitching lessons, piano lessons, flying lessons, science fair, club volleyball), so that I could make it to this point. Emily – thank you for being my sister and my support network, it is comforting to have a sister that can sympathize with late nights and hard work throughout her own schooling and job. Mom – from a humble, migrant-worker to first-college-graduate of her family, you taught me I can be anything I want to be. I am here because of you, so thank you. Dad – my earliest memories are of you handing me some chalk or a dry-erase marker in a classroom at UT, so I can scribble on the board while you studied for your masters, my first taste of academia. You are the reason I am an engineer, a scientist, and now a PhD. Thank you for encouraging me to always "follow my bliss".

Chapter 1 – Introduction

Human exposure to high doses of ionizing radiation is found in applications of spaceflight and clinical therapies. First, for spaceflight, astronauts on a deep-space mission to the moon or Mars will travel beyond the Earth's protective magnetic field and be exposed to ionizing radiation from solar (i.e. the sun) and cosmic (i.e. the universe) sources (**Figure 1.1**). Second, for clinical therapy applications, ionizing radiation is used in radiotherapy to treat patients with cancer (**Figure 1.2**).

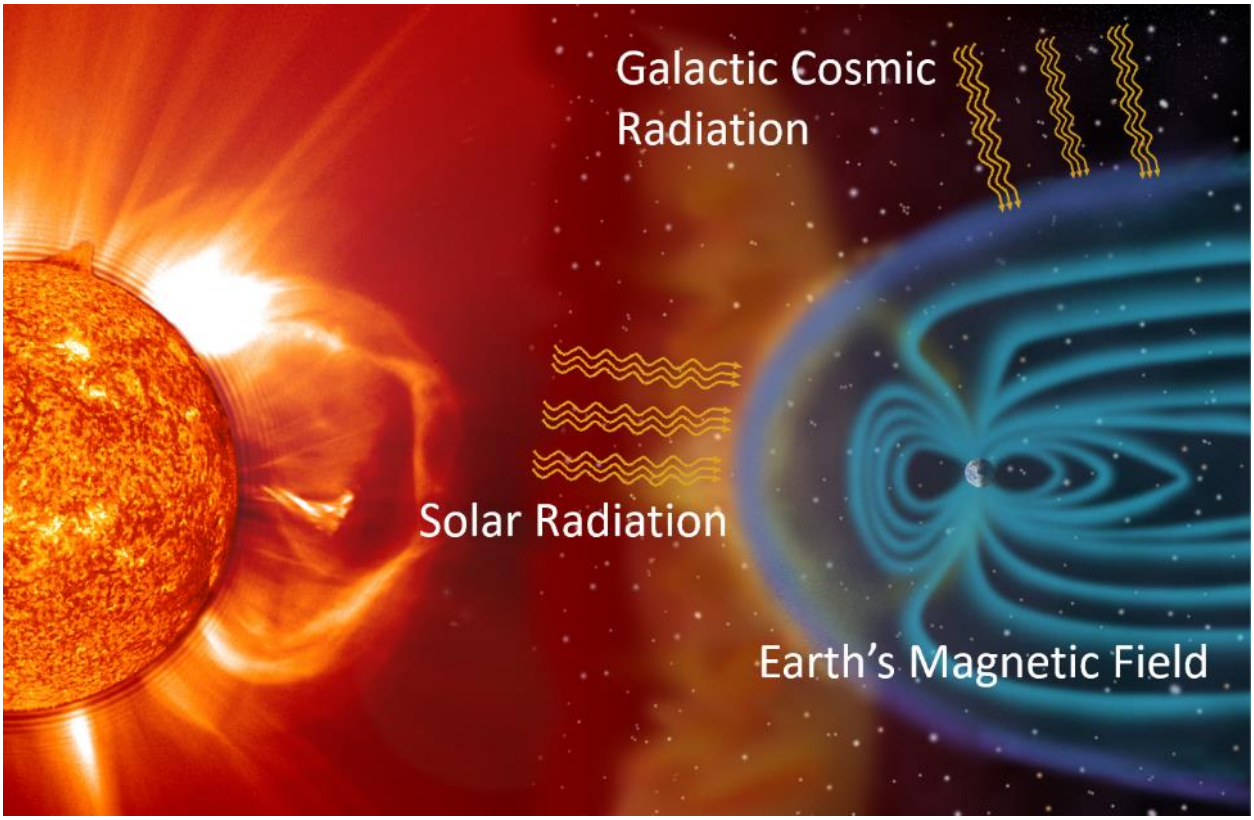

Figure 1.1 – Sources of ionizing radiation in spaceflight, outside the Earth's magnetic field. (Adapted from Steele Hill / NASA).

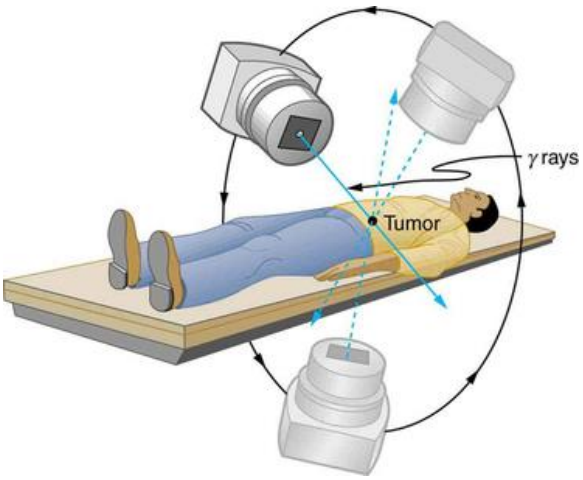

Figure 1.2 – Ionizing radiation exposure through radiotherapy treatment for cancer. (electromagneticspectrumscience.weebly.com)

There is evidence that exposure to these high doses of ionizing radiation is harmful to bone and leads to increased risk of fracture (Baxter et al. 2005; Okoukoni et al. 2017; Bazire et al. 2017). For example, with radiotherapy, x-rays or gamma-rays are localized to the area of cancerous tissue. However, in some cases, the radiation exposure to the surrounding tissue cannot be avoided. Baxter et al. (Baxter et al. 2005) reported that patients treated with radiotherapy for cervical, rectal, or anal cancer were up to 3.2-times more likely to suffer a pelvic fracture than patients treated with an alternative option, such as chemotherapy. Furthermore, a positive correlation between the magnitude of radiation received and risk of fracture has been observed in the rib cage with treatment of breast cancer (Overgaard 1988).

The elevated fracture risk observed with radiotherapy has prompted concern for risk of bone exposed to spaceflight radiation. With radiotherapy, the retrospective population studies of thousands of cancer patients led to our knowledge of elevated fracture risk, but for spaceflight we have very few data. In fact, the only data we have from a deep-space mission, outside the Earth's magnetic field, is from the lunar Apollo missions (9 manned-missions to the moon for a total of 27 astronauts). The longest and most recent of which was Apollo 17, which flew in 1972 and lasted a total of 12-days. Therefore, to collect more data for the purposes of understanding fracture risk with spaceflight, and bone mechanical properties in both spaceflight and clinical therapy applications, researchers have used animal models to investigate the effects of irradiation on bone.

Numerous studies, have investigated the effects of both spaceflight and clinically-relevant radiation exposure on bone using a murine (i.e. mouse or rat) animal model. In brief, these studies, discovered significant losses of trabecular bone and changes in the trabecular microarchitecture shortly (i.e. within days) after radiation exposure (Hamilton et al. 2006; Kondo et al. 2009; Willey et al. 2011a; Alwood et al. 2012; Green et al. 2013). Additionally, for clinically-relevant levels of radiation exposure, they found evidence of changes in the collagen network with increased levels of collagen crosslinks (Akkus and Belaney 2005; Gong et al.

2013; Oest and Damron 2014; Oest et al. 2016). It is unknown if spaceflight-relevant irradiation effects the collagen network in the same way.

Interestingly, these changes with irradiation did not yield a significant difference in strength or stiffness when tested mechanically, in monotonic compression (i.e. loaded once to failure) (Kondo et al. 2009). However, other modalities of failure, specifically fatigue (i.e. cyclic loading to failure), have yet to be investigated for either spaceflight or clinical applications. Understanding the response for cyclic loading is important because of the evidence of increased collagen crosslinks at the molecular level after radiation exposure. While structural changes to the collagen network typically only have a small effect on monotonic properties such as elastic modulus and yield stress (Currey et al. 1997; Zioupos, Currey, and Hamer 1999), these changes may have a larger effect on fatigue life. For example, if collagen crosslinking impedes fibrillar sliding, this may lead to reduced plasticity and increased rate of microcrack growth during cyclic loading (Acevedo et al. 2015). This mechanism can be observed in cyclic mechanics for other materials besides bone. For example, in polymer implants sterilized with radiation there is a dose-dependent increase in polymer chain crosslinks, this increase in crosslinks coincides with increased rate of crack propagation when loaded in fatigue (Baker, Bellare, and Pruitt 2003).

Therefore, the goal of this dissertation was to better understand the cyclic and monotonic mechanical properties of bone after exposure to radiation for spaceflight and clinically-relevant doses. Furthermore, we sought to better understand the underlying matrix mechanisms by which the mechanics can be altered.

This research is important because it contributes to the on-going effort to safely send human-occupied missions to the Mars or lunar surface. There are numerous challenges we will have to overcome to get there, one of which is mitigating risks of radiation exposure for human health. Radiation research across all physiological systems (e.g. skeletal, cardiovascular, neurological, etc.) is being conducted all over the world to evaluate the risk of irradiation on these systems. Skeletal health for the astronauts is critical for mission success in the short term and quality of life in the long term. Therefore, we have conducted this work to add to the body of knowledge on bone mechanics after radiation exposure, which hopefully will aid in fracture risk assessment, and also help guide in decisions and development of future countermeasures.

Furthermore, this research is also important because it contributes to the effort of improving quality of life for cancer survivors. As cancer survival rates increase (Miller et al. 2016), there will be greater concern for side-effects that affect the patient's quality of life after treatment, such as elevated fracture risk in the hip after radiotherapy for certain cancers (i.e. cervical, anal, or rectal). Hip fractures, in particular, are associated with "morbidity, mortality, loss of independence, and financial burden" for patients (≥ 65 years old) (Schnell et al. 2010). For example, reports estimate the mortality rate to be 1 in 3 people within 1-year post-hip fracture (Brauer et al. 2009; Roche et al. 2005; Bentler et al. 2009). This research contributes to better understanding of the underlying mechanisms in the bone that are affected by radiation exposure and will allow for future researchers to target appropriate mechanisms for countermeasures.

The remaining sections of this chapter aim to provide the reader with enough background information to understand the following research presented in the dissertation. First, an overview of what ionizing radiation is, and the key differences between radiation exposure from spaceflight versus clinical therapy exposure. Second and third, a description of bone composition followed by cellular bone remodeling. Fourth, a section on bone mechanics and testing for mechanical properties of bone, specifically fatigue testing. Lastly, a brief overview of the research objectives presented in the following chapters. Textbook references are listed at the bottom of each section for supplemental reading.

1.1 Ionizing Radiation

Ionizing radiation is radiation with enough energy to ionize an atom (i.e. remove an electron from an atom). Examples of ionizing radiation include: x-rays, gamma-rays, and high-energy particles such as electrons, protons, neutrons, heavy ions, or atomic nuclei (e.g. helium, iron, silicon, or titanium nuclei). Non-ionizing radiation does not have the energy level necessary to ionize an atom. Examples include: radio-waves, microwaves, visible light, and ultraviolet light (**Figure 1.3).**

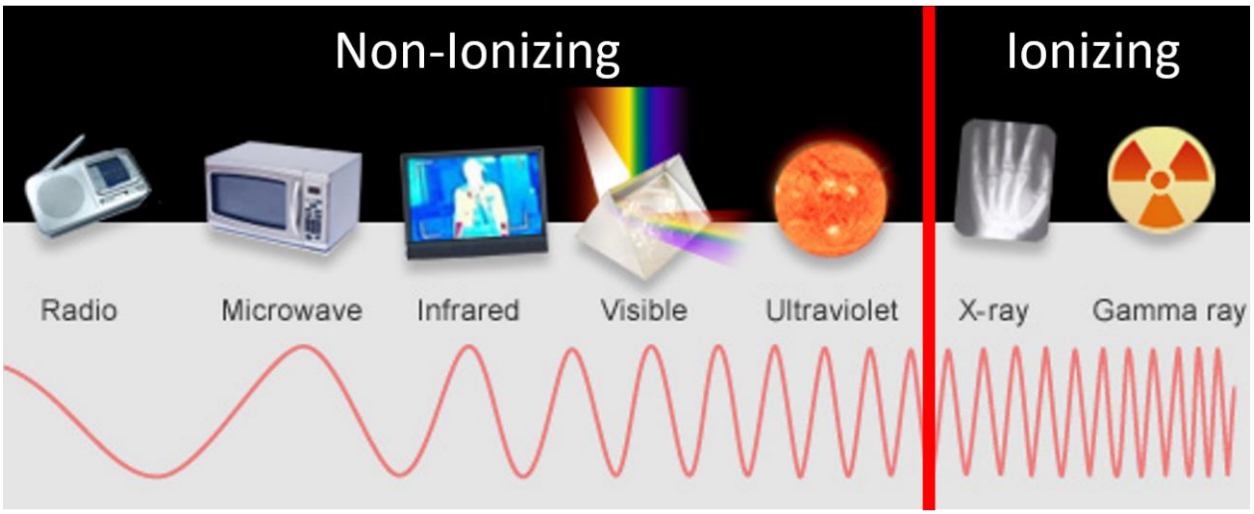

Figure 1.3 – Examples of non-ionizing and ionizing radiation. (Adapted from ABC Science author Bernie Hobbs).

Ionizing radiation exposure can be harmful to the human body because it can lead to cellular and protein damage in our tissues. There are two categories of damage: direct effects and indirect effects. First, the direct effects of ionizing radiation refer to direct energy transfer from radiation to biologically important molecules, that directly breaks molecular bonds of protein and DNA. For example, if ionizing radiation breaks through the bonds of DNA and the cell divides quickly, the DNA error can be propagated to the next cell, which could result in abnormal protein and cellular function. Second, the indirect effects of radiation refer to energy transfer that creates highly unstable and reactive species (chemical radicals) that effect protein and DNA. For example, radiolysis of water in the body's tissues produce highly reactive water molecule-based

species. These reactive molecules can bond two nominally independent proteins together, which could again result in abnormal protein and cellular function.

Ionizing radiation can further be classified by its ability to deposit energy in tissue, referred to as linear energy transfer (LET). High-LET radiation compared to low-LET radiation, deposits more energy per unit distance in tissue, and thus can generally do more harm to tissue cells and proteins. LET depends on the type of particle (i.e. mass and charge), the initial energy of the particle, and the medium the particle is passing through (i.e. mostly water for human tissue). Photons which have no mass and no charge, such as x-rays and gamma-rays, are always considered low-LET radiation. Charged particles, especially those with high atomic numbers (e.g. iron nuclei) are considered high-LET. For our experiments presented in the following chapters, only low-LET radiation in the form of x-rays and gamma-rays was used. However, it is an important distinction because clinical therapies generally use low-LET radiation, but the spaceflight-environment contains both low and high-LET radiation.

There are some key differences between the ionizing radiation exposure found in spaceflight and radiotherapy applications, which are important to know for discussions in later chapters. First, for deep spaceflight, astronauts will receive a whole-body dose of 1-2 Gy per year, from solar or cosmic sources (Bandstra et al. 2009; Willey et al. 2011a; National Council on Radiation Protection and Measurements. 2000), which is estimated accounting for spacecraft shielding. This radiation is comprised mostly of high-LET particles (~80% proton, also heavy-nuclei such as helium, iron, silicon, and titanium nuclei), plus low-LET radiation that is generated when particles interact with spacecraft shielding and slow down, generating bremsstrahlung, or "breaking radiation", in the form of x-rays (Turner 2007). The radiation exposure will be chronic, accumulated exposure over months of travel, or within hours in the case of solar storm. Second, for radiotherapy, patients receive a localized dose of 2 Gy per day (5-day week) for 5 weeks, for a total of ~50 Gy, and surrounding tissues can receive up to half of this dose (Willey et al. 2011a). This radiation is comprised of low-LET radiation, typically in the form of x-rays. The exposure is acute (i.e. one-time exposure within minutes).

An absorbed dose (or dose in this dissertation) of radiation describes the amount of energy deposited by radiation exposure in the tissue in Joules per kilogram, referred to as a "gray" (1 J/kg = 1 Gy). A dose can also be described as a "dose equivalent" which scales the dose by a quality factor that is based upon the properties of the particular type and energy of radiation. A dose equivalent still has units of Joules per kilogram, but is referred to as a "sievert" (Sv). Photon radiation such as x-rays or gamma-rays, have a quality factor of 1, therefore gray is the same as sievert.

For context, here are some examples of dose and dose equivalents that humans can receive in their daily lives. Humans receive 2 to 6 mSv from natural background radiation each year (2 mSv for populations living at sea level and up to 6 mSv for locations at higher elevations). Passengers on a flight from New York to Tokyo at 30,000 feet receive about 0.5 mSv. Many medical diagnostic tools use ionizing radiation, but the dose is quite small. For

example, a chest x-ray is 0.0001 Gy and an abdominal-CT scan is 0.01 Gy. Thus, one-year of deep-spaceflight is equivalent to 100-200 abdominal-CT scans.

Supplemental Reading: *Atoms, Radiation, and Radiation Protection* by James E. Turner (Turner 2007)

1.2 Bone Composition

Bone is a composite material made of approximately: 60% inorganic (i.e. mineral) content, 30% organic (i.e. protein) content, and 10% water measured by mass. The mineral component is mostly an impure form of calcium phosphate, called "hydroxyapatite" - $Ca_{10}(PO4)_6(OH)_2$. The protein component is mostly type-I collagen, but also a small percentage of cells and non-collagenous proteins (e.g. osteopontin, osteocalcin, and osteoectin). The last component is water, and it can be broken into categories of bound and un-bound water.

The structure of these components at the molecular level is organized with collagen as a scaffold base with mineral crystals deposited within and between collagen fibrils. At the most basic level, collagen alpha chains are a polypeptide of ~1000 amino acids, repeating the sequence glycine-proline-X, where X is often hydroxyproline. Three alpha chains (two alpha-1 chains plus one alpha-2 chain) twist together in a triple-helix shape to form a tropocollagen molecule (300 nm long; 1.5 nm diameter). Alpha-1 and alpha-2 differ slightly in the number and types of amino acids that comprise the chain. Tropocollagen molecules (200 to 800) then align end-to-end and next to each other (with small gaps) to form a collagen fibril (20-40 nm diameter). Crosslinks at the end of tropocollagen molecules bind enzymatically with a neighboring tropocollagen molecule, which help hold the fibril together (**Figure 1.4**). The hydroxyapatite crystals (~3 x 15 x 30 nm plates) attach to the tropocollagen molecules with non-collagenous proteins such as osteopontin acting as an adhesive. Lastly, water molecules bind to the hydroxyl-groups of hydroxyproline and hydroxyapatite. Progressing towards the macro-level the collagen fibrils arrange to form thin sheets of bone called lamellae that stack together in a hierarchical fashion to form the more macro-level of bone. (Bartel, Davy, and Keaveny 2006)

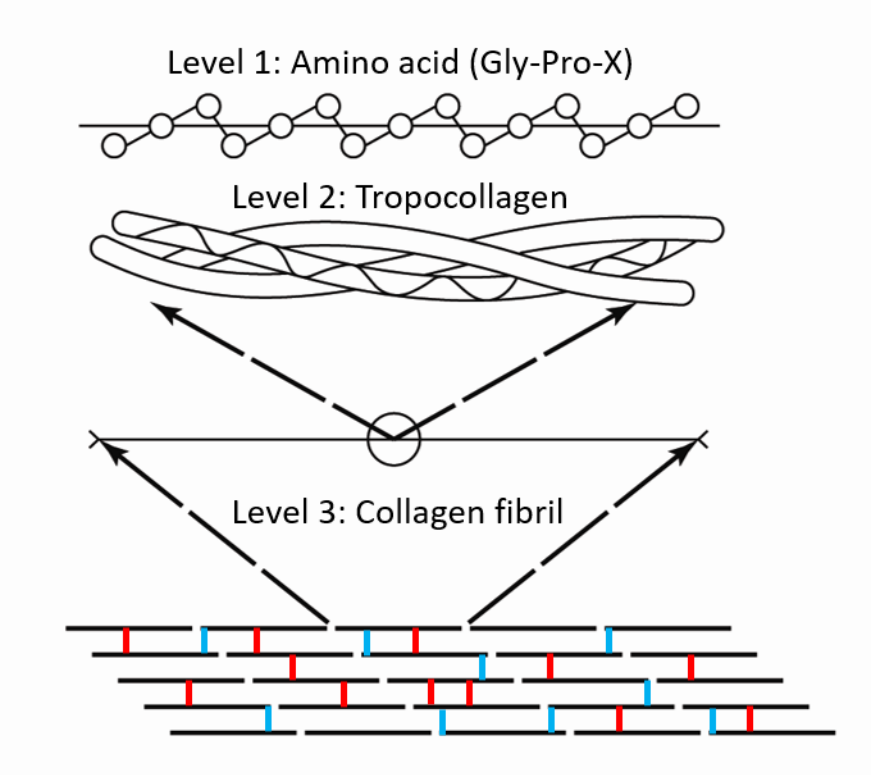

Figure 1.4 – Diagram representing the molecular structure of a collagen fibril. Individual chains of collagen are polypeptides made of repeating sequence of amino acids, glycine-proline-X. Three alpha chains twist together to form a tropocollagen molecule. The tropocollagen molecules stack end-to-end and radially to form a collagen fibril. Enzymatic collagen crosslinks are shown in blue, Non-enzymatic collagen crosslinks are shown in red. (Adapted from (Bartel, Davy, and Keaveny 2006)).

At the macro-level there are two types of bones: cortical bone (i.e. compact bone) and trabecular or cancellous bone (i.e. spongy bone). Cortical bone is the densely compact bone that is found primarily in the diaphysis of long bones. Human cortical bone has osteons, which are structures of circumferential layers of lamellae around a canal which allows for blood vessels to reach the inside of the bone to supply nutrients to the bone cells. In smaller animals, such as mice, the cortical bone is too small to have osteons. In contrast, trabecular bone is a porous, "spongy" looking structure made of connected rods, struts, and plates. This type of bone is found at the ends of the long bones and inside the vertebrae, surrounded by a shell of cortical bone. Trabecular bone does not have full osteons because the rods and struts are too small to contain a full osteon, and the blood vessels wind their way through the spongy structure to supply nutrients to the bone cells. Thus, trabecular and cortical bone differ significantly in microarchitecture, but are mostly the same material at the molecular level. Our mechanical testing utilizes the mouse vertebral body, which is composed of both types of bone: a trabecular core and surrounding cortical shell.

The material quality of bone plays an important role in bone mechanical properties, as is discussed further in Section 1.4 Bone Mechanics, therefore it is important to understand how bone can be altered by irradiation at the molecular level. The mineral component, as measured

by micro-CT, appears to be unaffected by irradiation (Pendleton et al. 2018B, Chapter 3), however there is evidence that the collagen network can be altered (Akkus and Belaney 2005; Gong et al. 2013; Oest and Damron 2014). Both direct and indirect effects of radiation exposure have been shown to impact the collagen structure. Direct effects of radiation break bonds in the polypeptide alpha chains, fragmenting the collagen into smaller molecular weight chains. Indirect effects of radiation cause radiolysis of water and these highly reactive molecules combine with collagen chains to form non-enzymatic collagen crosslinks (Barth et al. 2010; Nguyen, Morgan, and Forwood 2007; Akkus and Belaney 2005).

Supplemental Readings: (1) *Orthopaedic Biomechanics* by David Bartel, Dwight Davy, & Tony Keaveny (Bartel, Davy, and Keaveny 2006) (2) *Basic and Applied Bone Biology* by David Burr and Matthew Allen (Burr and Allen 2013).

1.3 Bone Remodeling

Bone is one of the most extraordinary structural materials in the world, not only because it can heal itself after fracture, but it can also adapt and optimize itself for its mechanical environment. The bone can sense a mechanical stimulus, or lack of mechanical stimulus, and add or remove bone as needed to make the best possible structure, this process is referred to as bone remodeling.

Bone remodeling is conducted by three types of bone cells that each play a key role in the process: (1) osteoclasts remove bone, (2) osteoblasts add/replace bone, and (3) osteocytes sense stimuli and signal activation of bone remodeling. When osteoclast and osteoblast activity are balanced, the bone mass remains constant. When osteoblasts are elevated compared to osteoclasts, the bone mass increases, and when osteoclasts are elevated compared to osteoblasts, the bone mass decreases. To resorb bone, osteoclasts form a tight seal on the bone surface and deposit an acid that digests the collagen releases the mineral crystals from the collagen scaffold. To add bone, osteoblasts deposit new collagen, called osteoid, that becomes mineralized overtime. Some osteoblasts become embedded within the bone as they produce osteoid and differentiate into osteocytes which are permanent bone cells. Osteocytes are thought to be the sensors for a mechanical stimulus, such as strain, which can then send a chemical signal to osteoclasts and osteoblasts when the strain is too high or too low (Taylor et al. 2007).

The bone quantity and structure depend upon the mechanical environment and adapt to changes in this mechanical environment. Similar to other controlled systems and homeostatic setpoints in the body (e.g. blood pressure, temperature, or glucose levels), the bone is also attempting to maintain a specific reference value (i.e. setpoint), possibly a specified level of strain sensed by the residing osteocytes (Taylor et al. 2007). When the mechanical load applied to the bone increases or decreases, the resulting strain is above or below the desired setpoint. To return to the setpoint, the bone will remodel to add and remove tissue as needed. A couple of examples illustrate this phenomenon. First, increased mechanical loading occurs in the dominant-upper-arm (i.e. the racket arm) of professional tennis players. X-rays of each forearm

have shown the dominant upper-arm has greater bone mass and a larger diameter compared to their contralateral upper-arm (Ireland et al. 2013). In contrast, decreased mechanical loading occurs in astronauts who experience weightlessness in the space environment. The lack of mechanical stimulus decreases the resulting strain sensed by the skeleton, and bone mass is resorbed (LeBlanc et al. 2000).

Bone remodeling is an ongoing process, gradually replacing old bone with new bone each day. When the mechanical environment remains relatively constant, the osteoclast and osteoblast activity are in balance, and therefore bone mass and architecture remain the same. However, there are diseases where the cellular activity becomes unbalanced and bone loss occurs, not as a result of mechanical unloading. For example, osteoporosis is a bone disease where osteoclast activity is elevated compared to the osteoblasts (Riggs and Melton 1986). The resulting loss of bone quantity and microarchitecture reduces the strength of bone and places the patient at a greater risk for fracture. There are drug treatments for osteoporosis, known as bisphosphonates or anti-resorptives (Russell et al. 1999; McClung et al. 2005). They act by shutting down the remodeling process primarily by stopping osteoclast activity. Bisphosphonates allow for the patient to retain bone mass and microarchitecture. However, without active resorption, bone may continue to accumulate microdamage and microcracks from daily loading activities (e.g. lifting groceries or going for a jog). Therefore, long-term use of bisphosphonates may impact the quality of the bone material and resulting mechanics of the bone (Odvina et al. 2005; Goh et al. 2007; Lenart, Lorich, and Lane 2008; Benhamou 2007). Currently, astronauts are also given a bisphosphonate treatment as a countermeasure for bone loss due to weightlessness (Leblanc et al. 2013).

Supplemental Reading*: Basic and Applied Bone Biology* by David Burr and Matthew Allen (Burr and Allen 2013).

1.4 Bone Mechanics

Bone mechanics refers to the behavior of bone measured through mechanical testing, or rather mechanical properties of bone. Testing for mechanical properties of bone is important because it provides insight into fracture risk. Fracture risk may be elevated if the mechanical properties of a treated bone are lower compared to the healthy control. Various mechanical properties can be measured to characterize the mechanical behavior of bone. For example: stiffness, strength, toughness, and ductility are measured from monotonic testing of bone (loaded once to failure). Fatigue strength, fatigue life and strain-to-failure are additional parameters measured from fatigue testing (cyclic loading to failure). These tests can be conducted in various loading configurations such as tension, compression, or bending, and will have different results in bone because it is an asymmetric material (i.e. is stronger in compression than tension). However, for the upcoming studies, we have focused on compression testing, because this most closely mimics the *in vivo* loading condition of the vertebra.

Fatigue, or cyclic testing is an integral part of this work and warrants a more in-depth explanation. A fatigue test is a mechanical test which applies force to a material repetitively and

tracks the number of loading cycles to failure, called the "fatigue life". The cyclic force applied is a percentage of the ultimate force (e.g. 50% of F_{ult}) the material can withstand in monotonic loading. As the bone is loaded, a combination of creep (i.e. deformation that occurs over time with a constant force) and damage (i.e. microcrack accumulation) occur (Bowman et al. 1998). There are three phases of the test which can be seen on a plot of strain per cycle (**Figure 1.5 A**). During the primary phase cracks initiate, in the secondary phase (the longest phase) cracks gradually grow, and in the third phase the cracks coalescence which leads to failure (Turner and Burr 1993). With enough specimens tested at various levels of cyclic force (or stress), an S-N curve can be plotted (**Figure 1.5 B**). For all materials, the S-N curve has a negative slope; the larger the applied stress (or force), the less number of cycles to failure. However, different materials exhibit varying S-N slopes, depending on their ability to withstand crack initiation and crack propagation. In our studies, we did not define an S-N curve for bone, but rather tested at one force level on the y-axis to see if the fatigue life was different between irradiated and healthy tissue. Fatigue testing is quite time consuming, with larger scatter in the data (Suresh 1998) which make it a challenging test, and not often performed. Nevertheless, fatigue testing is important to evaluate for two reasons. First, cyclic mechanical properties, such as fatigue life, provide insight into rate of crack propagation within the material. Second, cyclic loading can lead to unexpected catastrophic failure at forces well below the nominal strength of the material.

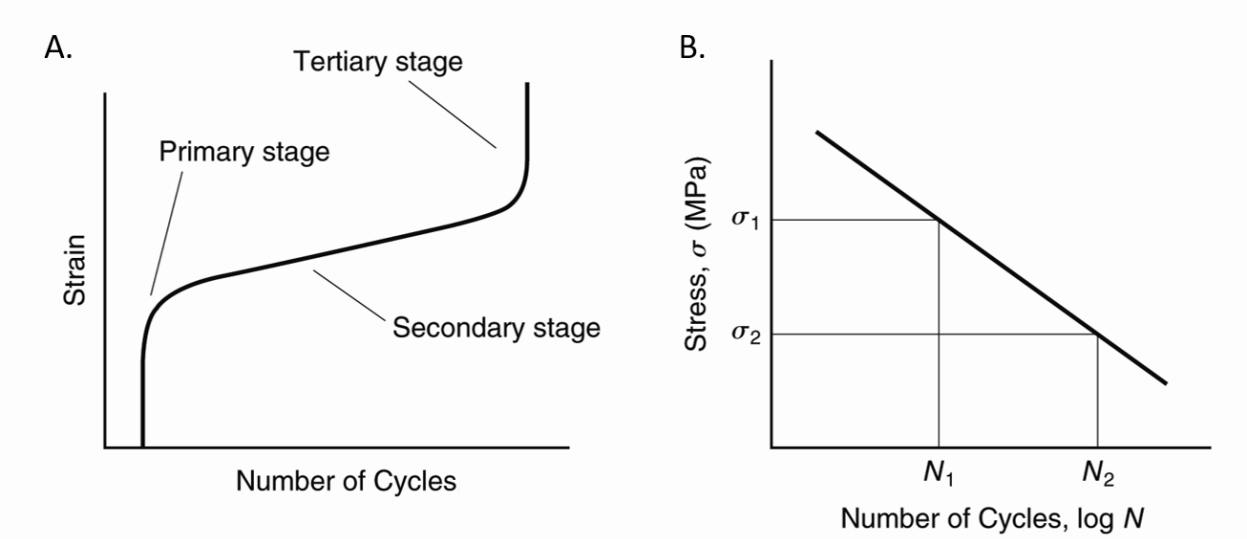

Figure 1.5 – (A) Typical tertiary plot of strain per cycle generated from fatigue testing of bone. Failure occurs in the tertiary region when the sample can no longer hold the applied load and has a large increase in strain. (B) S-N curve generated for a material from testing of many samples at varying stress levels. The slope will depend on the ability of the material to withstand crack initiation and crack propagation. (Adapted from (Bartel, Davy, and Keaveny 2006)).

Mechanical properties of bone are influenced by characteristics such as bone mass, microarchitecture, and material quality (Hernandez and Keaveny 2006; Watts 2002). A couple of examples highlight the importance of these factors. First, reduced bone mass and microarchitecture with osteoporosis lead to lower bone strength and thus more fracture incidents if left untreated. Second, reduced material quality can also lead to more fracture incidents. In the early 1990s a sodium fluoride drug was given as a treatment for osteoporosis to increase bone

mass. However, by only adding mineral to the bone they embrittled the tissue, reducing its strength and ductility (Riggs et al. 1990; Sogaard et al. 1994). Therefore, differences in these characteristics compared to healthy bone tissue can result in degraded bone mechanics. If mechanical properties are reduced, it is important to identify which of these factor(s) are the root cause in order to appropriately target a countermeasure, which is a major goal of this study with respect to irradiation.

Supplemental Reading: *Orthopaedic Biomechanics* by David Bartel, Dwight Davy, & Tony Keaveny (Bartel, Davy, and Keaveny 2006).

1.5 Objectives

The overall goal of this dissertation was to better understand the cyclic and monotonic mechanical properties of bone after exposure to radiation for spaceflight and clinically-relevant doses, and identify the underlying mechanisms influencing the resulting bone mechanics. Each of the upcoming chapters addressed specific objectives which contribute to the main goal.

The objective of Chapter 2 was to outline a novel methodology for fatigue testing of mouse vertebrae in a precise fashion, which was utilized later for mechanical testing of irradiated tissue in Chapters 3 and 4. Methods for fatigue testing commonly used in bone literature were not effective applied to the tiny mouse vertebrae because of the challenges with machine compliance errors. This chapter details key aspects of our new method which use 3D printing for precise specimen preparation, adjustable loading platens, and micro-CT-based finite element analysis to prescribe individualized cyclic force levels per specimen to reduce scatter in the data. We also compare our new fatigue methodology to two others found in the literature by testing all three methods with healthy mouse vertebrae.

Chapter 3 focuses on the short-term and long-term effects of *in vivo* irradiation on mechanical and biochemical properties of bone for both spaceflight and clinically-relevant doses. We analyze the results from micro-CT imaging, cyclic and monotonic mechanical testing, and biochemical testing of the collagen. We discuss the contribution of factors such as bone mass, material quality and microarchitecture quality on the resulting bone mechanics, and the implications these have for spaceflight and clinical treatment.

The objective of Chapter 4 was to identify the non-cellular effects of irradiation. Thus, we present a study on the effects of *ex vivo* irradiation across a range of doses from radiotherapy (50 Gy) to allograft sterilization (35,000 Gy). We discuss the major changes to the collagen network that influence the mechanics.

Lastly, Chapter 5 concludes with a summary of the important findings from each of the studies and their implications to the spaceflight and clinical communities. Also, a brief discussion on possible directions of related future work.

Chapter 2 – High-Precision Method for Cyclic Loading of Small-Animal Vertebrae to Assess Bone Quality[1]

2.1 Introduction

A number of diseases, including osteoporosis (Bouxsein 2003b; Saito and Marumo 2010) and Type II diabetes (Janghorbani et al. 2007; Vestergaard 2007; Farr and Khosla 2016; Rubin and Patsch 2016), are thought to increase fracture risk due, in part, to deteriorated bone quality. That is, these diseases result in detrimental changes to mechanical behavior that are not directly associated with reductions in bone mass (Hernandez and Keaveny 2006). Changes in bone quality also present potential issues with drug treatments for osteoporosis, causing the FDA to require extensive pre-clinical animal testing on any new treatments (Mosekilde 1995; Ominsky et al. 2011). In assessing bone quality, various mechanical properties can be measured (Hernandez and Keaveny 2006; Turner and Burr 1993; Fyhrie and Christiansen 2015), typically stiffness, strength, toughness, and ductility. All these properties are obtained from monotonic loading. In addition, fatigue strength and fatigue life can be measured, both of which require cyclic (repetitive) loading. Fatigue properties are potentially unique as an assay for bone quality because fatigue-related failure mechanisms such as slow crack growth and microdamage accumulation are not always manifested in monotonic loading (Kruzic and Ritchie 2008; Nalla, Kinney, and Ritchie 2003). Cyclic loading is particularly challenging to perform in a precise manner in small animals, such as in rats and mice, due to the small size of the vertebrae and the inevitable machine-compliance effects that are difficult to eliminate. Resulting problems, such as loss of test specimens during the experiment and the confounding levels of inter-specimen variations in fatigue response, both serve to reduce statistical power (Brouwers et al. 2009), which in turn can lead to inconclusive findings regarding the role of bone quality.

As a result of these challenges, and because of the continuing interest in bone quality (Bouxsein 2003a; Seeman and Delmas 2006), there remains a need to refine the experimental protocols for cyclic loading of small-animal vertebrae. We report here on a method for cyclic mechanical testing of the mouse lumbar vertebra *ex vivo* that has improved precision. The resulting low degree of inter-specimen variation in fatigue life should help optimize statistical power in animal experiments, thus improving the ability of researchers to detect mechanically relevant changes in bone quality due to aging, disease, or treatment.

2.2 Materials and Methods

We first present our new method as applied to mouse vertebrae. Then, to demonstrate utility, we describe results from cyclic testing experiments for three groups (n=5–6 per group) of L5 mouse vertebrae, comparing results for our new method (referred to as "K_{FEA} method") against two existing methods from the literature (referred to as "K_{EXP} method" and "F_{MAX} method") (Caler and Carter 1989; Bowman et al. 1998; Haddock et al. 2004; Lambers et al. 2013; McCubbrey et al. 1995; Brouwers et al. 2009).

[1] Manuscript of Chapter 2 submitted to the peer-reviewed journal Bone in June 2018.

Animals

Our experiments used L5 vertebrae obtained post-mortem from male C57BL/6J mice (Jackson Labs, Sacramento, CA) that were in the control groups of various previous studies (unpublished). All original studies, and this study, were approved by NASA Ames Research Center (ARC) Animal Care & Use Committee, and all experimental testing was conducted at NASA ARC. Ages of the mice ranged from 15-18 weeks. After sacrifice, the L1-S1 spinal segment was excised from the mouse with a scalpel via an anterior approach. The L5 vertebra was then separated by slicing through the adjacent intervertebral discs, gently cleaned of soft tissue, wrapped in saline-soaked gauze (Gibco PBS 1X, pH 7.4), and stored at -20°C until specimen preparation.

Specimen preparation

Obtaining true plano-parallel surfaces, which is difficult for such small specimens (Brouwers et al. 2009), is important to ensure full contact — and thus uniform compression — between the specimen surface and loading platens. If plano-parallel surfaces are not achieved, or if the loading platens are not perfectly parallel, local contact can occur over just part of the specimen surface. This introduces unwanted scatter in the mechanical response and perhaps also premature failure. Thus, we developed a detailed method for this aspect of the specimen preparation (**Figure 2.1**). Each vertebra was aligned inside a 3D-printed (Stratasys Dimension SST 1200es, Eden Prairie, MN), disposable jig with a metal pin (diameter range 0.91 to 0.99 mm; length of 38 mm) (**Figure 2.1 A**) and secured with polymethyl methacrylate (PMMA). The combined jig-bone construct was then positioned in a diamond-saw microtome (Leica SP1600 Saw Microtome, Wetzlar, Germany). Two parallel cuts were made on the cranial and caudal surfaces under constant irrigation to remove the endplates (**Figure 2.1 B**). A final cut through the posterior pedicles released the vertebral body from the jig (**Figure 2.1 C**).

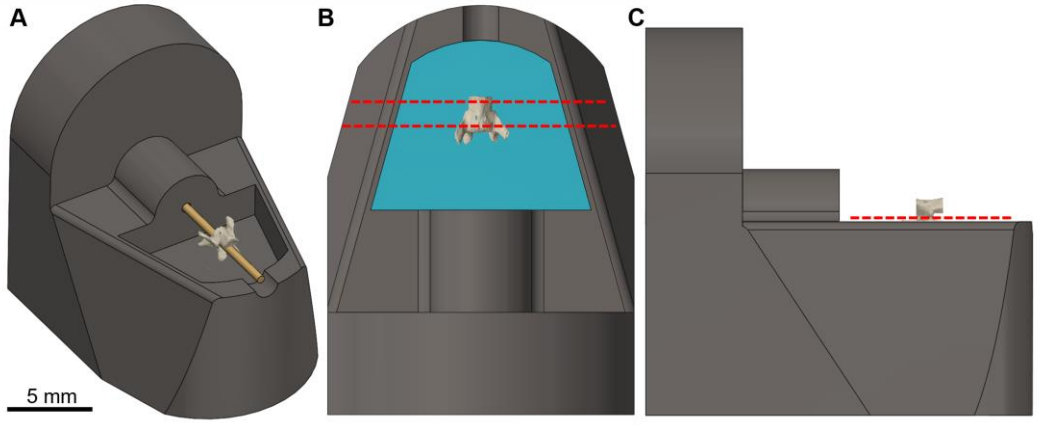

Figure 2.1 – Machining of a parallel-planed vertebral body. (A) A 3D-printed, disposable, plastic jig was designed to securely grip the specimen during machining (the stl file is available for download at http://oconnell.berkeley.edu/resources/). A vertebra is placed into the jig using a snugly fit, metal alignment pin (gold) through the vertebral foramen (pin diameter 0.9 – 1 mm) and sits in a diameter-matched channel. The spinous process is oriented into the jig's shallow well, which is then filled with PMMA (blue) to secure the vertebra. (B) Once the PMMA is set, the pin is removed and two plano-parallel cuts (red) through the endplates are made using a diamond-saw microtome (not shown). (C) A scalpel cut (red) through the pedicles releases the planed vertebral body.

Quantitative micro-CT imaging

After machining, specimens were imaged using quantitative micro-CT (µCT 50, Scanco Medical AG, Bruttisellen, Switzerland) at a 10-µm voxel size (55 kV, 109 µA, 1000 projections per 180°, 500 ms integration time) (**Figure 2.2**). Micro-CT images of the whole specimen (cortical and trabecular compartments) were analyzed for height, minimum tissue cross-sectional area (minimum value of tissue area at any cross-section, over all cross-sections), and total bone volume fraction (BV/TV) (ImageJ 1.51h, Java 1.6.0) by manually contouring around the cortical bone and interpolating contours every ten image slices. Additionally, the trabecular compartment was manually segmented, separate from the cortex. Each specimen was evaluated for trabecular micro-architecture (Scanco Evaluation Software v6.0): trabecular bone volume fraction (Tb.BV/TV), number (Tb.N), thickness (Tb.Th), and separation (Tb.Sp). Specimens were returned to the freezer after imaging.

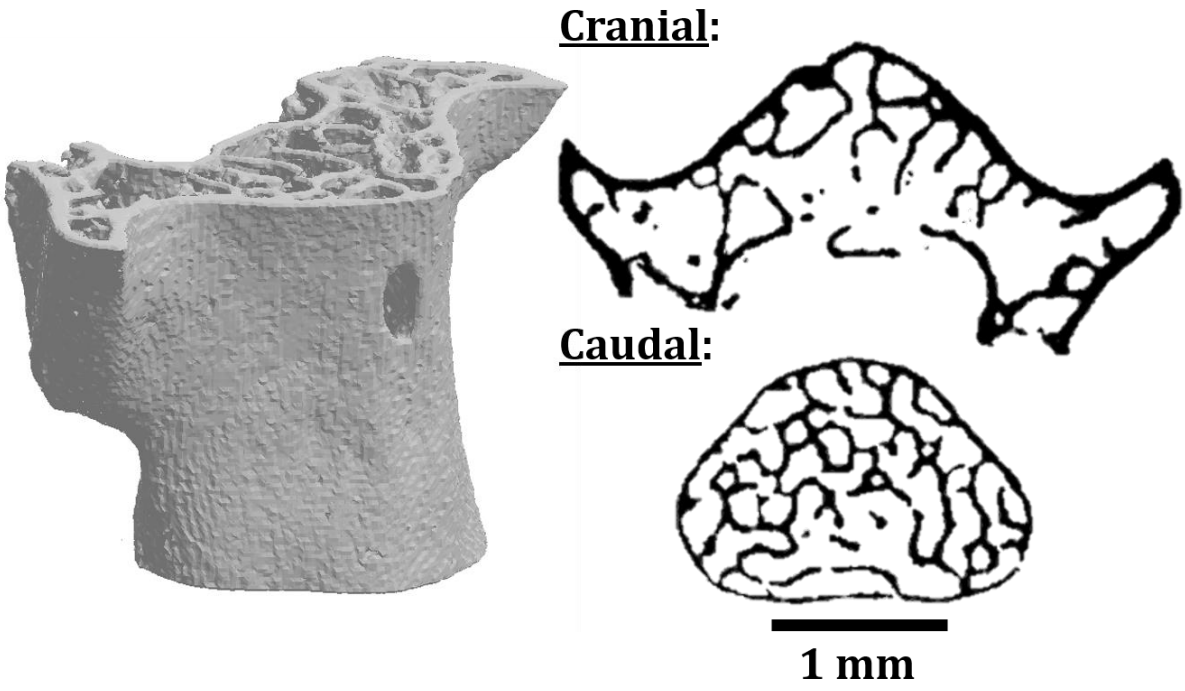

Figure 2.2 – Representative sample of a mouse vertebral body after all specimen preparation. Cranial and caudal cross-sections shown at 10-µm voxel resolution.

Calculating specimen-specific cyclic forces

We used a force-control loading protocol, which allows both creep and damage to occur during cyclic loading. Since the cyclic loading response of bone appears to be determined by the magnitude of the applied *strain* (as opposed to the magnitude of stress) (Nalla, Kinney, and Ritchie 2003; Keaveny, Wachtel, Ford, et al. 1994; Keaveny, Guo, et al. 1994), our protocol required us to calculate a specimen-specific level of applied force that resulted in a specified level of initial elastic strain. Cyclic loading in force control in this way should minimize scatter in the resulting fatigue life despite the heterogeneity in size, shape, and microarchitecture of the mouse vertebrae.

This protocol required measuring the overall vertebral stiffness before starting the cyclic loading so that the prescribed strains (ε_{min} and ε_{max}) could be converted into specimen-specific levels of applied force (F_{min} and F_{max}). However, experimentally measuring stiffness for any bone is challenging due to different types of machine compliance errors, which can introduce both fixed and random errors (Odgaard, Hvid, and Linde 1989; Odgaard and Linde 1991; Keaveny et al. 1993; Keaveny et al. 1997). The fixed errors have implications for external validity, but otherwise do not compromise comparisons within any given experiment and are therefore oftentimes acceptable. However, large random errors compromise statistical power, particularly when sample sizes are low (n<10 per specified strain level). Thus, to circumvent any errors associated with machine compliance, we used a computationally derived stiffness (K_{FEA}) found from specimen-specific, micro-CT-based, linearly elastic, voxel-based finite element analysis. The models used 10-μm sized cube voxels and assumed a tissue-level (voxel) elastic modulus of 10 GPa for all specimens (see section 2.5 Supplemental Material for details). The specimen-specific cyclic forces (F_{min} and F_{max}) were then calculated for each specimen using K_{FEA}, the specimen height (H) as measured from micro-CT, and two assumed nominal values of initial elastic strain (ε_{min} = 0.05% and ε_{max} = 0.5%) (**Equations 1 and 2**).

$$F_{min} = K_{FEA} H \varepsilon_{min} \quad (1)$$

$$F_{max} = K_{FEA} H \varepsilon_{max} \quad (2)$$

The assumed value of ε_{max} = 0.5% was chosen empirically by trial and error on some prior specimens, such that the resulting F_{max} values were approximately half of the directly measured ultimate force, which generally places a bone specimen in the middle region of its fatigue life. The minimum initial elastic strain value was chosen such that the resulting F_{min} values were near 1 N.

Mechanical testing

Within one week after imaging, specimens were thawed again to room temperature and prepared for cyclic loading in uniaxial compression to failure. The vertebral body was positioned onto the center of the lower platen of the material testing device (TA ElectroForce 3200, Eden Prairie, MN). Because obtaining perfectly parallel loading platens can be challenging, the upper platen comprised a spherically-seated platen on a lubricated ball-bearing which allows the platen surface to rotate and mate flush with the sample surface to achieve uniform contact (**Figure 2.3**); with the pre-load in place, the set screws on the upper platen are locked. We used a compressive pre-load of 1 N, and after the platen was locked room-temperature saline-solution (Gibco PBS 1X, pH 7.4) was added to the bath until the specimen was fully submerged. The pre-load was then adjusted to the predetermined F_{min}, and then sinusoidal cycles of compression between F_{min} and F_{max} were applied at a frequency of 8 Hz until the specimen reached 10% strain.

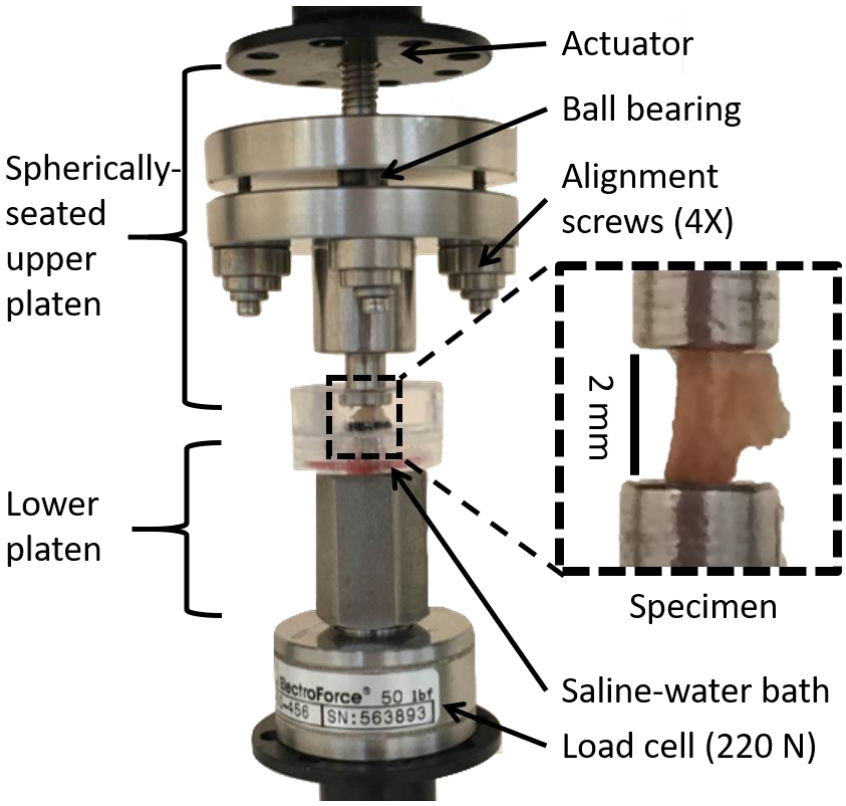

Figure 2.3 – Experimental test set-up for fatigue test shown with spherically-seated upper platen and specimen after preparation.

Outcome Measurements

Three plots were produced from each specimen fatigue test. First, the force-displacement data were plotted for each loading-unloading cycle, from which stiffness was defined as the secant stiffness, or range of force divided by range of displacement per cycle (**Figure 2.4 A**). Second, the apparent strain per cycle was plotted, and was separated into three curves representing total strain, creep strain, and damage strain (**Figure 2.4 B**). The total-strain curve was used to find the number of cycles to failure, or fatigue life (N_f) and strain to failure (ε_f) using the point of intersection between the curve and a 0.5% line offset parallel to a line of best fit for the secondary region (Bowman et al. 1998; Brouwers et al. 2009). Third, we plotted stiffness per cycle (**Figure 2.4 C**) to identify three variables: elastic stiffness of the specimen ($K_{elastic}$), stiffness at failure (K_f), and rate of stiffness degradation. Elastic stiffness was calculated as the average stiffness over ± 500 cycles centered about the maximum value of stiffness (K_{max}), which typically occurred after a few thousand cycles of loading; the stiffness at failure was defined as the stiffness measured at cycle N_f; and the rate of stiffness degradation ($\Delta K/\Delta N$) was calculated as the slope of a line that best fit the middle 50% of points in the range between K_{max} and K_f. The $\Delta K/\Delta N$ parameter reflected accumulation of fatigue damage, larger values indicating a more rapid accumulation of fatigue damage per loading cycle.

In addition to these fatigue parameters, we also calculated an effective elastic tissue modulus (E_{tissue}). This was calculated using both the experimental ($K_{elastic}$) and computational (K_{FEA}) assessments of stiffness, scaling with respect to the assumed FEA tissue-level (voxel) modulus of 10GPa (**Equation 3**).

$$E_{tissue} = 10\left(\frac{K_{elastic}}{K_{FEA}}\right) \quad (3)$$

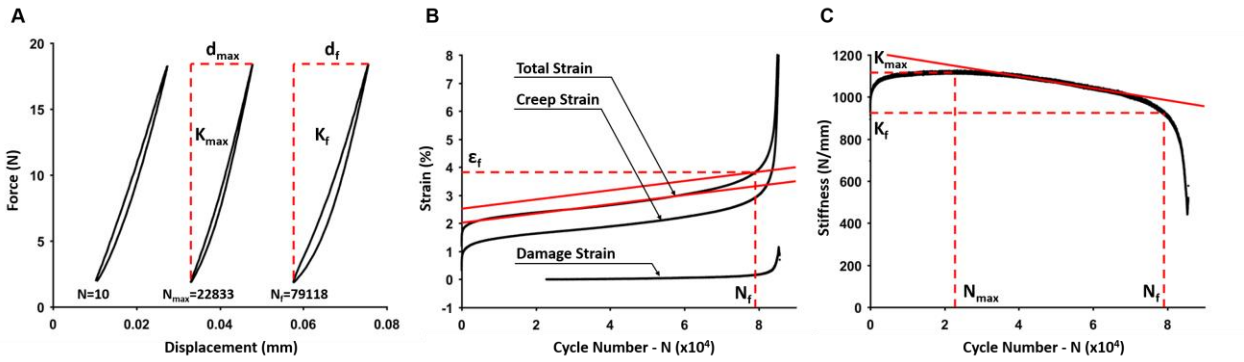

Figure 2.4 – Three plots generated from fatigue testing of a specimen. (A) Force-displacement shown for three cycles as the test progresses; an early cycle, the cycle of maximum stiffness, and the cycle defined as failure. (B) Strain per cycle was plotted for total strain, creep strain, and damage strain (Haddock et al. 2004). Damage strain was only plotted from the cycle at which stiffness was the greatest (N_{max}) and began to decline. Fatigue life, N_f, and strain to failure, ε_f, are found from the total strain curve (Bowman et al. 1998). (C) Stiffness per cycle displaying the maximum stiffness, K_{max}, from which $K_{elastic}$ was calculated, and stiffness at failure, K_f. Rate of stiffness degradation is the slope of the solid red line.

Alternative methods for calculating specimen-specific cyclic forces

Two other methods known from previous literature were also implemented to assess performance of the new method. For the first "K_{EXP} method" (Caler and Carter 1989; Bowman et al. 1998; Haddock et al. 2004; Lambers et al. 2013; Brouwers et al. 2009), instead of using the finite element-derived value of stiffness (K_{FEA}) in Equation 1, the experimental measurement K_{EXP} was used. Following literature protocol, K_{EXP} was found by pre-loading the specimen in compression to 1 N, cycling between 1–10 N 20 times, and using the slope from the force-displacement curve of the 20th cycle. All other mechanical testing details were the same as for our new method except for two differences in the K_{EXP} method: 1) the upper platen used was a rigid design (not adjustable); and 2) the cyclic frequency was 2 Hz. Fatigue behavior of bone has been shown to be unaltered for any loading frequency below 15 Hz (Lafferty 1978; Yamamoto et al. 2006).

For the second "F_{MAX} method" (McCubbrey et al. 1995), F_{max} was calculated using the measured strength of the adjacent L4 vertebra, obtained by monotonic compression to failure. The L5 strength was estimated as the product of the L4 strength and the ratio of minimum tissue cross-sectional areas (micro-CT) for the L4 and L5 vertebrae, and F_{max} was then calculated as 50% of the L5 force. All other mechanical testing details were the same as our new method.

Statistical Analysis

The means and standard deviations of cyclic loading force, fatigue life, and $K_{elastic}$ were statistically analyzed to compare the new method against the other two methods. To compare means, a one-way ANOVA was conducted, with a Tukey-Kramer *post-hoc* test applied to evaluate significant differences. A p value of less than 0.05 was considered statistically significant. To compare standard deviations, a Bartlett test was conducted. Standard deviations

were considered significantly different with a F-ratio greater than 1, and *p* value less than 0.05. Also, linear regression was used to model the relationship between maximum cyclic loading force and log of fatigue life (equivalent to a traditional S-N fatigue curve). All statistics were performed using JMP (v13.0, SAS Institute).

2.3 Results

Of all three methods tested, the K_{FEA} method produced the lowest variation in fatigue life. The mean value of the applied force was the same for all groups (22 N), but the standard deviation was lowest for the new (K_{FEA}) method (±0.77 N), 8-fold and 7-fold lower than the K_{EXP} and F_{MAX} methods (F-ratio = 5.5; $p < 0.01$; **Figure 2.5**), respectively. Because of these larger variations in applied force for the literature methods, the fatigue life displayed a negative S-N type relation with the loading force ($R^2 = 0.73$ both literature methods) but there was no such correlation for the new method ($R^2 = 0.07$; **Figure 2.6 B**). Instead, for the new method the fatigue life was approximately uniform across all specimens (5.0 ± 0.2), and its standard deviation was 5-fold and 2-fold lower than for the K_{EXP} or F_{MAX} methods, respectively (F-ratio = 4.9; $p = 0.008$; **Figure 2.5**).

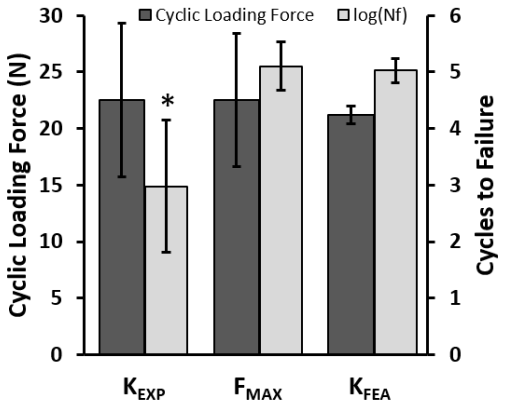

Figure 2.5 – Specimen-specific cyclic loading force and number of cycles to failure, or fatigue life for each method. Error bars represent standard deviations. There was no difference in the cyclic loading force across groups, but standard deviation was lowest for the K_{FEA} method. The K_{EXP} method fatigue life was significantly lower compared to the F_{MAX} and K_{FEA} methods. There was no change in fatigue life between the F_{MAX} and K_{FEA} methods. Standard deviation was significantly lowest for the K_{FEA} method. Significance indicated is $p < 0.01$.

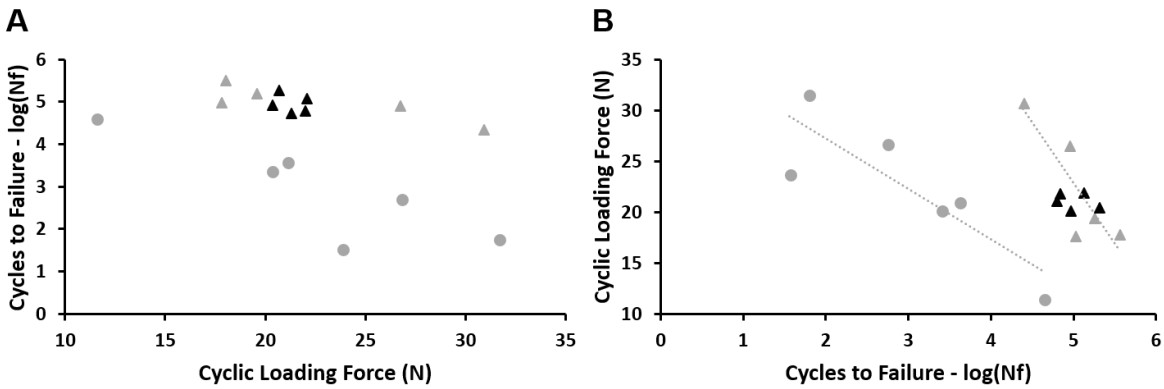

Figure 2.6 – (A) Fatigue life (N_f) verses maximum cyclic loading force plotted for each specimen tested. Gray circles indicate the K_{EXP} method, gray triangles indicate the F_{MAX} method, and black triangles indicate the K_{FEA} method. (B) The transpose of the same data, is plotted to match the format of a S-N curve. Two different F-N curves are found, one for the K_{EXP} method and another for the F_{MAX} and K_{FEA} methods. The K_{EXP} and F_{MAX} methods have a large range of forces applied across specimens and thus unintentionally define a F-N curve. (R^2 = 0.73 for both literature methods). In contrast, the K_{FEA} method has a small range of forces applied across specimen in that group and thus tests only a small region of the F-N curve as intended (K_{FEA} R^2 = 0.073).

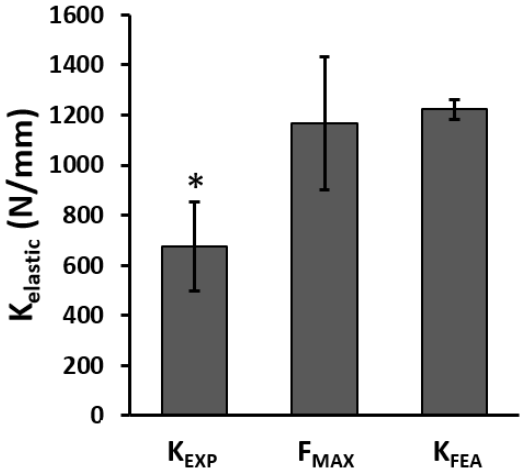

Figure 2.7 – Average elastic stiffness of the vertebra for each method. Error bars represent ± 1 standard deviation. The K_{EXP} method stiffness was significantly lower ($p < 0.01$) compared to the F_{MAX} and K_{FEA} methods.

The new method also provided other measurements related to bone quality, both of which displayed high uniformity across the specimens: the effective tissue elastic modulus, E_{tissue}, was 5.8 ± 0.2 GPa and the strain to (cyclic) failure, ε_f, was 3.2 ± 0.8%.

Three additional aspects of the behavior for the two literature-based methods were noteworthy. First, compared to the new method, the fatigue life was lower for the K_{EXP} method by 40.9% (p = 0.002) whereas fatigue life for the F_{MAX} method was not different ($p > 0.90$; **Figure 2.5**). Second, the elastic stiffness measured from fatigue testing ($K_{elastic}$) was also lower for the K_{EXP} method than the F_{MAX} method by 42.1% (p = 0.002), and than the new method by 44.8% ($p < 0.001$); stiffnesses for the F_{MAX} and new methods were not different ($p > 0.80$; **Figure 2.7**). And third, the standard deviation for stiffness was lowest for the new method (F-ratio = 4.53; p = 0.011; **Figure 2.7**) compared to the K_{EXP} and F_{MAX} method. The difference in

stiffness variation between F_{MAX} and the new method, which both used the spherically-seated platen, shows that large variations in stiffness can still exist even with the use of a pivotable fixture, presumably due to variable degrees of machine compliance.

2.4 Discussion

Our new method for cyclic loading of small-animal vertebrae yielded highly reproducible measurements of fatigue life and was successful, in part, by effectively controlling for the strain applied to these tiny bone specimens. Failure of bone in both static and fatigue loading is largely thought to be strain-controlled (Nalla, Kinney, and Ritchie 2003; Bowman et al. 1998; Keaveny et al. 2001; Keaveny, Wachtel, Guo, et al. 1994; Schileo et al. 2008). To apply a repeatable initial strain to each specimen, a consistent measurement of stiffness must first be obtained. Our new method utilized specimen-specific micro-CT-based finite element analyses to measure specimen stiffness and prescribe an individualized cyclic force for each specimen. In turn, these individualized forces resulted in a consistent starting level of strain applied to all test specimens, and resulted in similar values of fatigue life. By contrast, our implementations of the two literature methods were unable to consistently apply the specified starting strain value, which produced more scatter in the magnitude of the applied forces and an unintended S-N-like relationship.

The consistency of our strain-to-failure results with those from other studies provides additional support for the accuracy and validation of our method. We observed a relatively uniform value for strain-to-failure from fatigue compression testing of the mouse vertebrae (3.20 ± 0.80%). Our value is consistent with additional fatigue compression testing conducted in other species: 3.36 ± 2.13% for human trabecular bone (Haddock et al. 2004), 2.85% ± 0.66% for bovine trabecular bone (Bowman et al. 1998), and 4.19 ±1.52% for rat whole-bone vertebra (Brouwers et al. 2009). A similar value in strain-to-failure between these studies and ours is expected for three reasons. First, the loading conditions (compressive fatigue) were the same for all tests listed. Second, the bone material, primarily the collagen component which dominates the plasticity and therefore strain-to-failure of the bone (Burstein et al. 1975), is similar amongst the species listed. And third, others have reported on a relatively uniform values for the strain-to-failure independent of apparent density, applied loads, or temperature (Bowman et al. 1998; Keaveny et al. 2001; Keaveny, Wachtel, Guo, et al. 1994). Therefore, the consistency and repeatable value of strain-to-failure supports the validation of our method in achieving fatigue-like failure.

In addition to a repeatable measure of fatigue life, an effective tissue elastic modulus, another important measure of bone quality, can be obtained from specimens by implementing our new K_{FEA} method. A tissue-level modulus cannot be measured easily from mechanical testing alone because of the complex structure of the bone (Brouwers et al. 2009). For example, the tissue cross-sectional area of the mouse vertebrae varies greatly from cranial to caudal surfaces. However, when the finite element model is built, each voxel is assigned a modulus of 10 GPa. This modulus can be scaled by the ratio of experimental stiffness ($K_{elastic}$) to computational stiffness (K_{FEA}) to obtain the effective tissue modulus of the specimen.

Our findings also indicate that implementing a pivotable loading platen to ensure uniform contact is important for accuracy of results, at least for these small-animal bones. We observed a reduced $K_{elastic}$ and fatigue life for the K_{EXP} method compared to the F_{MAX} and new methods, even though the specimens used in the K_{EXP} and new methods were uniform in size and microarchitecture (section 2.5 Supplemental Material; **Table 2.1**). We attribute these inconsistent results to the rigid platen design used in the K_{EXP} method testing. Even with rigorous specimen preparation in place, we found that perfectly plano-parallel loading surfaces on small bones cannot always be achieved. And without an adjustable platen, the load can be localized to an area that comes into contact with the platen first, producing an effective stress concentration. This localized load can result in reduced stiffness and the stress concentration in reduced fatigue life.

There are some limitations to this study. First, the bone tissue acquired for this study was shared tissue, which did not allow for random assignment of animals to each group from the same sample set, and therefore a possibility of heterogeneity between groups exists. This heterogeneity could account for some of the larger standard deviations observed in the K_{EXP} and F_{MAX} methods. Therefore, it is possible that some of the observed improvement (reduction) in fatigue life scatter for the new method was simply due to a lower heterogeneity in those specimens tested. However, the similarity in size and structure of specimen across all groups as per micro-CT analysis (section 2.5 Supplemental Material; **Table 2.1**) suggests this is unlikely. Second, for fatigue testing, the initial strain values of ($\varepsilon_{max} = 0.5\%$) used for our new method may be specific to this particular protocol. The assumed value was chosen empirically by trial and error on some preliminary test specimens, such that the resulting F_{max} values were approximately half of the directly measured ultimate force. To use this method in other animal models, large or small (e.g. rat, monkey, human), similar preliminary testing to determine the value of ε_{max} is suggested. We recommend using an elastic strain level that is associated with about half of the ultimate strength. Third, the values of the effective tissue elastic modulus found may vary depending on the testing conditions. Parameters such as temperature, loading frequency, and use of different fixture designs can all contribute to varied machine compliance between tests and in turn impact the effective tissue modulus. Therefore, it is best to use the effective tissue modulus as a relative measurement to compare between untreated and treated specimens within an experiment, but not across studies (e.g. between mouse and rat bones).

In terms of applications, the main application of our new method is to provide greater statistical power in using small-animal experiments to mechanically assess relevant aspects of bone quality associated with aging, disease, or treatment. A small sample size and scatter associated with the fatigue testing present challenges for detecting statistically significant effects unless those effects are large. For example, Brouwers et al. (Brouwers et al. 2009) found a 37.5% difference in steady-state creep rate and 15.7% difference in loss of stiffness with zoledronate treatment in an osteoporotic rat model, but could not report a detectable significance due to high variation in the data and loss of some samples. They used a method similar to the K_{EXP} method, which produced standard deviations in fatigue life (reported as “time-to-failure”) up to the same magnitude as the mean value. By contrast, with our new method those standard deviations can be reduced up to 8-fold, as shown by our study comparisons. Furthermore, we had no loss of specimens, enabled by repeatable specimen preparation (e.g. 3D-printed support jigs for machining plano-parallel surfaces) and uniform loading of specimen surfaces (e.g. spherically-seated platen), which further improves statistical power. Implementing our new method is a time

intensive process for specimen preparation, micro-CT, image processing, and finite element analysis. However, the extra effort improves the ability to detect small differences across treatment groups without using a large number of animals. Thus, use of our new method should improve the ability of future studies to assess mechanically relevant aspects of bone quality associated with aging, disease, or treatment.

2.5 Supplemental Material

Image Processing

Image processing of the original micro-CT images was conducted prior to finite element analysis for each specimen. First, the image stack was reoriented to align the specimen with the z-axis (DataViewer v1.5.2.4, Bruker). Second, the reoriented images were thresholded using the 'Default' Autothreshold algorithm in ImageJ (ImageJ 1.51h, Java 1.6.0_24). The final stack was used to build the finite element model.

Finite element analysis

To determine the computational stiffness, high-resolution linear finite element analysis was performed. Each 10-μm cubic voxel in the images was converted into an eight-noded brick element to create a finite element model of the entire vertebral body. All bone elements were assigned the same elastic, homogeneous and isotropic material properties: elastic modulus 10 GPa and Poisson's ratio of 0.3 (Bevill and Keaveny 2009). Each model was uniaxially compressed to 2% apparent strain, the input was displacement which varied depending on specimen height. Typical models contained approximately 1.5 million elements and were solved using a highly scalable, implicit parallel finite-element framework Olympus (Adams et al. 2004) running on a Dell Linux Cluster supercomputer (Stampede, Texas Advanced Computing Center). The outcome was the whole-bone reaction force, which was then used to calculate computational stiffness, K_{FEA}, by dividing by the input displacement (**Equation 4**).

$$K_{FEA} = \frac{Reaction\ force}{Input\ displacement} \qquad (4)$$

Table 2.1 – The K_{EXP} and K_{FEA} method specimen structural parameters indicate there were no significant differences in specimen size and shape. F_{MAX} method specimen parameters were not comparable because of a difference in resolution of these micro-CT scans (20.7 μm). The stiffness and fatigue life measurements are the same for the F_{MAX} and K_{FEA} methods, which suggest the structural parameters for the F_{MAX} method specimens were similar to those used in the K_{EXP} and K_{FEA} methods.

Measure	K_{EXP} (n=6)	K_{FEA} (n=5)	*p*
Min Tissue Area (mm^2)	0.97 ± 0.19	0.96 ± 0.09	0.92
Avg Tissue Area (mm^2)	1.71 ± 0.33	1.59 ± 0.11	0.47
BV/TV (%)	34.0 ± 1.00	33.0 ± 1.00	0.08
Tb.BV/TV (%)	22.0 ± 3.00	23.0 ± 1.00	0.83
Tb.N (1/mm)	4.94 ± 0.42	5.30 ± 0.32	0.15
Tb.Th (μm)	47.1 ± 3.26	44.5 ± 2.58	0.19
Tb.Sp (μm)	198 ± 17.8	185 ± 14.1	0.24

Mean ± SD

Chapter 3 – Short and Long-term Effects of *in vivo* Ionizing Radiation Exposure on Monotonic and Cyclic Loading Strength of Mouse Vertebrae

3.1 Introduction

The effects of exposure to ionizing radiation on bone strength is of interest for numerous reasons, including spaceflight and radiotherapy. Human-occupied missions to Mars may only be undertaken if any bone weakening from exposure to deep-space ionizing radiation (National Council on Radiation Protection and Measurements. 2000; Chancellor et al. 2018; Cucinotta and Durante 2006; Wilson et al. 1995) can be properly managed to mitigate any increased risk of bone fracture for astronauts both in space and upon return to earth. In clinical therapy, women with anal, cervical, or rectal cancer (Baxter et al. 2005; Okoukoni et al. 2017) and with breast cancer (Overgaard 1988) have been shown to be at higher risk of bone fracture at sites directly exposed to radiation. From a basic science perspective, understanding the mechanisms by which irradiation can alter bone strength might also provide insight into general bone quality-related mechanisms that could be associated with aging, disease, or drug treatment.

While the effects of space and clinically-related levels of irradiation on bone strength have been studied for monotonic (one-time) loading (Bandstra et al. 2008; Kondo et al. 2009; Alwood et al. 2010; Wernle et al. 2010), much less is known about the effects for cyclic (repeated) loading. There is evidence of increased collagen crosslinks at the molecular level after radiation exposure (Akkus and Belaney 2005; Gong et al. 2013; Oest and Damron 2014). While such changes appear to only have a small effect on monotonic properties such as elastic modulus and yield stress (Currey et al. 1997; Zioupos, Currey, and Hamer 1999) these changes may have a larger effect on fatigue life by possibly impeding fibrillar sliding, reducing plasticity, and increasing the rate of microcrack growth during cyclic loading (Acevedo et al. 2015). Cyclic mechanics may also be affected by reductions in trabecular bone mass and microarchitecture, which can occur from radiation exposure (Hamilton et al. 2006; Kondo et al. 2009; Alwood et al. 2010; Green et al. 2012; Oest et al. 2015). Furthermore, there may be differences the short- and long-term effects on mechanics (Wernle et al. 2010) because the cell-mediated response to irradiation is different overtime (Oest et al. 2015).

Using an *in vivo* murine model, the goal of this study was to determine the effects of space (1 Gy) and clinical (5 Gy) levels of radiation on the cyclic and monotonic mechanical properties of mouse vertebrae, as well as on the underlying bone mass, microarchitecture, and collagen structure. Further, to gain insight into cell-mediated effects, we investigated both short-term and long-term responses for each radiation dose.

3.2 Materials and methods

Animals and Experiment Design

We conducted gamma-radiation exposure experiments on mice at space- and clinically-relevant doses, and collected bone tissue at both an early and late time points. Assays included monotonic and cyclic mechanical loading, biochemical assessments of the organic matrix, quantitative characterization of the trabecular and cortical mass and micro-architecture, and

micro-CT-based finite element analysis. Eighty-four male, 17-week old (skeletally-mature) C57BL/6J mice (Jackson Labs West, Sacramento, CA) were individually housed and randomly assigned to six groups (N = 14). Mice were exposed to either 0 Gy (sham-irradiated), 1 Gy, or 5 Gy and sacrificed at either 11-days or 12-weeks post-radiation. All experiment procedures were approved by NASA Ames Research Center (ARC) Animal Care & Use Committee and conducted at NASA ARC.

^{137}Cs Gamma Irradiation

Mice were exposed to whole-body, acute, γ-radiation from a ^{137}Cs source at 0.76 Gy/min (Mark-3 Irradiator, J.L. Shepherd, San Fernando, CA) for a total of 1.5, 1.32, and 6.58 minutes for the 0, 1 and 5 Gy groups respectively. Further details of irradiation procedures are reported elsewhere (Kondo et al. 2009).

Specimen preparation

After humane sacrifice, lumbar and sacral vertebrae, L3 to S1, were excised from the mouse, gently cleaned of soft tissue, wrapped in saline-soaked gauze (Gibco PBS 1X, pH 7.4), and stored at -20°C. The endplates of the L4 and L5 were removed to produce plano-parallel surfaces for uniaxial compression testing (Pendleton et al. 2018A, submitted for publication, Chapter 2). There were three freeze-thaw cycles in total for L4 and L5 vertebrae (-20°C to room temperature) between dissection, specimen preparation, imaging, and mechanical testing.

Quantitative micro-CT imaging

After machining, the L4 and L5 specimens were imaged with quantitative micro-CT (μCT 50, Scanco Medical AG, Bruttisellen, Switzerland) using a 10-μm voxel size (55 kV, 109 μA, 1000 projections per 180°, 500 ms integration time). Micro-CT images of the L4 and L5 specimens were analyzed for height (ImageJ 1.51h, Java 1.6.0). Additionally, the L5 specimen were evaluated for three-dimensional architecture of the trabecular and cortical compartments (Scanco Evaluation Software v6.0). After manually segmenting out the trabecular compartment — using a lower threshold of 300 grayscale units and a Gaussian filter with sigma of 0.5 and support of 2 — the following parameters were measured: trabecular bone volume fraction (BV/TV), number (Tb.N), thickness (Tb.Th), separation (Tb.Sp), connectivity density (Conn.D), and volumetric bone mineral density (Tb.vBMD). Additionally, after segmenting the cortex — from 0.5 mm above to 0.5 mm below the transverse processes and using a lower threshold of 380 grayscale units and a Gaussian filter with sigma of 0.8 and support of 1 — the following parameters were measured: cortical thickness (Ct.Th), cross-sectional area (CSA), and cortical bone mineral density (Ct.BMD).

Mechanical testing

After micro-CT imaging, uniaxial compressive monotonic and fatigue mechanical testing was performed. The monotonic testing was conducted on the L4 specimens, at a platen displacement rate of 0.01 mm/s. Force-displacement data were collected (1000 Hz) and custom code (MATLAB R2017a) was used to obtain whole-vertebral stiffness (K), ultimate force (strength; F_{ult}), and ultimate strain (ε_{ult}) (**Figure 3.1 A**). Elastic modulus and ultimate stress were not calculated because the cross-sectional area of the vertebral body varies substantially from cranial to caudal ends. The cyclic testing was conducted on the L5 specimens, using methods described in detail elsewhere (Pendleton et al. 2018A, submitted for publication, Chapter 2).

Briefly, before testing we calculated individualized minimum and maximum cyclic loading forces, F_{min} and F_{max}, for each specimen using micro-CT based finite element models (Pendleton et al. 2018A, submitted for publication, Chapter 2), such that all specimens were initially loaded to the same nominal value (0.5%) of initial elastic apparent strain (averaged over the entire specimen). After F_{min} and F_{max} values were calculated, specimens were cyclically loaded in force control between $-F_{min}$ and $-F_{max}$ in uniaxial compression until failure, using a sinusoidal waveform at 8 Hz (TA ElectroForce 3200, Eden Prairie, MN; 50 lb. load cell, resolution of ± 0.1N). Testing was conducted at room temperature (~24°C) in a saline-water bath to maintain hydration for the entire duration of test. Force-displacement data was collected (1000 Hz), and custom code was used to obtain fatigue properties including: fatigue life (N_f), strain to failure (ε_f), specimen elastic stiffness ($K_{elastic}$), and effective tissue elastic modulus (E_{tissue}) (**Figure 3.1 B**).

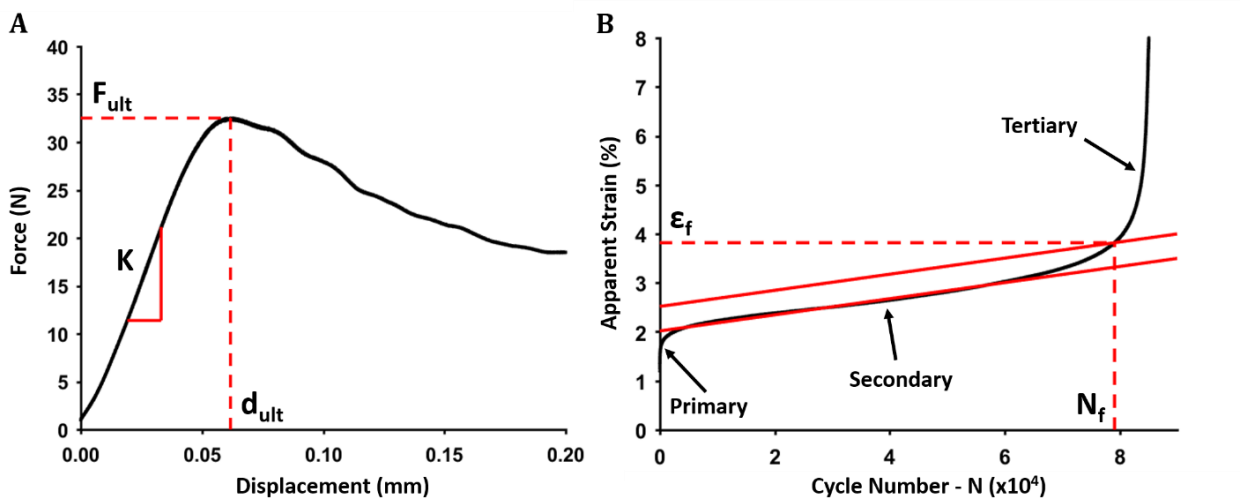

Figure 3.5 – Plots generated from mechanical testing of vertebral specimens. (A) For monotonic compression testing, a force-displacement curve was plotted to obtain: ultimate force (F_{ult}), stiffness (K) and ultimate strain (ε_{ult}). ε_{ult} was found by normalizing ultimate displacement (d_{ult}) by the specimen height. (B) For fatigue testing, maximum apparent strain per cycle was plotted to obtain: fatigue life (N_f) and strain to failure (ε_f). N_f and ε_f are found from the point of intersection between the apparent strain versus cycles curve, and a 0.5% line offset parallel to the line of best fit for the secondary region. Additionally, elastic stiffness ($K_{elastic}$) was found from fatigue testing. $K_{elastic}$ is an average stiffness over ± 500 cycles centered about the maximum value of stiffness which typically occurred after a few thousand cycles of loading. Lastly, with both experimental and computational assessments of stiffness of specimens tested in fatigue, we calculated an effective tissue modulus (E_{tissue}). E_{tissue} was calculated by scaling the FEA modulus of 10 GPa by the ratio of elastic stiffness to computed stiffness.

Biochemical assays

Assays were performed for advanced glycation end-products (AGEs) and collagen fragmentation to assess collagen modifications. To measure the AGEs, a fluorometric assay was applied to the S1 vertebrae, adapting protocols reported by Sell et al. (Sell and Monnier 1989). Each S1 specimen was demineralized in 0.5 M ethylenediaminetetraacetic acid (EDTA), and hydrolyzed in 12N HCl at 120°C for 3 hours to break down peptide bonds. The hydrolysate was then resuspended in PBS (0.1X) and pipetted in triplicate onto a black-walled 96 well plate. Quinine dissolved in H_2SO_4 was used as a standard. Fluorescence (370nm excitation, 440 nm emission) was measured and used to determine number of AGEs.

To measure collagen fragmentation, we used an automated electrophoresis assay (2100 Bioanalyzer, Agilent Technologies, Santa Clara, CA) applied to the L3 vertebrae. Our assay was based on the molecular weights of the alpha-1 (139 kDa) and alpha-2 (129 kDa) chains of Type-I collagen. To identify fragmentation, we looked for a wider distribution of molecular weights and a lower quantity of protein in the 130–140 kDa range. After isolating the collagen (section 3.5 Supplemental Material (Burton et al. 2014)), the collagen extract was dissolved in 1X PBS, prepared for electrophoresis (see Agilent Protein 230 Kit Guide), and evaluated using a software-generated "gel" and electropherogram (Agilent 2100 Expert software). Rat tail collagen (Sigma Aldrich) was run as a standard.

Statistics

We conducted a two-way Analysis of Variance (ANOVA) with terms for radiation, latency (time after irradiation until sacrifice), and the interaction of radiation by latency (JMP v13.0, SAS Institute). If any term was significant ($p < 0.05$), we conducted two *post-hoc* analyses: the Tukey-Kramer test to compare all groups against each other, and Dunnett's test to compare each group against the control (0 Gy, 11-day).

3.3 Results

Cyclic mechanical properties were lower in the long-term (i.e. at 12-weeks) with and without radiation exposure. For example, without radiation exposure, cycles to failure was 10% lower between 11-days and 12-weeks (**Table 3.1, Figure 3.2 A**). With irradiation at 1 Gy and 5 Gy, cycles to failure was 9.6% and 15.1% lower respectively compared to the control (0 Gy, 11-day). Short-term effects of radiation exposure on cycles to failure were not significant. Consistent with cycles to failure, elastic stiffness, measured during cyclic testing (Pendleton et al. 2018A, submitted for publication, Chapter 2), was also lower in the long-term with and without irradiation (**Table 3.1**). Strain-to-failure was the same for all groups. For measured monotonic properties, whole-bone strength was lower in the long-term with irradiation at 5 Gy. Strength, was 16.7% lower between 11-days and 12-weeks after 5 Gy exposure (**Table 3.1**). There were no differences in strength observed without irradiation, or with irradiation in the short-term. Stiffness and ultimate strain were the same for all groups.

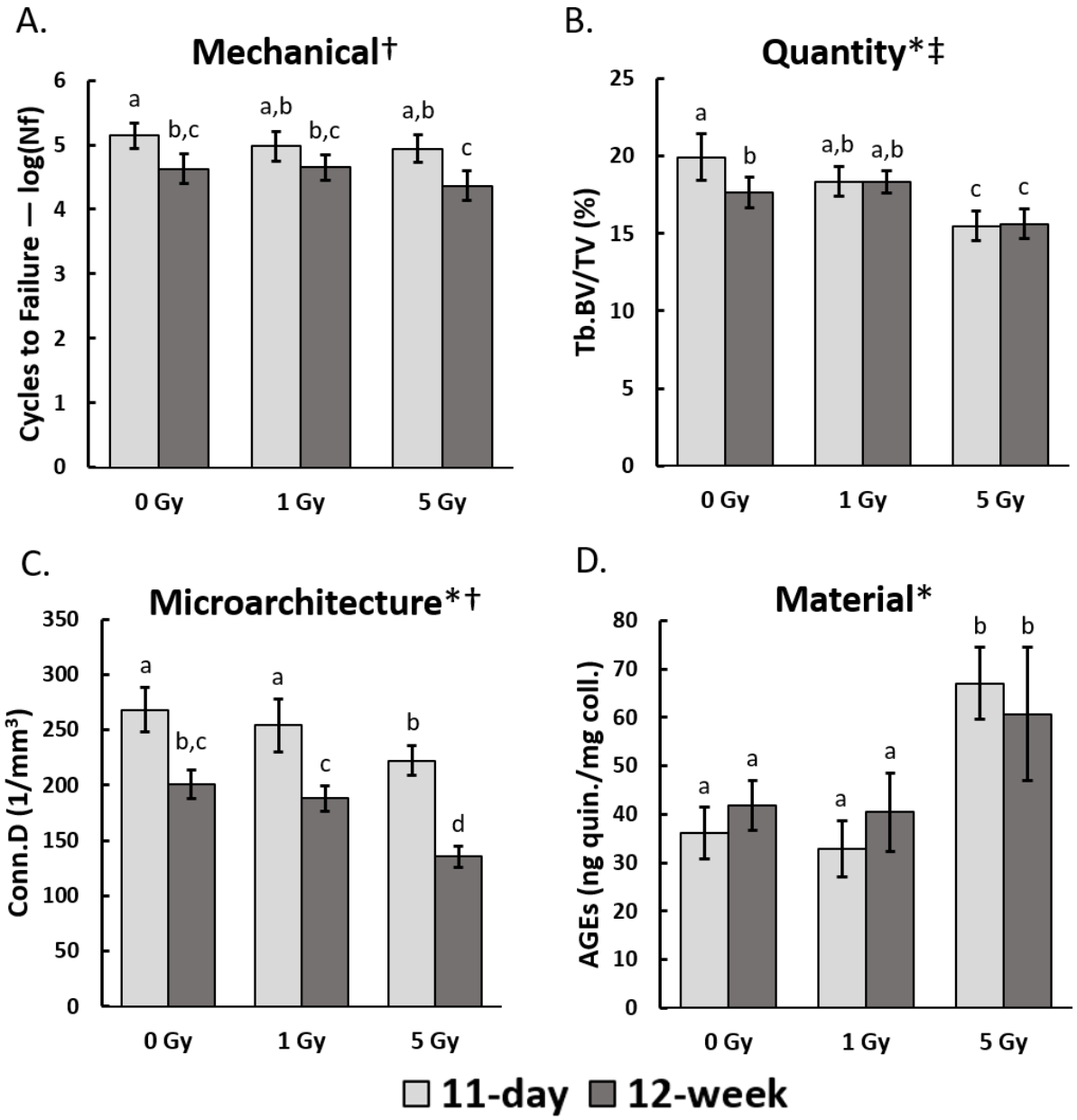

Figure 3.2 – Effects of 0, 1, & 5 Gy acute, whole-body, gamma-radiation exposure after an 11-day or 12-week latency period (time after irradiation until sacrifice) on parameters that are representative of the observed mechanical behavior, bone quantity, material, and microarchitecture. A: Number of cycles to failure. B: Bone volume fraction of the trabecular bone, BV/TV. C: Trabecular connectivity, Conn.D. D: Non-enzymatic collagen crosslinks, AGEs. Bars show the least-square means, error bars denote the 95% confidence intervals; bars with the same letter were not significantly different by the Tukey-Kramer post-hoc test. Significance by ANOVA is indicated with superscripts: *radiation $p < 0.05$ at least, †latency $p < 0.05$ at least; or ‡interaction (radiation x latency) $p < 0.05$ at least.

Table 3.1 – Results from a two-way ANOVA for terms of radiation, latency, and the interaction of radiation by latency for parameters of micro-CT, mechanical, and biochemical testing.

	No Radiation			Radiation Effects							
	Short-term	Long-term		Short-term				Long-term			
Parameters:	0 Gy, 11-day (Control)	0 Gy, 12-wk % diff.	*p***	1 Gy, 11-day % diff.	*p***	5 Gy, 11-day % diff.	*p***	1 Gy, 12-wk % diff.	*p***	5 Gy, 12-wk % diff.	*p***
BV/TV (%) *‡	19.9	**-11.5**	**0.005**	-7.9	0.086	**-22.3**	**0.000**	-8.1	0.079	**-21.6**	**0.000**
Tb.Th (mm) *	0.04	-3.2	0.095	-0.5	0.994	**5.4**	**0.001**	0.0	1.000	**4.8**	**0.004**
Tb.Sp (mm) *†	0.19	8.0	0.050	5.0	0.371	**16.1**	**0.000**	**9.2**	**0.020**	**27.6**	**0.000**
Tb.N (mm^{-1}) *†	5.05	**-8.5**	**0.002**	-4.0	0.285	**-11.8**	**0.000**	**-9.1**	**0.001**	**-21.5**	**0.000**
Conn.D ($1/mm^3$) *†	268	**-25.0**	**0.000**	-5.2	0.561	**-17.0**	**0.000**	**-29.7**	**0.000**	**-49.5**	**0.000**
SMI *†‡	0.75	15.8	0.183	20.1	0.057	**107.5**	**0.000**	5.5	0.934	**53.6**	**0.000**
CSA (mm^2)	0.64	-0.3	1.000	-1.4	0.933	1.5	0.926	-3.0	0.447	-0.1	1.000
Ct.Th (mm) †	0.05	**-11.1**	**0.035**	-4.0	0.790	0.5	1.000	**-13.0**	**0.009**	-10.5	0.055
Cycles to Failure — log(N_f) †	5.14	**-10.0**	**0.002**	-3.2	0.664	-3.9	0.500	**-9.6**	**0.004**	**-15.1**	**0.000**
Strain at Failure (%)	3.18	7.3	0.874	5.7	0.949	-1.0	1.000	-4.0	0.988	8.5	0.792
$K_{elastic}$ (N/mm) †	1216	**-11.2**	**0.014**	-4.6	0.594	-3.0	0.889	-6.7	0.239	**-16.5**	**0.000**
K_{FEA} (N/mm) *†	2180	**-13.1**	**0.000**	-2.6	0.874	-6.4	0.165	**-9.3**	**0.015**	**-15.6**	**0.000**
E_{tissue} (GPa)	5.61	1.9	0.982	-2.2	0.961	3.2	0.864	2.6	0.926	-1.6	0.989
Stiffness (N/mm) †	640	-7.9	0.818	-1.3	1.000	0.4	1.000	-11.6	0.522	-14.6	0.309
Ultimate Force (N) †	32.5	-7.8	0.537	-3.4	0.973	-4.7	0.908	-6.4	0.698	**-16.7**	**0.026**
Ultimate Strain (%)	3.63	-4.3	0.937	-5.4	0.886	-5.7	0.864	-3.6	0.968	-9.9	0.390
AGEs (ng quinine / mg collagen) *	36.2	15.6	0.785	-9.1	0.982	**85.5**	**0.001**	11.8	0.911	**67.9**	**0.002**
Tb.BMD (mg of HA / cm^3)	1070	-0.6	0.972	0.0	1.000	-0.7	0.951	0.3	0.998	-0.3	1.000
Ct.BMD (mg of HA / cm^3)	1206	-0.2	1.000	-0.1	1.000	0.2	1.000	0.0	1.000	-0.6	0.980

Least squares means (LSM) for the control group (0 Gy, 11-day) with the percent difference in LSM for all other groups compared to the control

** *P* values for Dunnett's test, comparing against the control group

* ANOVA showed significant effect ($p < 0.05$ at least) for radiation.

† ANOVA showed significant effect ($p < 0.05$ at least) for latency.

‡ ANOVA showed significant effect ($p < 0.05$ at least) for interaction.

With irradiation, trabecular bone mass was lower after 5 Gy in the short-term (i.e. after 11-days) and long-term (i.e. after 12-weeks), but no difference in mass was observed between the two time-points. With a dose of 5 Gy at 11-days, trabecular bone volume fraction was lower by 22.3% compared to the control and was the same after 12-weeks. A similar trend was seen with 1 Gy irradiation, but the difference in BV/TV was not significant. Also, without irradiation, only aging, trabecular bone mass was lower between 11-day and 12-week timepoints, with a BV/TV 11.5% lower (**Table 3.1; Figure 3.2 B**).

In contrast to bone mass, trabecular microarchitecture parameters were lower after 5 Gy radiation exposure in the short-term and long-term, however the deficits were largest in the long-term. For example, with a dose of 5 Gy, trabecular connectivity density was lower by 29.7% at 11-days and 49.5% after 12-weeks, compared to the control. Results for trabecular number and spacing were consistent with connectivity density (**Table 3.1**). Visual analysis (**Figure 3.3**) confirmed these results. Without irradiation, only aging, microarchitecture parameters were also lower. For example, connectivity density went down by 25.0% between 11-days and 12-weeks without irradiation (**Table 1, Figure 3.2 C**). Furthermore, trabecular thickness and structural model index were unaffected without irradiation between 11-days and 12-weeks, but were significantly different in the short-term and long-term after a dose of 5 Gy. In the short-term, trabeculae were thicker and more rod-like which persisted into the long-term (**Table 3.1**). Cortical thickness was lower with aging (-11.1%), and with irradiation in the long-term after a dose of 1 Gy (-13.0%).

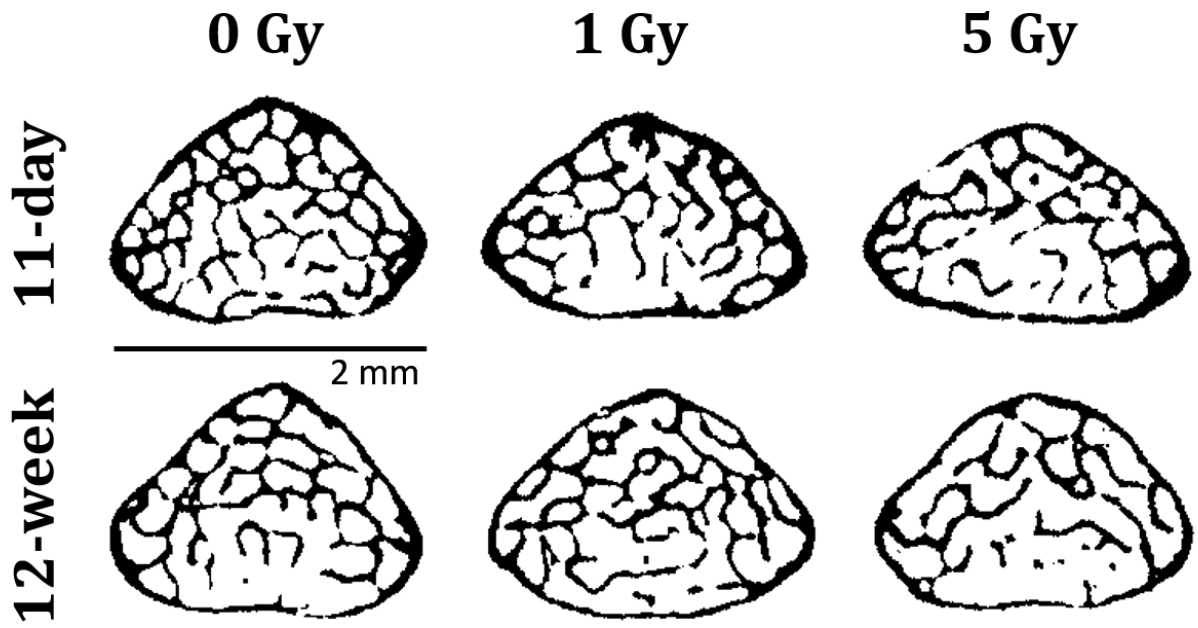

Figure 3.3 – Micro-CT images of transverse cross-sections from the caudal region of representative L5 vertebrae, showing the short-term and long-term effects of irradiation on the quantity and microarchitecture of trabecular and cortical bone.

Collagen crosslinking was elevated in the irradiated groups, but effective tissue modulus of the bone material was not. For example, with a dose of 5 Gy, the number of AGEs, representing non-enzymatic collagen crosslinks, was 85.5% greater than the control 11-days after

exposure, and 67.9% greater than the control 12-weeks after exposure (**Table 3.1; Figure 3.2 D**). Regardless of this difference in the collagen network, the effective tissue modulus remained the same across all groups (**Table 3.1**). No other differences were observed in the organic matrix or mineral content. For example, collagen molecular weight was the same for all groups, indicating no collagen fragmentation (**Figure 3.4**). Also, trabecular and cortical bone mineral density, measured via micro-CT, were the same across all groups (**Table 3.1**).

Overall, the trends observed for mechanical testing were most consistent with those identified for trabecular microarchitecture (**Figure 3.2**). The bone mass was lower and the material was different with greater amounts of collagen crosslinks after only 11-days with irradiation but was not different between 11-days and 12-weeks. These differences observed at 11-days did not coincide with a difference in mechanical properties at 11-days. In contrast, the deficits in trabecular connectivity density that are greater between 11-days and 12-weeks coincide with the lower number of cycles to failure also observed at 12-weeks, with and without irradiation.

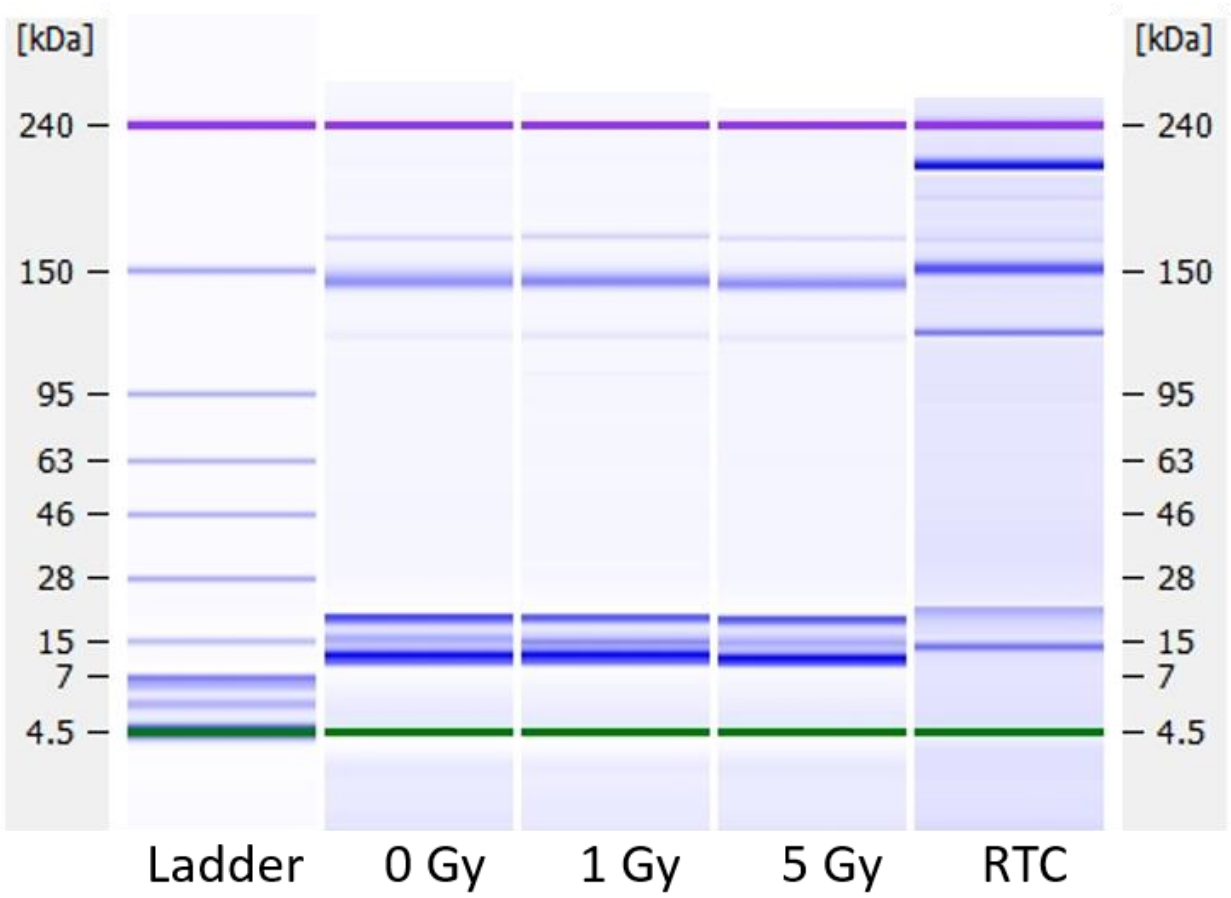

Figure 3.4 – Representative software-generated "gel" from automated electrophoresis showed no effect of radiation on fragmentation of collagen after 11-days at 1 or 5 Gy (12-week results were similar). Typical molecular weight of non-fragmented collagen is indicated by the 150 kDa band. A "smeared" band in the 150 kDa range would indicate fragmented collagen chains of lower molecular weight, but no smearing was found. Rat tail collagen (RTC) was used as a standard.

3.4 Discussion

We investigated the short-term and long-term effects of both space (1 Gy) and clinically-relevant (5 Gy) radiation exposure on cyclic and monotonic bone mechanics in the mouse vertebra. we found a loss of cyclic mechanical properties, such as lower fatigue life and elastic stiffness, occurred irrespective of radiation exposure, and only in the long-term (i.e. 12-weeks). We were able to attribute the mechanical losses primarily to losses in cancellous microarchitecture by comparing the results from groups without radiation to groups with radiation.

Without irradiation, between 11-days and 12-weeks, we observed a loss of trabecular bone quantity and microarchitecture, as well as cyclic whole-bone mechanics. The quantity and structural changes were consistent with typical aging in the C57BL/6J, male mouse of this age (~4 to ~7 months old) (Glatt et al. 2007; Halloran et al. 2002; Alwood et al. 2012), mainly a decline in trabecular number and connectivity and a slight loss of cancellous bone volume fraction. However, it was unclear if one factor, bone quantity or microarchitecture, was primarily responsible for the resulting mechanical loss.

When compared to the short-term and long-term results of a 5 Gy dose of irradiation, the primary factor impacting the cyclic mechanics became more clear. With a 5 Gy dose of irradiation, after 11-days, there was a rapid loss in bone quantity, which exceeded the amount observed with aging alone. This finding was consistent with previous literature reporting a rapid loss of cancellous tissue in as little as 10-days with whole-body gamma-radiation (doses ranged from 1 to 6 Gy) (Kondo et al. 2009; Willey et al. 2010; Alwood et al. 2012; Green et al. 2013; Turner et al. 2013). But, interestingly this early loss of bone tissue did not coincide with any reduced cyclic mechanics at 11-days. After 12-weeks the bone quantity remained unchanged compared to 11-day losses, however microarchitecture losses matched or exceeded those found with aging alone. This reflected the mechanical losses also observed at 12-weeks. Therefore, we have attributed the loss of cyclic mechanics primarily to a poor trabecular structure, which has been noted by other authors reporting on the importance of trabecular number and connectivity in retaining bone strength demonstrated with computer models (Silva and Gibson 1997; Guo and Kim 2002). A decrease in cortical thickness with aging and irradiation could also play a role in the mechanical deficits, which has been reported for human bone after exposure to radiotherapy (Okoukoni et al. 2017).

Interestingly, a 2-fold increase in AGEs, indicating increased non-enzymatic collagen crosslinks with 5 Gy, also did not significantly impact the cyclic mechanics at 11-days. This was unexpected because AGEs have been associated with reduced post-yield properties and energy absorption in cortical bone (Wang et al. 2002; Tang et al. 2009; Tang, Zeenath, and Vashishth 2007). We hypothesized that an increase in collagen crosslink density would reduce fibrillar sliding (an energy dissipation mechanism) and enable microcracks to accumulate more quickly, ultimately leading to reduced cycles to failure or reduced post-yield properties (Acevedo et al. 2015). For example, Acevedo et al. (Acevedo et al. 2018) reported on reduced tissue-level ductility and whole-bone strength with a 27% increase in AGEs in a type 2 diabetes rat model. In contrast, our observed 64% increase in AGEs due to radiation exposure had no effect on cyclic or monotonic properties at 11-days. One explanation for the unaffected mechanics might be a difference between the type of AGEs produced from oxidation processes (radiation) (Saito and Marumo 2013) versus glycation processes (diabetes). It has been noted that not all AGEs

detected with the total fluoresce assay lead to non-enzymatic crosslinks (Karim and Bouxsein 2016). Therefore, it is possible that there are a greater percentage of AGEs capable of crosslinking in diabetes compared to radiation exposure. However, this explanation is unlikely because physical crosslink bonds in collagen have been measured with Raman spectroscopy, and a similar 2-fold increase was found after one week of clinically-relevant radiation exposure (5 to 20 Gy) (Gong et al. 2013; Oest et al. 2016). Therefore, we must consider that collagen crosslinks are not solely responsible for the mechanical differences and increased fracture rates observed with radiation therapy (Baxter et al. 2005; Overgaard 1988) or diabetes (Saito and Marumo 2010; Melton et al. 2008; Farr and Khosla 2016; Vestergaard 2007; Janghorbani et al. 2007), and further molecular mechanisms must be explored.

Although most of our results with a 1 Gy dose were not statistically significant, the results of 1 and 5 Gy, taken together, can still provide insight into space-related effects for two key reasons. First, the effects of spaceflight irradiation may actually reside between the lower and upper bounds of 1 and 5 Gy: (1) because astronauts could experience a dose up to 2 Gy (National Council on Radiation Protection and Measurements 2014; Willey et al. 2011a, 2011b), and (2) because spaceflight radiation contains high linear energy transfer (LET) particles (i.e. protons or iron-nuclei) which have been shown to mimic effects of low-LET (gamma x-ray photons) radiation, but to a greater degree (Hamilton et al. 2006; Alwood et al. 2010; Alwood et al. 2017). Second, the deficits in trabecular microarchitecture and bone volume fraction we observed in the vertebral body were not significant for 1 Gy, however the trabecular losses might be even larger (and may have been significant) in the appendicular skeleton, such as the tibia or femur. This larger loss of bone in the appendicular bones has been observed in murine studies investigating the effects of aging (Glatt et al. 2007) or irradiation (Kondo et al. 2009). Glatt et al. reported greatest losses of cancellous tissue in the distal femur with aging compared to the vertebral body, and suggested this may be due to the greater importance of trabeculae in load transfer within the vertebral body compared to epiphyses of long-bones. With irradiation, Kondo et al. reported a significant loss of trabecular bone volume fraction and microarchitecture with a dose of 1 Gy in the proximal tibia, but similar losses on the vertebra were only reported for 2 Gy. This greater loss in the appendicular skeleton is also observed in humans when exposed to weightlessness (Lang et al. 2004).

For spaceflight applications, our findings suggest that to retain pre-flight bone strength and fatigue life properties, maintaining the microarchitecture of the bone should be a priority, especially when considering current and future countermeasures. Currently, the astronauts combat bone loss due to weightlessness (Lang et al. 2004; LeBlanc et al. 2007) with daily load-bearing exercise regimen, or a bisphosphonate treatment (anti-resorptive), or both (Leblanc et al. 2013). Although these regimens have been effective, there are lingering concerns about long-term treatment of astronauts with bisphosphonates. There is some evidence that shutting down bone resorption with a bisphosphonate allows for faster accumulation of microcracks and altered tissue quality (Acevedo et al. 2015), possibly leading to greater risk of fracture (Odvina et al. 2005; Goh et al. 2007; Lenart, Lorich, and Lane 2008). This concern, taken together with our initial concern about radiation-induced collagen crosslinks and tissue quality, make a bisphosphonate treatment given in a radiation environment, such as deep-space, appear risky. However, our findings suggest a bisphosphonate treatment, or any other treatment that can protect the cancellous microarchitecture, may outweigh the risk of any tissue quality degradation. Our results support the use of a bisphosphonate because it will not allow for the

microarchitecture to deteriorate, and also suggest that space-relevant doses (~1 Gy) of radiation exposure does cause any deficits in tissue quality and therefore should not cause any greater concern for faster accumulation of microcracks. Once the number and connectivity of the trabecular network are lost, whether from radiation exposure or weightlessness, it is unlikely that the astronaut will recover this architecture (without significant drug interventions which have not yet been validated) (Altman et al. 2015) and will remain at risk for fracture during and after the mission. A countermeasure capable of protecting the architecture, either via anti-resorptive drug (Willey et al. 2010) or diet (Schreurs et al. 2016), is highly encouraged for long-term astronaut bone health.

For clinical applications, protecting the bone from radiation-induced microarchitecture degradation also will likely reduce the risk of fractures observed following radiation therapy. Recall, patients undergoing radiation therapy receive a localized dose of 2 Gy per day (5-day week) for 5 weeks, for a total of ~50 Gy, where the surrounding tissue, such as bone, may receive up to half of this dose (Willey et al. 2011a). Our 5 Gy, whole-body irradiation results are most relevant to the application of radiotherapy. Cancer patients with risk of bone metastases are often given a combined treatment of radiation plus bisphosphonate (Tolia et al. 2014). However, a bisphosphonate treatment might also be helpful to radiotherapy patients with cancer where radiation exposure to the bone is unavoidable, such as the anal, cervical, or rectal cancers. Arrington et al. (Arrington et al. 2010) reported a combined treatment of zoledronate and radiation exposure was effective in retaining bone strength in a mouse model. Furthermore, our findings on the influence of trabecular microarchitecture on cyclic and static mechanics support previous findings from our lab on the importance of trabecular architecture in human vertebral strength (Fields and Keaveny 2012). And that the population of osteopenic individuals, who are missed for osteoporosis treatment and suffer vertebral (or hip) fractures, could be identified by diagnostic tools capable of assessing the trabecular architecture.

This study was unique in that the radiation administered spanned both space and clinically-relevant doses, however this also generates limitations within our model with respect to both applications. First, for spaceflight, the radiation exposure will also include high-LET radiation (e.g. ^{56}Fe ions), which may have a greater impact to the bone in the long term than low-LET radiation (e.g. gamma-rays or protons) (Alwood et al. 2017). From a LET perspective, our results may under-estimate the true response of bone to spaceflight irradiation. Also, a spaceflight radiation dose will be received chronically, over the course of a mission, not acutely (all at once), as we have done. From an exposure-rate perspective, our results may over-estimate the response of the skeleton to spaceflight irradiation. Second for clinical applications, we have administered a dose on the lower end of what is typically given in radiation therapy (Willey et al. 2011a), and also administered a whole-body instead of localized dose. Therefore, it is possible that there are systemic effects driving some of the observed changes, that would not typically be observed with a localized dose. It is also possible that with a greater dose, the material quality may be further impacted with an even higher level of collagen crosslinks, such that they do significantly contribute to degraded tissue quality and increased risk of fracture.

In summary, our findings suggest that with respect to irradiation and aging, bone mass alone is not sufficient to assess mechanical effects, and differences in microarchitecture or possibly the bone spatial distribution must also be evaluated. Also, molecular-level changes to the collagen do not manifest in degraded tissue quality. On-going work is using finite element analysis to identify which architecture parameter (e.g. trabecular number, connectivity, spacing,

cortical thickness) can best explain the reduced mechanics observed. We plan to look at the tissue level stress and strain values, to see if these are elevated in the 12-week groups, and if there is a correlation with a particular architectural parameter.

3.5 Supplemental Material

Isolation of collagen protein from bone

Lumbar verterbra (L3) samples were demineralized over 3-weeks in 0.5M ethylenediaminetetraacetic acid (EDTA) with the solution changed every 2-3 days. Demineralized samples were defatted for 24-hours in a 1:1 solution of chloroform and methanol and then soaked in 100% methanol for another hour. Samples were then dried in a desiccator overnight. Dried samples were flash-frozen with liquid-nitrogen and crushed into bone powder using a mortar and pestle. Bone powder was then lyophilized (Sequence: -38°C for 180 min, -38°C at 120 mTorr for 90 min, -20°C at 770 mTorr for 900 min, -10°C at 930 mTorr for 270 min, and 23°C at 120 mTorr for 55 min) (VirTis AdVantage Plus Benchtop Freeze Dryer XL Model, SP Scientific, Stone Ridge, NY). For tissue digestion, the powder was added to a solution of 0.5M acetic acid and pepsin (1mg of pepsin per 10 mg of bone powder) and placed on a rocker at 4°C for 72-hours. To neutralize the digestion process 5M NaOH was added until pH was neutral (pH = 6 to 8). To remove non-soluble collagen and non-collagenous proteins, samples were centrifuged for 30-minutes at 13,000 RPM. The supernatant, containing the soluble collagen, was collected. To precipitate the collagen out of solution, solid NaCl was added to a final concentration of 2M NaCl and placed on a rocker at 4°C for 24-hours. Samples were centrifuged for 30-minutes at 13,000 RPM. The supernatant was removed and the pellets were resuspended in 200 µL of 0.5M acetic acid. Samples were then lyophilized and stored at -20°C until electrophoresis with the bioanalyzer.

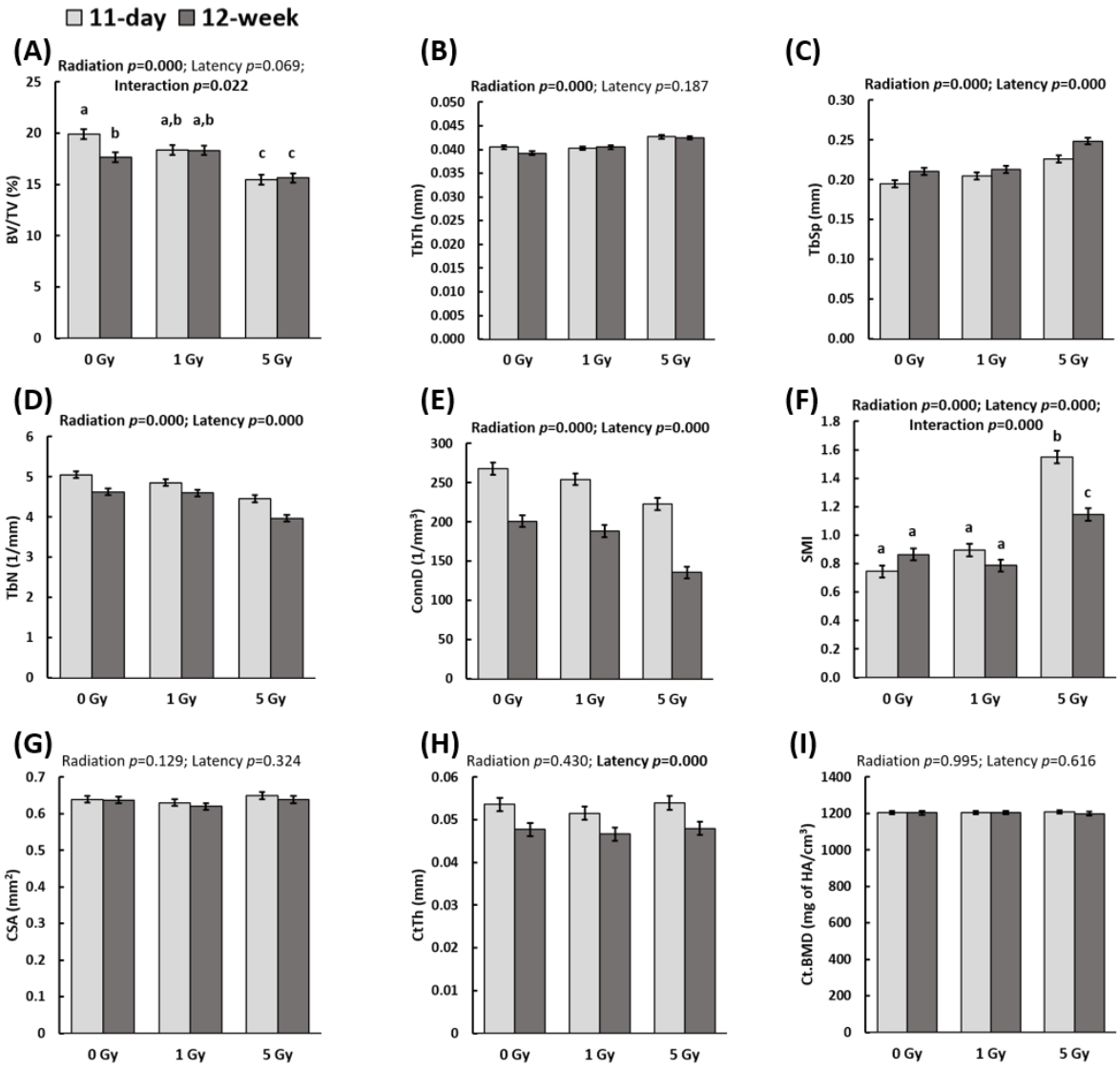

Figure 3.5 – Effects of 0, 1, & 5 Gy acute, whole-body, gamma-radiation after an 11-day or 12-week latency period (time after irradiation until sacrifice) on quantity and microarchitecture of trabecular and cortical bone measured by micro-CT. Least-square means are presented with error bars signifying standard error. Significance is indicated for radiation, latency, or interaction is indicated by bold text. For all results indicating significant radiation effects, only 5 Gy is significantly different from 0 and 1. The interaction term was only significant for Tb BV/TV and SMI; bars with the same letter are not significantly different.

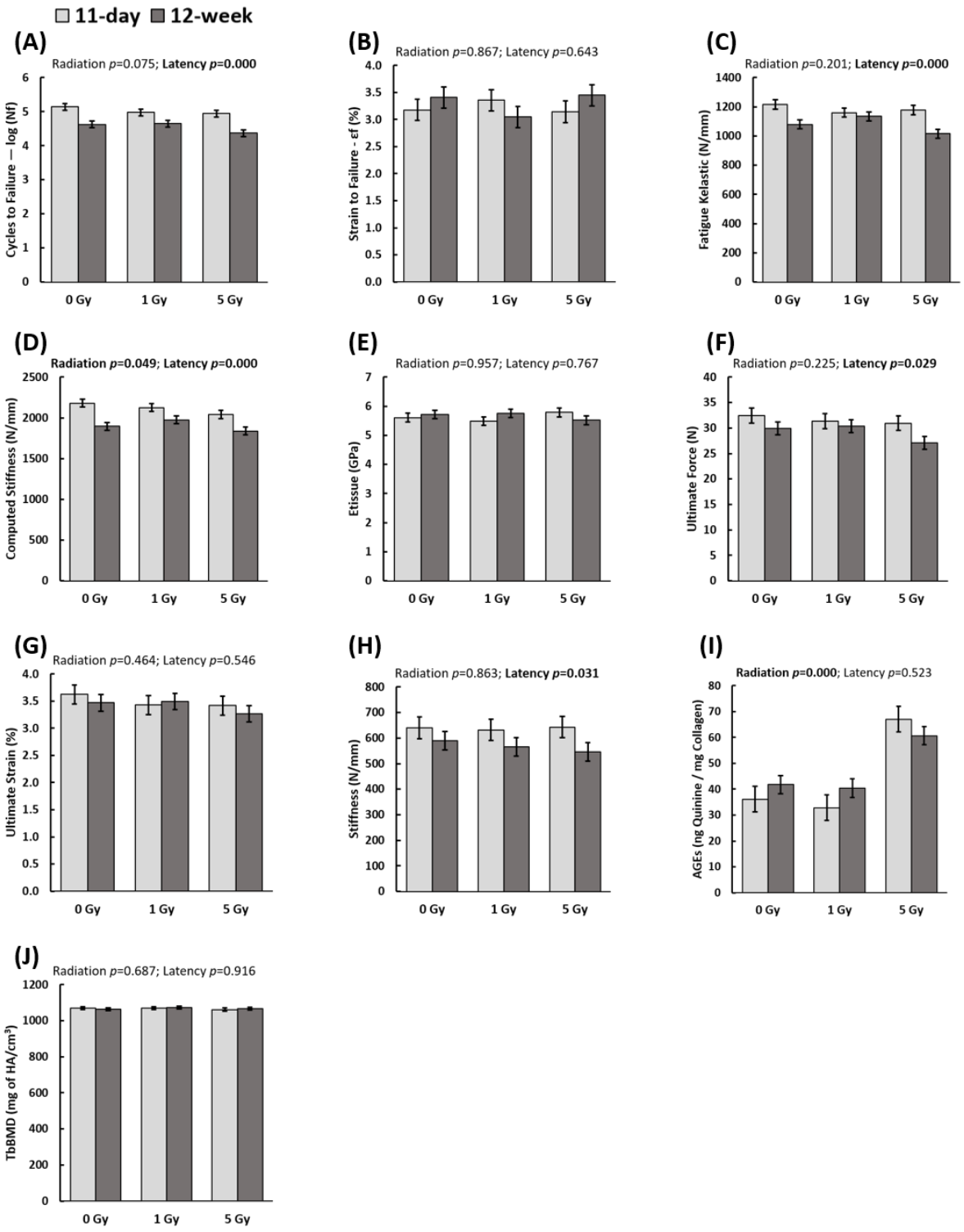

Figure 3.6 – Effects of 0, 1, & 5 Gy acute, whole-body, gamma-radiation after an 11-day or 12-week latency period (time after irradiation until sacrifice) on mechanical and biochemical measures. Least-square means are presented with error bars signifying standard error. Significance is indicated for radiation or latency by bold text, no interaction terms were significant. For all results indicating significant radiation effects, only 5 Gy is significantly different from 0 and 1.

Chapter 4 – Effects of High Levels of *ex vivo* Ionizing Radiation Exposure on Collagen Structure and Mechanical Properties of Mouse Vertebrae[2]

4.1 Introduction

For a variety of clinical applications, bones are exposed to a wide range of ionizing radiation doses, some doses being very high. *In vivo*, radiotherapy treatment results in an accumulated localized dose of 50 Gy in cancer patients. *Ex vivo*, bone allografts are sterilized prior to transplantation at a dose of ~35,000 Gy. While these high-dose applications are critical for overall patient health and safety, high levels of ionizing radiation exposure have been shown to put patients at an increased risk of fracture (Okoukoni et al. 2017; Bazire et al. 2017). For example, for women with anal, rectal or colon cancer, those treated with radiation therapy were up to 3.2-times more likely to suffer a pelvic fracture than those without radiation therapy (Baxter et al. 2005). Furthermore, for patients with implanted bone allografts, those allografts sterilized with radiation were twice as likely to fail compared to those sterilized using other methods (Lietman et al. 2000). The increased risk of fracture clinically has led to widespread research into the effect of high levels of ionizing radiation exposure on mechanical and biochemical properties of bone.

In order to assess the effect of ionizing radiation exposure on bone without the confounding influence of cellular activity, numerous *ex vivo* studies on cortical or cancellous bone have demonstrated that ionizing radiation exposure degrades mechanical properties and collagen integrity. Compared to non-irradiated bone, the post-yield properties (ultimate strain, ultimate strength, fracture toughness, work-to-failure) of irradiated bone are significantly reduced (Burton et al. 2014; Currey et al. 1997; Barth et al. 2010; Barth et al. 2011; Nguyen, Morgan, and Forwood 2007; Akkus and Rimnac 2001b). As an intact collagen network dictates these post-yield properties, mechanical degradation has been attributed to collagen network degradation (Zioupos, Currey, and Hamer 1999; Nyman, Reyes, and Wang 2005; Burstein et al. 1975). Irradiation is believed to disrupt the collagen network either indirectly through an increase in radiolysis-induced collagen crosslinks, or directly via photon-induced fragmentation of the collagen backbone. However, it is unclear which of the aforementioned collagen structural changes (crosslinks or fragmentation) accounts for the observed reduced post-yield properties. Previous studies provide confounding results: while some suggest deleterious changes in bulk material properties were dominated by collagen crosslinking (Barth et al. 2010; Barth et al. 2011; Oest et al. 2016; Gong et al. 2013; Bailey, Rhodes, and Cater 1964), others indicate it was caused by collagen chain fragmentation (Akkus and Belaney 2005; Burton et al. 2014). Furthermore, while these studies have reported on the effects of irradiation on cortical or cancellous tissue individually, we are aware of no biomechanical studies that have addressed the effect on whole-bones containing both cortical and cancellous tissue. Thus, in order to characterize the effect of irradiation on mechanics and more completely understand the resulting collagen damage driving mechanical differences, we sought to investigate the dose-dependent, non-cellular effect of *ex vivo* ionizing radiation exposure on whole-bones by performing biomechanical testing and collagen network assessment on murine vertebral bodies. By understanding the molecular mechanisms, our findings will ultimately help identify targets for preventive measures for *ex vivo* and *in vivo* applications.

[2] Chapter 4 data collection, data analysis, and writing were a collaborative effort with Shannon R. Emerzian

4.2 Materials and Methods

Study Design

In this study, we conducted an x-ray radiation experiment on excised mouse lumbar vertebrae (L3-S1) using a range of doses that span from radiotherapy (50 Gy) to sterilization (35,000 Gy) with both mechanical and biochemical characterization. Vertebrae used for collagen characterization with biochemical assays (L3 and S1) were irradiated and then tested; no sample preparation or micro-CT imaging was conducted. Vertebrae used for mechanical testing (L4 and L5) required additional steps of preparation than vertebrae used for biochemical testing; they were machined, irradiated, imaged with micro-CT, and tested.

Animals

Forty-eight female, 20-week old (skeletally-mature) C57BL/6J mice (Jackson Labs, Sacramento, CA) were randomly assigned to five groups (N = 9-10). Mice were euthanized prior to *ex vivo* irradiation. All procedures were approved by the University of California Berkeley Animal Care & Use Committee.

Specimen preparation

After humane sacrifice, lumbar and sacral vertebrae (L3 to S1) were excised from the mouse for irradiation prior to mechanical or biochemical testing. All vertebrae were gently cleaned of soft tissue, wrapped in saline-soaked gauze (Gibco PBS 1X, pH 7.4), and stored at -20°C. Only vertebra used for mechanical testing, L4 and L5, were modified per Pendleton et al. (Pendleton et al. 2018A; submitted for publication, Chapter 2). In brief, endplates and posterior elements were removed to isolate the vertebral body and ensure plano-parallel testing surfaces. There were four freeze-thaw cycles in total for L4 and L5 vertebrae (-20°C to room temperature), one between each step: dissection, specimen preparation, irradiation, imaging, and mechanical testing.

Ex Vivo X-Ray Irradiation

After specimen preparation, *ex vivo* irradiation was performed. All vertebrae from each spine (L3-L5) were randomly assigned to one of five dose groups for x-ray irradiation: 0, 50, 1,000 17,000 or 35,000 Gy. Irradiation was performed at the Advanced Light Source (ALS) synchrotron facility at Lawrence Berkeley National Laboratory using the x-ray synchrotron micro-tomography beam line (8.3.2). Irradiation was achieved at 21 keV and 500 mA for a dose rate of 13.3 Gy/sec. See Section 4.5 Supplemental Material for dose calculation details. Specimens were kept hydrated during irradiation via saline-soaked gauze.

Quantitative micro-CT Imaging

After irradiation, the L4 and L5 specimens were imaged with quantitative micro-CT (µCT 50, Scanco Medical AG, Bruttisellen, Switzerland) using a 10-µm voxel size (55 kV, 109 µA, 1000 projections per 180°, 500 ms integration time). Micro-CT images of the L4 and L5 specimens were analyzed for height (ImageJ 1.51h, Java 1.6.0). Additionally, to confirm successful random sample distribution, the L5 specimens were evaluated for three-dimensional architecture of the trabecular compartments (Scanco Evaluation Software v6.0). After manual

segmentation of the trabecular compartment — using a lower threshold of 300 grayscale units and a Gaussian filter with sigma of 0.5 and support of 2 — the following parameters were measured: trabecular bone volume fraction (Tb.BV/TV), number (Tb.N), thickness (Tb.Th), and separation (Tb.Sp).

Mechanical Characterization

After micro-CT imaging, uniaxial compressive monotonic (L4) and cyclic (L5) mechanical testing was performed. Monotonic testing was conducted at a platen displacement rate of 0.01 mm/sec. Force-displacement data were collected (1,000 Hz) and custom code was used to obtain whole-vertebral stiffness, ultimate force (strength), ultimate strain, and work-to-fracture (**Figure 4.1 A**). Due to the variation in cross-sectional area of the vertebral body from cranial to caudal ends, the elastic modulus and ultimate stress were not calculated.

Cyclic testing was conducted using methods described in detail elsewhere (Pendleton et al. 2018A; submitted for publication, Chapter 2). In brief, prior to testing individualized minimum and maximum cyclic loading forces, F_{min} and F_{max}, were calculated for each specimen based on micro-CT generated finite element models, such that all specimens were initially loaded to the same initial elastic strain. After these calculations, specimens were cyclically loaded in uniaxial compression between the individualized F_{min} and F_{max} value with a sinusoidal waveform at 8 Hz until failure (TA ElectroForce 3200, Eden Prairie, MN; 50 lb. load cell, resolution of ± 0.1N). Testing was conducted at room temperature in a saline-water bath to maintain hydration for the duration of the test. Force-displacement data was collected (1,000 Hz), and custom code was used to obtain fatigue properties including: fatigue life (N_f), strain-to-failure (ε_f), and specimen elastic stiffness ($K_{elastic}$, refer to Section 2.2 Materials and methods and **Figure 2.7** for details) (**Figure 4.1 B**). Cyclic testing was not performed for specimens where the F_{max} calculated by the finite element model exceeded the average strength observed during monotonic testing of the same dose group. Here, where the monotonic strength exceeded the prescribed cyclic F_{max}, these specimens would have failed within one loading cycle, similar to a monotonic test. Therefore, these specimens were assigned a fatigue life value of 1, a strain-to-failure value equaling the monotonic ultimate strain of the same dose group, and an elastic stiffness value of 0 (elastic stiffness is typically calculated after several thousand loading cycles).

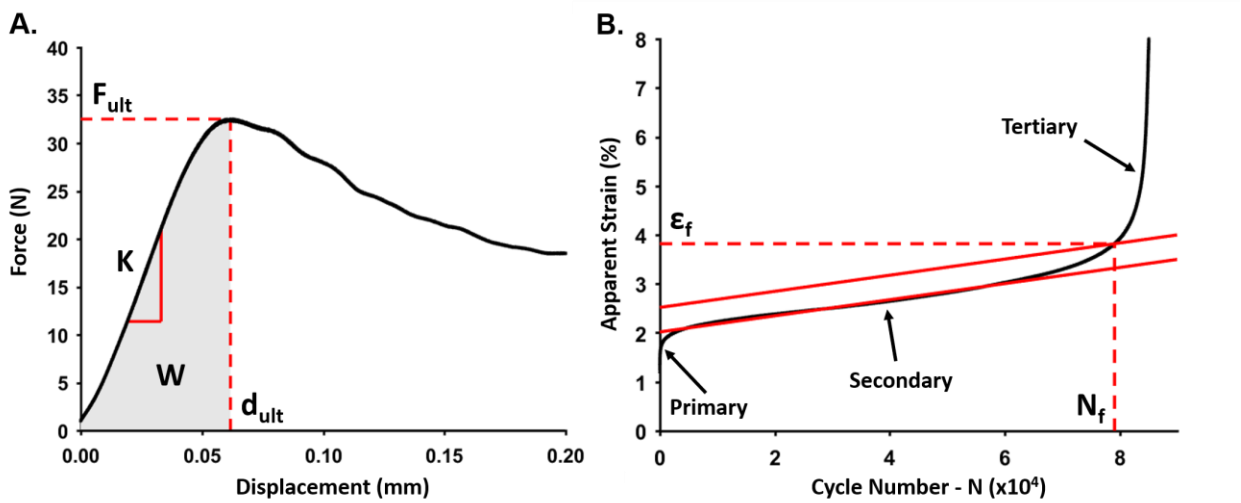

Figure 4.1 – Plots generated from mechanical testing of vertebral specimens. (A) For monotonic compression testing, a force-displacement curve was plotted to obtain stiffness (K), ultimate force (F_{ult}), ultimate strain (ε_{ult}), and work to fracture (W; area in gray). Ultimate strain was found by normalizing ultimate displacement (d_{ult}) by the specimen height. (B) For cyclic testing, maximum apparent strain per cycle was plotted to obtain fatigue life (N_f) and strain to failure (ε_f). N_f and ε_f are found from the point of intersection between the apparent strain versus cycles curve, and a line offset by 0.5% strain parallel to the line of best fit for the secondary region (Bowman et al. 1998; Brouwers et al. 2009). Additionally, elastic stiffness ($K_{elastic}$) was found from fatigue testing. $K_{elastic}$ is an average stiffness over ± 500 cycles centered about the maximum value of stiffness, which typically occurred after a few thousand cycles of loading. $K_{failure}$ is the stiffness at the failure cycle (N_f) (Pendleton et al. 2018A; submitted for publication, Chapter 2).

Biochemical Characterization

After irradiation, two biochemical tests (N = 4 specimens for each test) were conducted to assess the primary molecular mechanisms that are thought to alter bone mechanics: (1) the accumulation advanced glycation end-products (AGEs), representative of non-enzymatic collagen crosslinks; and (2) fragmentation of the collagen backbone.

To assess collagen cross-linking, advanced glycation end-products (AGEs), which form non-enzymatic crosslinks through oxidation or glycation processes between and within collagen fibrils (Knott and Bailey 1998; Karim and Bouxsein 2016), were assessed via a fluorometric assay on the S1 vertebrae (protocol adapted from Sell et al. (Sell and Monnier 1989)). Each S1 specimen was demineralized in 0.5 M ethylenediaminetetraacetic acid (EDTA) and hydrolyzed in 12N HCl at 120°C for 3 hours to break down peptide bonds. The hydrolysate was then resuspended in PBS (0.1X) and pipetted in triplicate onto a black-walled 96 well plate. The non-enzymatic collagen crosslink content was determined using fluorescence readings taken using a microplate reader at wavelengths of 370 nm excitation and 440 nm emission. The readings were standardized to a quinine-sulfate standard (quinine dissolved in H_2SO_4) and then normalized to the amount of collagen present in each sample. The amount of collagen for each sample was approximated by the amount of hydroxyproline (Barth et al. 2011; Tang, Zeenath, and Vashishth 2007).

To assess collagen fragmentation, we used an automated electrophoresis assay (2100 Bioanalyzer, Agilent Technologies, Santa Clara, CA) to assess the molecular weight distribution

of isolated collagen from the L3 vertebrae. To isolate collagen for this assay, we adapted methods used by Burton et al. (Burton et al. 2014) (Section 4.5 Supplemental Material). The collagen extracted from each sample was then dissolved in 1X PBS, mixed with additional reagents (Agilent Technologies Protein 230 Manual), and loaded on a bioanalyzer chip for automated electrophoresis. Rat tail collagen (Sigma Aldrich) was run as a standard. From this assay, the size and amount of collagen protein could then be assessed in two ways: (1) visually with a software-generated "gel" and (2) quantitatively with a software-generated fluorescence-unit (FU) chart, called an "electropherogram" (Agilent 2100 Expert software). The nominal size of a type-I collagen, either alpha-1 or alpha-2, chain is between 130-150 kDa. To identify chain fragmentation, we looked for evidence of less protein in this range, and a wider distribution of molecular weights. On the gel, this can be observed as a lighter-colored band or smeared band at ~150 kDa. On the electropherogram, fragmentation can be observed when the peak150 kDa is diminished, indicating fewer fluorescence units and therefore fewer collagen chains of the nominal size.

Statistics

We conducted a one-way Analysis of Variance (ANOVA) for irradiation (JMP v13.0, SAS Institute). For terms with $p < 0.05$, a Dunnett's post-hoc test was used to identify significant differences compared to the control (0 Gy). Values listed in the text are reported as mean ± standard deviation, unless otherwise noted.

4.3 Results

Mechanical Characterization

For monotonic compression testing, the strength and ultimate strain were lower than the control group for radiation exposure of 17,000 and 35,000 Gy, while 50 and 1000 Gy were similar to the control group. Strength was 50% and 73% lower for 17,000 and 35,000 Gy, respectively, compared to the control (38.9 ± 5.3 N; $p < 0.001$) (**Figure 4.2 A**). Ultimate strain was 58% and 77% lower for 17,000 and 35,000 Gy, respectively, compared to the control (5.4 ± 2.3 %; $p < 0.05$) (**Figure 4.2 B**). Work-to-fracture was 76% and 92% lower for 17,000 and 35,000 Gy respectively, compared to the control (1.7 ± 0.7 mJ; $p < 0.01$). In contrast, monotonic stiffness remained unchanged for all radiation dose groups compared to the control group (691 ± 275 N/mm; $p = 0.67$) (**Figure 4.2 C**).

Similar to the monotonic properties, the cyclic properties for 50 and 1,000 Gy were not significantly different compared to the control: fatigue life (5.2 ± 0.4 log(cycles); $p = 0.50$), strain to failure (3.8 ± 1.0 %; $p = 0.41$), and elastic stiffness (1273 ± 162 N/mm; $p = 0.31$) (**Figure 4.2 D-F**). The monotonic strength of the 17,000 and 35,000 Gy groups were less than the finite element model prescribed cyclic loading force, F_{max}. Cyclic testing was not conducted for these two groups.

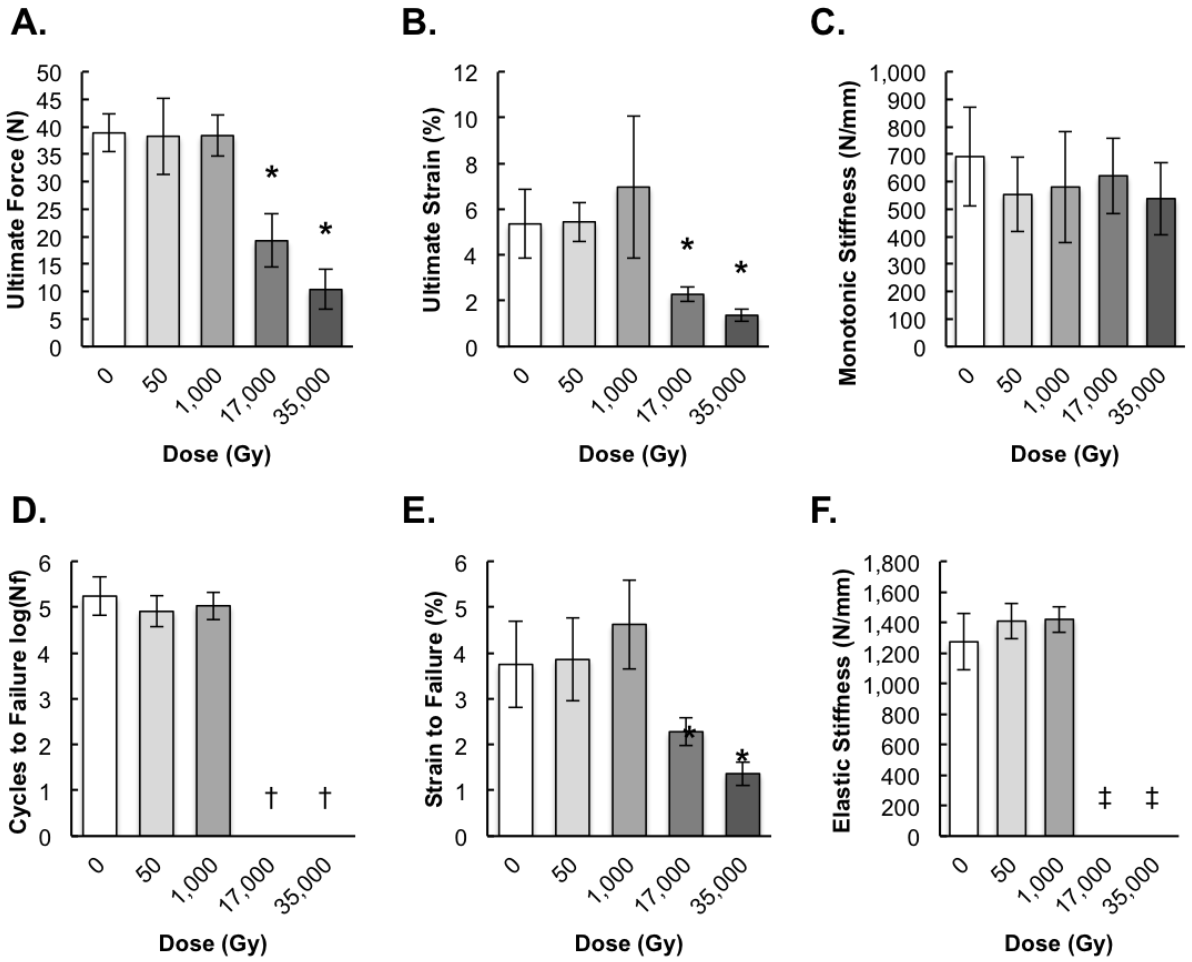

Figure 4.2 – Effect of *ex vivo* x-ray radiation exposure on monotonic (A-C) and cyclic (D-F) mechanical properties of mouse lumbar vertebrae. Data are shown as least-square means. Error bars represent 95% confidence intervals. Cyclic testing was not conducted for 17,000 and 35,000 Gy groups because the prescribed cyclic loading force was greater than the same group's measured monotonic strength. Thus, cyclic tests for 17,000 and 35,000 Gy were considered monotonic in nature and therefore assigned value of 1 for cycles to failure, a strain-to-failure value equal to the ultimate strain of the same dose group, and an elastic stiffness value of 0. * $P < 0.001$ using Dunnett's post-hoc test. † $P < 0.0001$ for assumed 1 cycle to failure. ‡ Elastic stiffness not computed.

Biochemical Characterization

Compared to the control, the relative amount of AGEs was greater for all radiation groups. However, collagen fragmentation was only observed at doses of 17,000 and 35,000 Gy, consistent with the reduced mechanical properties also observed only at these doses. AGEs were higher for all radiation doses in a dose-dependent manner: by 67%, 95%, 96%, and 108% for 50, 1,000, 17,000 and 35,000 Gy, respectively, compared to the control (42.2 ± 2.3 ng quinine / mg collagen; $p < 0.001$). However, the greater amount of AGEs measured at 50 and 1,000 Gy did not coincide with a reduction in strength or any other mechanical property (**Figure 4.3**). In contrast, collagen fragmentation (i.e. a lower amount of nominal size, ~150 kDa, collagen proteins) was found to occur at 17,000 and 35,000 Gy, where a reduction in strength was also observed. Fragmentation at these doses was observed on both the software-generated gel (**Figure 4.4 A)** and electropherogram (**Figure 4.4 B**). On the gel, a dark band was visible at 150 kDa for

samples of 0, 50, and 1,000 Gy. This band began to lighten at 17,000 and 35,000 Gy, indicating fewer collagen proteins of this chain size. Also, a "smearing" of bands was observed below 150 kDa, which suggests that there was a greater amount of collagen fragmented chains with lower molecular weights. On the electropherogram, the same result can be observed. The peak fluorescence unit found at 150 kDa for 17,000 Gy went down by 74% compared to the control (460 ± 72 FU; $p < 0.02$). The fragmented collagen at 17,000 Gy and above coincides with the loss of strength observed at 17,000 Gy and above (**Figure 4.3**).

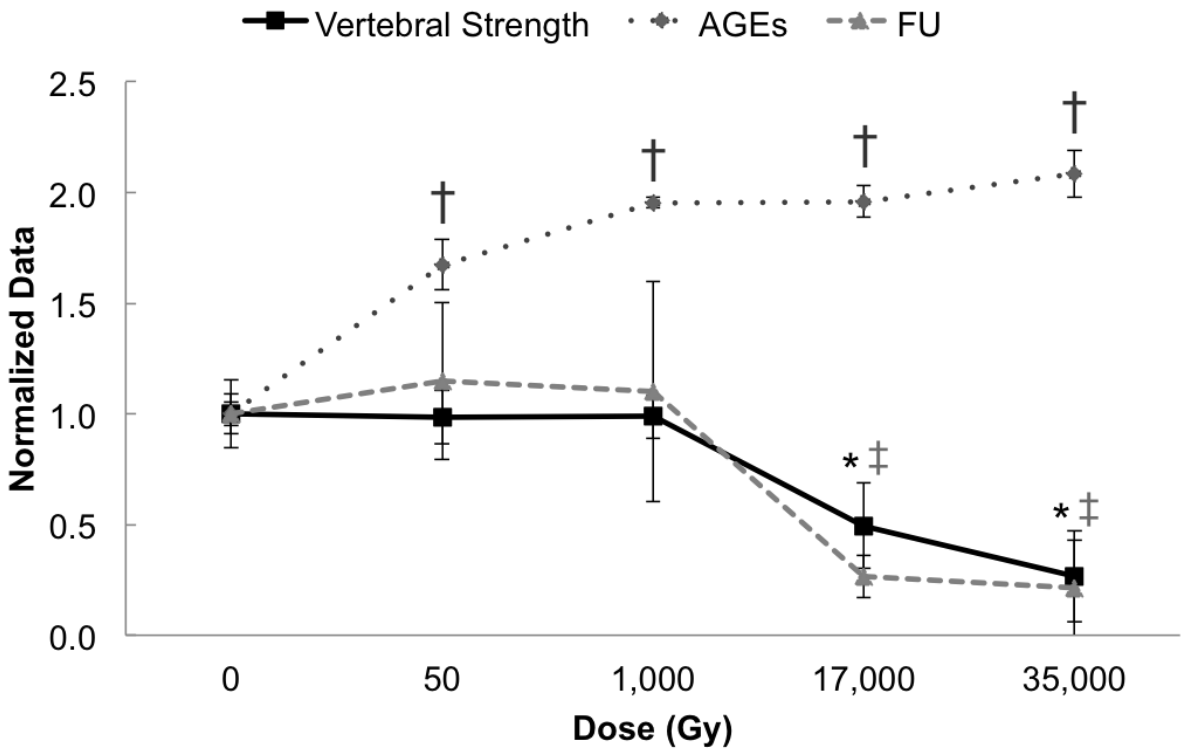

Figure 4.3 – Comparison of vertebral strength with two primary mechanisms of collagen degradation: (1) collagen crosslinks represented by AGEs, and (2) collagen fragmentation indicated by a lower fluorescence unit value indicating less collagen with a nominal chain length, by radiation dose. Data are normalized by the control values: vertebral strength 38.9 ± 3.5 N, AGEs 42.2 ± 2.2 ng quinine/mg collagen, and fluorescence units 460.1 ± 70.9 FU. Data are shown as normalized least-square means, with error bars signifying 95% confidence intervals analyzed by ANOVA with Dunnett's post-hoc test, $p < 0.05$. * represents $p < 0.0001$ for vertebral ultimate strength; † represents $p < 0.0001$ for AGEs; ‡ represents $p < .001$ for FU.

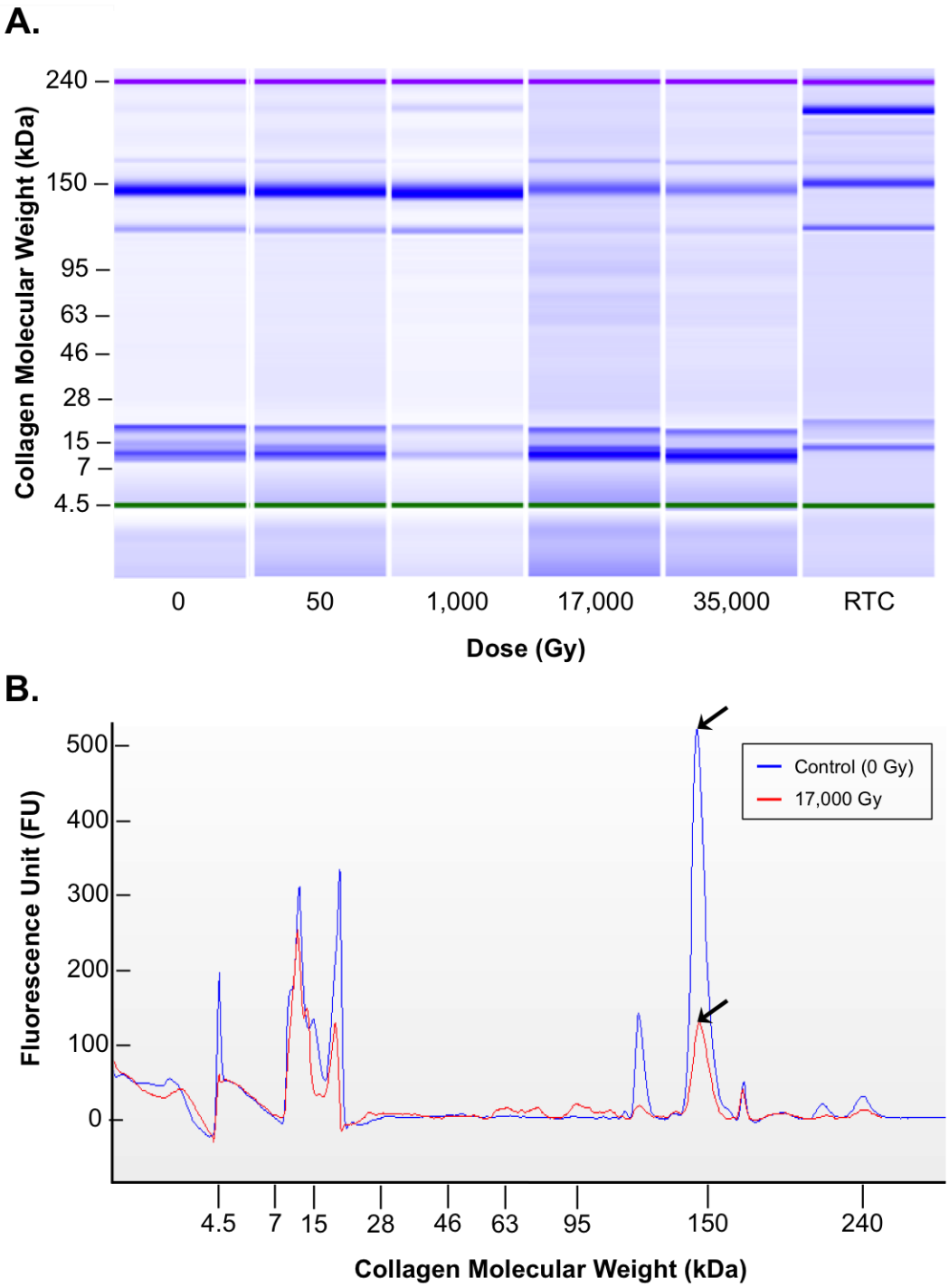

Figure 4.4 – Output from the automated electrophoresis assay which indicates collagen fragmentation occurred with a radiation dose of 17,000 Gy or higher. (A) A representative gel with a dark band visible at 150 kDa for samples of 0, 50, and 1,000 Gy. The band was lighter at 17,000 and 35,000 Gy, indicating fewer collagen proteins of this chain size. Also, a "smearing" of the band below 150 kDa indicates more chains of varied and lower molecular weights, which suggests a greater amount of fragmented collagen. (B) A representative electropherogram with the results of 0 and 17,000 Gy overlaid. The peak fluorescence unit found at 150 kDa for 17,000 Gy (red) is significantly lower compared to the 0 Gy control (blue).

Quantitative micro-CT Imaging

There were no significant differences in bone quantity or microarchitecture. Trabecular bone volume fraction (18.79 ± 0.94%, $p = 0.197$), number (3.92 ± 0.13 1/mm, $p = 0.352$), and separation (256.97 ± 8.81μm, $p = 0.47$) were the same for all dose groups. ANOVA results for trabecular thickness were significant (ANOVA $p = 0.036$), however the post-hoc analysis found no differences between any group compared to the control (50.17 ± 1.0 μm; $p > 0.05$ for all groups).

4.4 Discussion

These results demonstrate that the reduction in monotonic post-yield properties (ultimate strength, ultimate strain, work to fracture) and cyclic properties (fatigue life) for whole-bones exposed to x-rays at 17,000 Gy and above were dominated by the increase in fragmentation of the collagen backbone and were negligibly influenced by the increase in AGEs (crosslinks).

Similar to numerous other high-dose radiation sterilization studies (30,000 ± 5,000 Gy), we observed reduced monotonic post-yield properties (e.g. ultimate strength, ultimate strain, and work to fracture) and cyclic properties (e.g. fatigue life) for doses of 17,000 Gy (Currey et al. 1997) and 35,000 Gy (Hamer et al. 1996; Cornu et al. 2000; Nguyen, Morgan, and Forwood 2007; Akkus, Belaney, and Das 2005; Akkus and Belaney 2005; Akkus and Rimnac 2001a), with no change in elastic properties (e.g. stiffness); together, these mechanical properties are indicative of collagen degradation (Burstein et al. 1975; Zioupos, Currey, and Hamer 1999). These previous studies have demonstrated that the nominal protein structure of collagen can change due to exposure to ionizing radiation in two ways (Colwell et al. 1996; Nguyen, Morgan, and Forwood 2007; Akkus and Belaney 2005; Burton et al. 2014). Directly, radiation photons split the molecular bonds in the collagen backbone, thereby fragmenting the collagen into smaller polypeptide chains. Indirectly, radiation energy causes the radiolysis of water molecules in the tissue, which releases free radicals that cause inter- and intra- molecular chemical crosslinks, referred to as non-enzymatic collagen crosslinks. Presently, it has been unclear which mechanism, collagen crosslinks (Barth et al. 2010) or collagen fragmentation (Burton et al. 2014), is primarily responsible for the reduced post-yield mechanical properties so widely observed. Here, we demonstrate that although collagen crosslinks increase nearly 2-fold with exposure to as little as 50 Gy of x-ray irradiation, this mechanism has no significant impact on the monotonic or cyclic mechanics. In contrast, collagen fragmentation is observed at 17,000 Gy and above, which directly corresponds to the reduced monotonic and cyclic mechanics also observed at these doses. Results from Burton et al. (Burton et al. 2014) and Akkus et al. (Akkus and Belaney 2005) further support collagen fragmentation, via photon energy breaking molecular bonds of the backbone, as the primary mechanism responsible for reduced mechanics at 33,000 and 36,400 Gy, respectively.

Our findings suggest that in order to maintain mechanical integrity following exposure to ionizing radiation, bone allograft specimens should be sterilized at a dose below 17,000 Gy unless safeguarded via a radioprotectant. For example, Currey et al. (Currey et al. 1997) reported reduced bending strength and work to fracture for cortical bone with irradiation doses at 17,000

Gy and above. We have shown that fragmentation and reduced mechanical properties can occur at 17,000 Gy, well below the recommended standard sterilization dose of 25,000 Gy (Singh, Singh, and Singh 2016; Campbell et al. 1994). These deficits suggest that in order to preserve allograft mechanical integrity, lower sterilization doses should be considered whenever possible. Furthermore, previous work has demonstrated that doses as low as 11,000 Gy can be used effectively to achieve the same sterility level as 25,000 Gy (Nguyen, Morgan, and Forwood 2011). Taken together with our work, this suggests sterilization at 11,000 Gy could be sufficient to both effectively sterilize the tissue and possibly maintain its structural integrity, although further studies are needed to validate this. Further *ex vivo* irradiation experiments are on-going to evaluate fragmentation and mechanical properties of doses spanning between 1,000 and 17,000 Gy. If the current recommended standard of 25,000 Gy sterilization is utilized, radioprotectants that target countering the effects of collagen fragmentation should be further investigated. For example, Willett et al. (Willett et al. 2015) demonstrated that using ribose pre-treatment as a radioprotectant (in order to preserve collagen network stability and offsetting inevitable collagen fragmentation) improved allograft mechanical properties (Willett et al. 2015; Woodside and Willett 2016). In contrast, our data suggest that radioprotectants focused on the reduction of crosslinks will likely have a small or negligible impact on bone mechanics, at least when loaded in compression.

Related, our findings suggest that higher levels of non-enzymatic collagen crosslinks may play a smaller role in reduced mechanical properties such as whole-bone strength than previously considered. For example, Acevedo et al. (Acevedo et al. 2018) reported a 40% decrease in collagen fibril ultimate strain (measured via Small Angle X-Ray Scattering, SAXS) and a 27% decrease in vertebral strength in a rat model with type-2 diabetes, which was associated with a 27% increase in AGEs, representing non-enzymatic collagen crosslinks. In contrast, in our current irradiation study we found up to 96% increase in AGEs and no difference in vertebral strength. Other studies on aging also reported no association between whole-bone strength and crosslinks for human trabecular bone (Follet et al. 2011). Taken together, it is possible that another molecular mechanism (e.g. altered non-collagenous proteins, or reduced water content (Granke, Does, and Nyman 2015)) is responsible for the reduced fibril strain and whole-bone strength found in the diabetic rat model. It is also possible that the deficit in whole-bone strength with diabetes is a result of structural changes rather than tissue quality. For example, changes in cortical quality such as increased cortical porosity have been associated with a higher number of fragility fractures for women with type-2 diabetes (Patsch et al. 2013). Understanding the role of elevated collagen crosslinks (or other mechanisms that could impact tissue quality) on bone mechanics is important in a number of applications, including: aging (Zimmermann et al. 2011), irradiation (Gong et al. 2013), and diabetes (Saito and Marumo 2015; Karim and Bouxsein 2016; Acevedo et al. 2018; Farlay et al. 2016), in order to appropriately target countermeasures and decrease risk of fracture. countermeasures.

There are some limitations to note in this study. First, we performed all mechanical testing, monotonic and cyclic tests, in compression. While this is the typical *in vivo* loading condition of the vertebrae, failure properties in tension or bending can be greatly affected by reduced collagen fibril stretching and sliding (Acevedo et al. 2018). The higher levels of collagen crosslinks observed at 50 and 1,000 Gy, which inhibit fibrillar motion, could have a significant impact on mechanical properties if tested in tension or bending, rather than in compression. There are some horizontal trabeculae in the vertebral body which primarily experience tension

when the whole-bone is loaded in compression (refer to **Figure 5.1**), and may have failed prematurely due to crosslinks. However, our results suggest that if this is true, the early failure of trabeculae in tension is not apparent at the whole-bone level. Second, with respect to the collagen fragmentation assay (i.e. automated electrophoresis with the bioanalyzer), we were unable to approximate the amount of total collagen collected per sample, as was done with the hydroxyproline measurement in the total fluorescence assay. Therefore, it is possible that the lower amount of collagen observed at 150 kDa in the 17,000 and 35,000 Gy groups (indicated by the lighter bad color on the gel) was because less collagen was initially loaded onto the chip well. However, this is unlikely for two reasons. First, collagen was extracted from the same vertebral level for all samples, so the starting level of collagen was the same and the exact collagen extraction protocols were executed for each sample. Second, we also observed "smearing" on the gel below 150 kDa for 17,000 and 35,000 Gy, an indication of a large variation in lower molecular weight collagen chains, likely due to random fragmentation of originally uniform size chains (**Figure 4.4 A**).

With potential application to radiotherapy treatment for cancer, for which there is an increased risk of pelvic fracture (Baxter et al. 2005), our results suggest an important role of the radiation exposure on cell-mediated effects as opposed to direct degradation of the matrix. Fracture risk is elevated when the bone biomechanical properties, such as strength or fatigue life, are reduced. These properties are influenced by factors such as bone quantity (bone mass), microarchitecture, and material quality of the bone tissue. In our *ex vivo* experimental study, the inactivity of cellular bone remodeling allowed us to analyze the impact of radiation exposure solely on the quality of the matrix material, without a change in bone quantity or microarchitecture. We found no significant differences in strength of fatigue life for doses relevant to radiation therapy (i.e. 50 Gy). Thus, the elevated fracture risk observed in radiotherapy is likely from the impact of irradiation on the cellular response. Previous *in vivo* irradiation studies of bone in a murine model relevant to radiotherapy or spaceflight have shown reduced cancellous bone mass and lower trabecular number and connectivity associated with hyperactive osteoclast activity (Oest et al. 2018; Kondo et al. 2009; Willey et al. 2011a)(Pendleton et al. 2018B, Chapter 3), pointing to changes in bone quantity and microarchitecture as more plausible explanations for increased fracture risk with radiotherapy. It is also possible that there is a cellular effect on the tissue material quality. Consistent with our findings, there is evidence from *in vivo* studies of elevated collagen crosslinks (Gong et al. 2013; Oest et al. 2016). However, we have demonstrated that this molecular change had no substantial impact on monotonic or cyclic mechanics.

In summary, we have quantified the level of direct (collagen fragmentation) and indirect (collagen crosslinks) effects of radiation exposure on the organic matrix that are observed in whole-bone over a range of clinically-applicable doses and identified the primary cause of mechanical degradation occurs from collagen fragmentation at 17,000 Gy and above.

4.5 Supplemental Material

Irradiation Dose Calculation

To estimate the radiation dose (measured in Gray, 1 Gy = 1 J/kg) absorbed by the vertebral bone samples, first the flux density (ψ) was measured. The flux density was then converted to energy density E_p (**Equation 5**):

$$E_p = \psi \times E \times 1.6 \times 10^{-19} \frac{J}{eV} \quad (5)$$

where E is the energy of the beam in eV. Thus, for the measured flux density of 83,000 photons s^{-1} μm^{-2} and beam energy of 20,000 eV, the energy density was

$$E_p = \left(83{,}000 \frac{photons}{s \times \mu m^2}\right) \times (20{,}000\ eV) \times 1.6 \times 10^{-19} \frac{J}{eV} = 2.656 \times 10^{-10} \frac{J}{s \times \mu m^2}$$

The transmission, T, of x-rays through a material of thickness l is expressed as (**Equation 6)**:

$$T = \frac{I}{I_o} = e^{-\mu \rho l} \quad (6)$$

where I_o and I are the transmitted and incident x-ray intensities, respectively, μ is the mass attenuation coefficient in cm^2/g for bone at an energy of 20 keV and ρ is the bone density. For the bone samples, the bone thickness l was taken to be 2.5mm. From ICRU Report 44, the mass attenuation coefficient for bone at 20 keV is μ = 4 cm^2/g (Turner 2007). The density of bone is ρ = 1.85 g/cm (Bartel, Davy, and Keaveny 2006). Thus, T was calculated as:

$$T = \frac{I}{I_o} = e^{-(4\frac{cm^2}{g} \times 1.85\frac{g}{cm^3} \times 0.25\ cm)} = 0.157$$

To be conservative, T was taken as its measured value of 0.9 rather than the calculated value above. The fraction of x-rays absorbed (A) by the sample is given as (1-T). Thus, A = 0.1. The dose rate, $\dot{D}$, can be calculated from (**Equation 7**):

$$\dot{D} = \frac{AE_p a}{m} \text{ [Gy/s]} \quad (7)$$

where m is the mass of the bone absorbing radiation, taken to be 10 mg.

Thus, given a uniform distribution of the absorption of x-rays within the bone sample, the total exposure time for each desired dose rate was calculated from the dose rate (Ḋ).

Table 4.1 – Exposure time used to achieve desired dose from x-ray beamline.

Desired Dose (Gy)	Time in Beam (sec)
50	3.8
1,000	75 (1 min, 15 sec)
17,000	1280 (21 min, 20 sec)
35,000	2636 (44 min)

Isolation of collagen protein from bone

The third lumbar vertebra (L3) specimens were demineralized over 3-weeks in 0.5M ethylenediaminetetraacetic acid (EDTA) with the solution changed every 2-3 days. Demineralized specimens were defatted for 24-hours in a 1:1 solution of chloroform and methanol and then soaked in 100% methanol for another hour. Specimens were then dried in a desiccator overnight. Dried specimens were flash-frozen with liquid-nitrogen and crushed into bone powder using a mortar and pestle. Bone powder was then lyophilized (Sequence: -38°C for 180 min, -38°C at 120 mTorr for 90 min, -20°C at 770 mTorr for 900 min, -10°C at 930 mTorr for 270 min, and 23°C at 120 mTorr for 55 min) (VirTis AdVantage Plus Benchtop Freeze Dryer XL Model, SP Scientific, Stone Ridge, NY). For tissue digestion, the powder was added to a solution of 0.5M acetic acid and pepsin (1mg of pepsin per 10 mg of bone powder) and placed on a rocker at 4°C for 72-hours. To neutralize the digestion process 5M NaOH was added until pH was neutral (pH = 6-8). To remove non-soluble collagen and non-collagenous proteins, samples were centrifuged for 30-minutes at 13,000 RPM. The supernatant, containing the soluble collagen, was collected. To precipitate the collagen out of solution, solid NaCl was added to a final concentration of 2M NaCl and placed on a rocker at 4°C for 24-hours. Samples were centrifuged for 30-minutes at 13,000 RPM. The supernatant was removed and the pellets were resuspended in 200 uL of 0.5M acetic acid. Samples were then lyophilized and stored at -20°C until electrophoresis with the bioanalyzer.

Chapter 5 – Conclusions

The goal of this research was to characterize the cyclic and monotonic mechanical properties after radiation exposure at spaceflight- and clinically-relevant doses, and to better understand the factors (both cellular and non-cellular) influencing the resulting mechanical behavior. We have conducted three studies that contribute to this overall goal which are outlined below by recapping the purpose of the study, highlighting major findings, and how these results are important to the field.

First, we presented a new method for precise fatigue testing of mouse vertebral bodies. To recap, cyclic loading experiments are particularly challenging in small animals, such as rats and mice, to perform in a precise manner. We found that by implementing some key steps (i.e. rigorous specimen preparation, adjustable platens, and micro-CT-based finite element analysis to calculate specimen-specific cyclic forces) could reduce the standard deviation of the measured fatigue life up to 5-times, compared to other commonly used procedures from literature. The method is quite a time intensive process. However, the extra effort improves the ability to detect small differences across treatment groups without using a large number of animals. Our new method should improve the ability of future studies to assess mechanically relevant aspects of bone quality associated with aging, disease, or treatment, and thus be impactful to the field.

Second, we presented our findings on the short-term and long-term effects of *in vivo* ionizing radiation exposure at spaceflight (1 Gy) and clinically-relevant (5 Gy) doses. We found that deficits in cancellous microarchitecture after irradiation and aging led to reduced fatigue life in the long-term, 12-weeks after radiation exposure. In contrast, deficits in bone quantity (i.e. reduced bone volume fraction) and collagen structure (i.e. increased collagen crosslinks) did not have a significant impact on monotonic or cyclic mechanics. Our findings suggest that to retain nominal mechanical behavior, maintaining the microarchitecture of bone should be a priority, especially when considering current and future countermeasures for spaceflight and radiotherapy applications. For spaceflight, a countermeasure capable of protecting the architecture, either via anti-resorptive drug (Willey et al. 2010) or diet (Schreurs et al. 2016), is highly encouraged for astronaut bone health. Similarly, for clinical applications, protecting the bone from radiation-induced microarchitecture degradation will likely reduce the risk of fractures observed following radiation therapy.

Lastly, we presented our findings on the effects of *ex vivo* irradiation at clinically-relevant doses ranging from radiotherapy (50 Gy) up to sterilization (35,000 Gy) for the purposes of differentiating between cellular and non-cellular effects and identifying the impact of structural changes to the collagen network on mechanical properties. We found increased collagen fragmentation at 17,000 and above, which coincided with a loss in monotonic and cyclic mechanical properties. In contrast, collagen crosslinks were elevated with all radiation doses, however this did not coincide with a reduction in strength or any other mechanical property. We conclude that mechanical properties of *ex vivo* irradiation are dominated by the direct effects of radiation exposure through fragmentation of the collagen backbone, and are negligibly influenced by the indirect effects of non-enzymatic crosslinks. The primary implications of these results are applicable mostly to sterilization treatment of allografts. Our findings suggest that to maintain mechanical integrity following radiation exposure, bone allograft specimens should be sterilized at a dose below 17,000 Gy. It also suggests that a

radioprotectant capable of decreasing fragmentation, or stabilizing the collagen backbone, could retain mechanical behavior.

These findings have generated new questions to explore as areas of future work. First, we would like to have a better understanding of the specific microarchitecture parameters parameter (e.g. trabecular number, connectivity density, thickness, spacing, or cortical thickness) primarily responsible for the mechanical behavior changes we observed. Computational analysis via micro-CT-based finite element models will be a valuable tool to provide further insight. For example, FEA could be conducted on the specimens from the *in vivo* irradiation study to identify localized regions of high stress or high strain (**Figure 5.1**), and visually or statistically identify if a particular microarchitecture parameter, best explains the resulting decrease in fatigue life observed from our experimental testing. These findings would give us a more in-depth understanding of the important factors in microarchitecture that effect bone mechanical properties and influence risk of fracture.

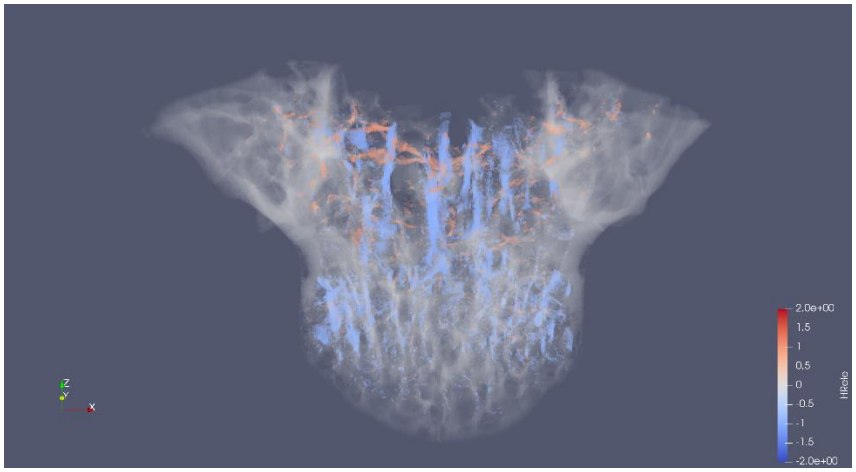

Figure 5.1 – Representative 3D micro-CT image of mouse vertebral body from *in vivo* irradiation experiment (Chapter 3). Finite element model (further details of FEM procedures used in our lab provided in section 2.5 Supplemental Materials) results indicate areas of high risk trabecular tissue calculated based on compressive (blue) and tensile (red) principal stresses. Note the vertical trabeculae are primarily in compression and horizontal trabeculae are primarily in tension. Specimen shown is a control specimen (0 Gy, 11-day). Comparison of results from irradiated and control tissue may give insight into the microarchitectural changes that primarily influence areas of high stress or strain. (Preliminary results conducted and provided by Tongge Wu.)

Related to spaceflight, additional future work recommended includes animal experiments to verify bone material quality and nominal mechanical properties with more "space-like" radiation exposure and current/proposed countermeasures, which include high-LET radiation and bisphosphonate treatment. High-LET radiation (e.g. high-energy nuclei), is known to cause increased radiolysis of water molecules which could lead to higher levels of collagen crosslinks. Bisphosphonates, could also lead the build-up of greater amounts of collagen crosslinks because bone resorption is blocked. Using assays outlined in this dissertation (i.e. fatigue testing and crosslink quantification), we could verify this combination of irradiation and drug-treatment does not lead to deficits in material quality and resulting loss of mechanical properties.

Related to clinical radiotherapy, additional future work recommended includes animal experiments to investigate the best bisphosphonate treatment and dose needed to prevent microarchitecture deficits and loss of mechanical properties. Arrington et al. (Arrington et al.

2010; Willey et al. 2010) has already demonstrated that a bisphosphonate treatment can protect the bone strength in a mouse model where a hind-limb was exposed to 20 Gy. We suggest validating this in a larger animal model, using an irradiation protocol commonly used in radiotherapy treatments where the resulting fracture risk is high (Baxter et al. 2005). Additionally, we would support any future work related to microarchitecture repair to replace lost trabecular connections and struts, possibly through drug- or mechanically-induced mechanisms.

In closure, this research highlighted the critical role of bone microarchitecture in maintaining cyclic mechanical behavior with radiation exposure and aging. It provided further knowledge on collagen degradation from both *in vivo* and *ex vivo* irradiation, and the primary mechanisms that lead to deficits in bone biomechanics. To our knowledge, this research was the first to conduct fatigue testing after radiation exposure related to spaceflight and clinical radiotherapy. Finally, through this effort, we have provided the field with a novel and precise methodology for fatigue testing of small animal bone.

References

Acevedo, C., H. Bale, B. Gludovatz, A. Wat, S. Y. Tang, M. Wang, B. Busse, E. A. Zimmermann, E. Schaible, M. R. Allen, D. B. Burr, and R. O. Ritchie. 2015. 'Alendronate treatment alters bone tissues at multiple structural levels in healthy canine cortical bone', *Bone*, 81: 352-63.

Acevedo, C., M. Sylvia, E. Schaible, J. L. Graham, K. L. Stanhope, L. N. Metz, B. Gludovatz, A. V. Schwartz, R. O. Ritchie, T. N. Alliston, P. J. Havel, and A. J. Fields. 2018. 'Contributions of Material Properties and Structure to Increased Bone Fragility for a Given Bone Mass in the UCD-T2DM Rat Model of Type 2 Diabetes', *J Bone Miner Res*.

Adams, Mark F, Harun H Bayraktar, Tony M Keaveny, and Panayiotis Papadopoulos. 2004. "Ultrascalable implicit finite element analyses in solid mechanics with over a half a billion degrees of freedom." In *Supercomputing, 2004. Proceedings of the ACM/IEEE SC2004 Conference*, 34-34. IEEE.

Akkus, O., and R. M. Belaney. 2005. 'Sterilization by gamma radiation impairs the tensile fatigue life of cortical bone by two orders of magnitude', *J Orthop Res*, 23: 1054-8.

Akkus, O., R. M. Belaney, and P. Das. 2005. 'Free radical scavenging alleviates the biomechanical impairment of gamma radiation sterilized bone tissue', *J Orthop Res*, 23: 838-45.

Akkus, O., and C. M. Rimnac. 2001a. 'Cortical bone tissue resists fatigue fracture by deceleration and arrest of microcrack growth', *J Biomech*, 34: 757-64.

———. 2001b. 'Fracture resistance of gamma radiation sterilized cortical bone allografts', *J Orthop Res*, 19: 927-34.

Altman, A. R., C. M. de Bakker, W. J. Tseng, A. Chandra, L. Qin, and X. S. Liu. 2015. 'Enhanced individual trabecular repair and its mechanical implications in parathyroid hormone and alendronate treated rat tibial bone', *J Biomech Eng*, 137.

Alwood, J. S., A. Kumar, L. H. Tran, A. Wang, C. L. Limoli, and R. K. Globus. 2012. 'Low-dose, ionizing radiation and age-related changes in skeletal microarchitecture', *J Aging Res*, 2012: 481983.

Alwood, J. S., K. Yumoto, R. Mojarrab, C. L. Limoli, E. A. Almeida, N. D. Searby, and R. K. Globus. 2010. 'Heavy ion irradiation and unloading effects on mouse lumbar vertebral microarchitecture, mechanical properties and tissue stresses', *Bone*, 47: 248-55.

Alwood, Joshua S, Luan H Tran, Ann-Sofie Schreurs, Yasaman Shirazi-Fard, Akhilesh Kumar, Diane Hilton, Candice GT Tahimic, and Ruth K Globus. 2017. 'Dose-and Ion-Dependent Effects in the Oxidative Stress Response to Space-Like Radiation Exposure in the Skeletal System', *International journal of molecular sciences*, 18: 2117.

Arrington, S. A., E. R. Fisher, G. E. Willick, K. A. Mann, and M. J. Allen. 2010. 'Anabolic and antiresorptive drugs improve trabecular microarchitecture and reduce fracture risk following radiation therapy', *Calcif Tissue Int*, 87: 263-72.

Bailey, A. J., D. N. Rhodes, and C. W. Cater. 1964. 'Irradiation-Induced Crosslinking of Collagen', *Radiat Res*, 22: 606-21.

Baker, D. A., A. Bellare, and L. Pruitt. 2003. 'The effects of degree of crosslinking on the fatigue crack initiation and propagation resistance of orthopedic-grade polyethylene', *J Biomed Mater Res A*, 66: 146-54.

Bandstra, E. R., M. J. Pecaut, E. R. Anderson, J. S. Willey, F. De Carlo, S. R. Stock, D. S. Gridley, G. A. Nelson, H. G. Levine, and T. A. Bateman. 2008. 'Long-term dose response of trabecular bone in mice to proton radiation', *Radiat Res*, 169: 607-14.

Bandstra, E. R., R. W. Thompson, G. A. Nelson, J. S. Willey, S. Judex, M. A. Cairns, E. R. Benton, M. E. Vazquez, J. A. Carson, and T. A. Bateman. 2009. 'Musculoskeletal changes in mice from 20-50 cGy of simulated galactic cosmic rays', *Radiat Res*, 172: 21-9.

Bartel, Donald L., Dwight T. Davy, and Tony M. Keaveny. 2006. *Orthopaedic biomechanics : mechanics and design in musculoskeletal systems* (Pearson/Prentice Hall: Upper Saddle River, N.J.).

Barth, H. D., M. E. Launey, A. A. Macdowell, J. W. Ager, 3rd, and R. O. Ritchie. 2010. 'On the effect of X-ray irradiation on the deformation and fracture behavior of human cortical bone', *Bone*, 46: 1475-85.

Barth, H. D., E. A. Zimmermann, E. Schaible, S. Y. Tang, T. Alliston, and R. O. Ritchie. 2011. 'Characterization of the effects of x-ray irradiation on the hierarchical structure and mechanical properties of human cortical bone', *Biomaterials*, 32: 8892-904.

Baxter, N. N., E. B. Habermann, J. E. Tepper, S. B. Durham, and B. A. Virnig. 2005. 'Risk of pelvic fractures in older women following pelvic irradiation', *JAMA*, 294: 2587-93.

Bazire, L., H. Xu, J. P. Foy, M. Amessis, C. Malhaire, K. Cao, A. De La Rochefordiere, and Y. M. Kirova. 2017. 'Pelvic insufficiency fracture (PIF) incidence in patients treated with intensity-modulated radiation therapy (IMRT) for gynaecological or anal cancer: single-institution experience and review of the literature', *Br J Radiol*, 90: 20160885.

Benhamou, C. L. 2007. 'Effects of osteoporosis medications on bone quality', *Joint Bone Spine*, 74: 39-47.

Bentler, S. E., L. Liu, M. Obrizan, E. A. Cook, K. B. Wright, J. F. Geweke, E. A. Chrischilles, C. E. Pavlik, R. B. Wallace, R. L. Ohsfeldt, M. P. Jones, G. E. Rosenthal, and F. D. Wolinsky. 2009. 'The aftermath of hip fracture: discharge placement, functional status change, and mortality', *Am J Epidemiol*, 170: 1290-9.

Bevill, G., and T. M. Keaveny. 2009. 'Trabecular bone strength predictions using finite element analysis of micro-scale images at limited spatial resolution', *Bone*, 44: 579-84.

Bouxsein, M. L. 2003a. 'Bone quality: where do we go from here?', *Osteoporos Int*, 14 Suppl 5: S118-27.

———. 2003b. 'Mechanisms of osteoporosis therapy: a bone strength perspective', *Clin Cornerstone*, Suppl 2: S13-21.

Bowman, S. M., X. E. Guo, D. W. Cheng, T. M. Keaveny, L. J. Gibson, W. C. Hayes, and T. A. McMahon. 1998. 'Creep contributes to the fatigue behavior of bovine trabecular bone', *J Biomech Eng*, 120: 647-54.

Brauer, C. A., M. Coca-Perraillon, D. M. Cutler, and A. B. Rosen. 2009. 'Incidence and mortality of hip fractures in the United States', *JAMA*, 302: 1573-9.

Brouwers, J. E., M. Ruchelsman, Bv Rietbergen, and M. L. Bouxsein. 2009. 'Determination of rat vertebral bone compressive fatigue properties in untreated intact rats and zoledronic-acid-treated, ovariectomized rats', *Osteoporos Int*, 20: 1377-84.

Burr, David B., and M. R. Allen. 2013. *Basic and applied bone biology* (Elsevier/Academic Press: Amsterdam).

Burstein, A. H., J. M. Zika, K. G. Heiple, and L. Klein. 1975. 'Contribution of collagen and mineral to the elastic-plastic properties of bone', *J Bone Joint Surg Am*, 57: 956-61.

Burton, B., A. Gaspar, D. Josey, J. Tupy, M. D. Grynpas, and T. L. Willett. 2014. 'Bone embrittlement and collagen modifications due to high-dose gamma-irradiation sterilization', *Bone*, 61: 71-81.

Caler, W. E., and D. R. Carter. 1989. 'Bone creep-fatigue damage accumulation', *J Biomech*, 22: 625-35.

Campbell, D. G., P. Li, A. J. Stephenson, and R. D. Oakeshott. 1994. 'Sterilization of HIV by gamma irradiation. A bone allograft model', *Int Orthop*, 18: 172-6.

Chancellor, Jeffery C, Rebecca S Blue, Keith A Cengel, Serena M Auñón-Chancellor, Kathleen H Rubins, Helmut G Katzgraber, and Ann R Kennedy. 2018. 'Limitations in predicting the space radiation health risk for exploration astronauts', *npj Microgravity*, 4: 8.

Colwell, A., A. Hamer, A. Blumsohn, and R. Eastell. 1996. 'To determine the effects of ultraviolet light, natural light and ionizing radiation on pyridinium cross-links in bone and urine using high-performance liquid chromatography', *Eur J Clin Invest*, 26: 1107-14.

Cornu, O., X. Banse, P. L. Docquier, S. Luyckx, and C. Delloye. 2000. 'Effect of freeze-drying and gamma irradiation on the mechanical properties of human cancellous bone', *J Orthop Res*, 18: 426-31.

Cucinotta, F. A., and M. Durante. 2006. 'Cancer risk from exposure to galactic cosmic rays: implications for space exploration by human beings', *Lancet Oncol*, 7: 431-5.

Currey, J. D., J. Foreman, I. Laketic, J. Mitchell, D. E. Pegg, and G. C. Reilly. 1997. 'Effects of ionizing radiation on the mechanical properties of human bone', *J Orthop Res*, 15: 111-7.

Farlay, D., L. A. Armas, E. Gineyts, M. P. Akhter, R. R. Recker, and G. Boivin. 2016. 'Nonenzymatic Glycation and Degree of Mineralization Are Higher in Bone From Fractured Patients With Type 1 Diabetes Mellitus', *J Bone Miner Res*, 31: 190-5.

Farr, J. N., and S. Khosla. 2016. 'Determinants of bone strength and quality in diabetes mellitus in humans', *Bone*, 82: 28-34.

Fields, A. J., and T. M. Keaveny. 2012. 'Trabecular architecture and vertebral fragility in osteoporosis', *Curr Osteoporos Rep*, 10: 132-40.

Follet, H., S. Viguet-Carrin, B. Burt-Pichat, B. Depalle, Y. Bala, E. Gineyts, F. Munoz, M. Arlot, G. Boivin, R. D. Chapurlat, P. D. Delmas, and M. L. Bouxsein. 2011. 'Effects of preexisting microdamage, collagen cross-links, degree of mineralization, age, and architecture on compressive mechanical properties of elderly human vertebral trabecular bone', *J Orthop Res*, 29: 481-8.

Fyhrie, D. P., and B. A. Christiansen. 2015. 'Bone Material Properties and Skeletal Fragility', *Calcif Tissue Int*, 97: 213-28.

Glatt, V., E. Canalis, L. Stadmeyer, and M. L. Bouxsein. 2007. 'Age-related changes in trabecular architecture differ in female and male C57BL/6J mice', *J Bone Miner Res*, 22: 1197-207.

Goh, S. K., K. Y. Yang, J. S. Koh, M. K. Wong, S. Y. Chua, D. T. Chua, and T. S. Howe. 2007. 'Subtrochanteric insufficiency fractures in patients on alendronate therapy: a caution', *J Bone Joint Surg Br*, 89: 349-53.

Gong, Bo, Megan E Oest, Kenneth A Mann, Timothy A Damron, and Michael D Morris. 2013. 'Raman spectroscopy demonstrates prolonged alteration of bone chemical composition following extremity localized irradiation', *Bone*, 57: 252-58.

Granke, M., M. D. Does, and J. S. Nyman. 2015. 'The Role of Water Compartments in the Material Properties of Cortical Bone', *Calcif Tissue Int*, 97: 292-307.

Green, Danielle E, Benjamin J Adler, Meilin E Chan, and Clinton T Rubin. 2012. 'Devastation of adult stem cell pools by irradiation precedes collapse of trabecular bone quality and quantity', *Journal of Bone and Mineral Research*, 27: 749-59.

Green, Danielle E, Benjamin J Adler, Meilin Ete Chan, James J Lennon, Alvin S Acerbo, Lisa M Miller, and Clinton T Rubin. 2013. 'Altered composition of bone as triggered by irradiation facilitates the rapid erosion of the matrix by both cellular and physicochemical processes', *PLoS One*, 8: e64952.

Guo, X. E., and C. H. Kim. 2002. 'Mechanical consequence of trabecular bone loss and its treatment: a three-dimensional model simulation', *Bone*, 30: 404-11.

Haddock, S. M., O. C. Yeh, P. V. Mummaneni, W. S. Rosenberg, and T. M. Keaveny. 2004. 'Similarity in the fatigue behavior of trabecular bone across site and species', *J Biomech*, 37: 181-7.

Halloran, B. P., V. L. Ferguson, S. J. Simske, A. Burghardt, L. L. Venton, and S. Majumdar. 2002. 'Changes in bone structure and mass with advancing age in the male C57BL/6J mouse', *J Bone Miner Res*, 17: 1044-50.

Hamer, A. J., J. R. Strachan, M. M. Black, C. J. Ibbotson, I. Stockley, and R. A. Elson. 1996. 'Biochemical properties of cortical allograft bone using a new method of bone strength measurement. A comparison of fresh, fresh-frozen and irradiated bone', *J Bone Joint Surg Br*, 78: 363-8.

Hamilton, S. A., M. J. Pecaut, D. S. Gridley, N. D. Travis, E. R. Bandstra, J. S. Willey, G. A. Nelson, and T. A. Bateman. 2006. 'A murine model for bone loss from therapeutic and space-relevant sources of radiation', *J Appl Physiol (1985)*, 101: 789-93.

Hernandez, C. J., and T. M. Keaveny. 2006. 'A biomechanical perspective on bone quality', *Bone*, 39: 1173-81.

Ireland, A., T. Maden-Wilkinson, J. McPhee, K. Cooke, M. Narici, H. Degens, and J. Rittweger. 2013. 'Upper limb muscle-bone asymmetries and bone adaptation in elite youth tennis players', *Med Sci Sports Exerc*, 45: 1749-58.

Janghorbani, M., R. M. Van Dam, W. C. Willett, and F. B. Hu. 2007. 'Systematic review of type 1 and type 2 diabetes mellitus and risk of fracture', *Am J Epidemiol*, 166: 495-505.

Karim, L., and M. L. Bouxsein. 2016. 'Effect of type 2 diabetes-related non-enzymatic glycation on bone biomechanical properties', *Bone*, 82: 21-7.

Keaveny, T. M., R. E. Borchers, L. J. Gibson, and W. C. Hayes. 1993. 'Theoretical analysis of the experimental artifact in trabecular bone compressive modulus', *J Biomech*, 26: 599-607.

Keaveny, T. M., X. E. Guo, E. F. Wachtel, T. A. McMahon, and W. C. Hayes. 1994. 'Trabecular bone exhibits fully linear elastic behavior and yields at low strains', *J Biomech*, 27: 1127-36.

Keaveny, T. M., E. F. Morgan, G. L. Niebur, and O. C. Yeh. 2001. 'Biomechanics of trabecular bone', *Annu Rev Biomed Eng*, 3: 307-33.

Keaveny, T. M., T. P. Pinilla, R. P. Crawford, D. L. Kopperdahl, and A. Lou. 1997. 'Systematic and random errors in compression testing of trabecular bone', *J Orthop Res*, 15: 101-10.

Keaveny, T. M., E. F. Wachtel, C. M. Ford, and W. C. Hayes. 1994. 'Differences between the tensile and compressive strengths of bovine tibial trabecular bone depend on modulus', *J Biomech*, 27: 1137-46.

Keaveny, T. M., E. F. Wachtel, X. E. Guo, and W. C. Hayes. 1994. 'Mechanical behavior of damaged trabecular bone', *J Biomech*, 27: 1309-18.

Knott, L., and A. J. Bailey. 1998. 'Collagen cross-links in mineralizing tissues: a review of their chemistry, function, and clinical relevance', *Bone*, 22: 181-7.

Kondo, H., N. D. Searby, R. Mojarrab, J. Phillips, J. Alwood, K. Yumoto, E. A. Almeida, C. L. Limoli, and R. K. Globus. 2009. 'Total-body irradiation of postpubertal mice with (137)Cs acutely compromises the microarchitecture of cancellous bone and increases osteoclasts', *Radiat Res*, 171: 283-9.

Kruzic, J. J., and R. O. Ritchie. 2008. 'Fatigue of mineralized tissues: cortical bone and dentin', *J Mech Behav Biomed Mater*, 1: 3-17.

Lafferty, J. F. 1978. 'Analytical model of the fatigue characteristics of bone', *Aviat Space Environ Med*, 49: 170-4.

Lambers, F. M., A. R. Bouman, C. M. Rimnac, and C. J. Hernandez. 2013. 'Microdamage caused by fatigue loading in human cancellous bone: relationship to reductions in bone biomechanical performance', *PLoS One*, 8: e83662.

Lang, T., A. LeBlanc, H. Evans, Y. Lu, H. Genant, and A. Yu. 2004. 'Cortical and trabecular bone mineral loss from the spine and hip in long-duration spaceflight', *J Bone Miner Res*, 19: 1006-12.

LeBlanc, A. D., E. R. Spector, H. J. Evans, and J. D. Sibonga. 2007. 'Skeletal responses to space flight and the bed rest analog: a review', *J Musculoskelet Neuronal Interact*, 7: 33-47.

Leblanc, A., T. Matsumoto, J. Jones, J. Shapiro, T. Lang, L. Shackelford, S. M. Smith, H. Evans, E. Spector, R. Ploutz-Snyder, J. Sibonga, J. Keyak, T. Nakamura, K. Kohri, and H. Ohshima. 2013. 'Bisphosphonates as a supplement to exercise to protect bone during long-duration spaceflight', *Osteoporos Int*, 24: 2105-14.

LeBlanc, A., V. Schneider, L. Shackelford, S. West, V. Oganov, A. Bakulin, and L. Voronin. 2000. 'Bone mineral and lean tissue loss after long duration space flight', *J Musculoskelet Neuronal Interact*, 1: 157-60.

Lenart, B. A., D. G. Lorich, and J. M. Lane. 2008. 'Atypical fractures of the femoral diaphysis in postmenopausal women taking alendronate', *N Engl J Med*, 358: 1304-6.

Lietman, S. A., W. W. Tomford, M. C. Gebhardt, D. S. Springfield, and H. J. Mankin. 2000. 'Complications of irradiated allografts in orthopaedic tumor surgery', *Clin Orthop Relat Res*: 214-7.

McClung, M. R., J. San Martin, P. D. Miller, R. Civitelli, F. Bandeira, M. Omizo, D. W. Donley, G. P. Dalsky, and E. F. Eriksen. 2005. 'Opposite bone remodeling effects of teriparatide and alendronate in increasing bone mass', *Arch Intern Med*, 165: 1762-8.

McCubbrey, D. A., D. D. Cody, E. L. Peterson, J. L. Kuhn, M. J. Flynn, and S. A. Goldstein. 1995. 'Static and fatigue failure properties of thoracic and lumbar vertebral bodies and their relation to regional density', *J Biomech*, 28: 891-9.

Melton, L. J., 3rd, B. L. Riggs, C. L. Leibson, S. J. Achenbach, J. J. Camp, M. L. Bouxsein, E. J. Atkinson, R. A. Robb, and S. Khosla. 2008. 'A bone structural basis for fracture risk in diabetes', *J Clin Endocrinol Metab*, 93: 4804-9.

Miller, K. D., R. L. Siegel, C. C. Lin, A. B. Mariotto, J. L. Kramer, J. H. Rowland, K. D. Stein, R. Alteri, and A. Jemal. 2016. 'Cancer treatment and survivorship statistics, 2016', *CA Cancer J Clin*, 66: 271-89.

Mosekilde, L. 1995. 'Assessing bone quality--animal models in preclinical osteoporosis research', *Bone*, 17: 343S-52S.

Nalla, R. K., J. H. Kinney, and R. O. Ritchie. 2003. 'Mechanistic fracture criteria for the failure of human cortical bone', *Nat Mater*, 2: 164-8.

National Council on Radiation Protection and Measurements. 2014. "Radiation protection for space activities : supplement to previous recommendations." In *NCRP commentary no 23*, 1 online resource. Bethesda, Maryland: National Council on Radiation Protection and Measurements,.

National Council on Radiation Protection and Measurements. 2000. *Radiation protection guidance for activities in low-earth orbit* (National Council on Radiation Protection and Measurements: Bethesda, MD).

Nguyen, H., D. A. Morgan, and M. R. Forwood. 2007. 'Sterilization of allograft bone: effects of gamma irradiation on allograft biology and biomechanics', *Cell Tissue Bank*, 8: 93-105.

———. 2011. 'Validation of 11 kGy as a radiation sterilization dose for frozen bone allografts', *J Arthroplasty*, 26: 303-8.

Nyman, J. S., M. Reyes, and X. Wang. 2005. 'Effect of ultrastructural changes on the toughness of bone', *Micron*, 36: 566-82.

Odgaard, A., I. Hvid, and F. Linde. 1989. 'Compressive axial strain distributions in cancellous bone specimens', *J Biomech*, 22: 829-35.

Odgaard, A., and F. Linde. 1991. 'The underestimation of Young's modulus in compressive testing of cancellous bone specimens', *J Biomech*, 24: 691-8.

Odvina, C. V., J. E. Zerwekh, D. S. Rao, N. Maalouf, F. A. Gottschalk, and C. Y. Pak. 2005. 'Severely suppressed bone turnover: a potential complication of alendronate therapy', *J Clin Endocrinol Metab*, 90: 1294-301.

Oest, M. E., C. G. Policastro, K. A. Mann, N. D. Zimmerman, and T. A. Damron. 2018. 'Longitudinal Effects of Single Hindlimb Radiation Therapy on Bone Strength and Morphology at Local and Contralateral Sites', *J Bone Miner Res*, 33: 99-112.

Oest, Megan E, and Timothy A Damron. 2014. 'Focal therapeutic irradiation induces an early transient increase in bone glycation', *Radiation research*, 181: 439-43.

Oest, Megan E, Veerle Franken, Timothy Kuchera, Judy Strauss, and Timothy A Damron. 2015. 'Long-term loss of osteoclasts and unopposed cortical mineral apposition following limited field irradiation', *Journal of Orthopaedic Research*, 33: 334-42.

Oest, Megan E, Bo Gong, Karen Esmonde-White, Kenneth A Mann, Nicholas D Zimmerman, Timothy A Damron, and Michael D Morris. 2016. 'Parathyroid hormone attenuates radiation-induced increases in collagen crosslink ratio at periosteal surfaces of mouse tibia', *Bone*, 86: 91-97.

Okoukoni, C., D. M. Randolph, E. R. McTyre, A. Kwok, A. A. Weaver, A. W. Blackstock, M. T. Munley, and J. S. Willey. 2017. 'Early dose-dependent cortical thinning of the femoral neck in anal cancer patients treated with pelvic radiation therapy', *Bone*, 94: 84-89.

Ominsky, M. S., B. Stouch, J. Schroeder, I. Pyrah, M. Stolina, S. Y. Smith, and P. J. Kostenuik. 2011. 'Denosumab, a fully human RANKL antibody, reduced bone turnover markers and increased trabecular and cortical bone mass, density, and strength in ovariectomized cynomolgus monkeys', *Bone*, 49: 162-73.

Overgaard, M. 1988. 'Spontaneous radiation-induced rib fractures in breast cancer patients treated with postmastectomy irradiation. A clinical radiobiological analysis of the influence of fraction size and dose-response relationships on late bone damage', *Acta Oncol*, 27: 117-22.

Patsch, J. M., A. J. Burghardt, S. P. Yap, T. Baum, A. V. Schwartz, G. B. Joseph, and T. M. Link. 2013. 'Increased cortical porosity in type 2 diabetic postmenopausal women with fragility fractures', *J Bone Miner Res*, 28: 313-24.

Riggs, B. L., S. F. Hodgson, W. M. O'Fallon, E. Y. Chao, H. W. Wahner, J. M. Muhs, S. L. Cedel, and L. J. Melton, 3rd. 1990. 'Effect of fluoride treatment on the fracture rate in postmenopausal women with osteoporosis', *N Engl J Med*, 322: 802-9.

Riggs, B. L., and L. J. Melton, 3rd. 1986. 'Involutional osteoporosis', *N Engl J Med*, 314: 1676-86.

Roche, J. J., R. T. Wenn, O. Sahota, and C. G. Moran. 2005. 'Effect of comorbidities and postoperative complications on mortality after hip fracture in elderly people: prospective observational cohort study', *BMJ*, 331: 1374.

Rubin, M. R., and J. M. Patsch. 2016. 'Assessment of bone turnover and bone quality in type 2 diabetic bone disease: current concepts and future directions', *Bone Res*, 4: 16001.

Russell, R. G., M. J. Rogers, J. C. Frith, S. P. Luckman, F. P. Coxon, H. L. Benford, P. I. Croucher, C. Shipman, and H. A. Fleisch. 1999. 'The pharmacology of bisphosphonates and new insights into their mechanisms of action', *J Bone Miner Res*, 14 Suppl 2: 53-65.

Saito, M., and K. Marumo. 2010. 'Collagen cross-links as a determinant of bone quality: a possible explanation for bone fragility in aging, osteoporosis, and diabetes mellitus', *Osteoporos Int*, 21: 195-214.

———. 2013. 'Bone quality in diabetes', *Front Endocrinol (Lausanne)*, 4: 72.

———. 2015. 'Effects of Collagen Crosslinking on Bone Material Properties in Health and Disease', *Calcif Tissue Int*, 97: 242-61.

Schileo, E., F. Taddei, L. Cristofolini, and M. Viceconti. 2008. 'Subject-specific finite element models implementing a maximum principal strain criterion are able to estimate failure risk and fracture location on human femurs tested in vitro', *J Biomech*, 41: 356-67.

Schnell, S., S. M. Friedman, D. A. Mendelson, K. W. Bingham, and S. L. Kates. 2010. 'The 1-year mortality of patients treated in a hip fracture program for elders', *Geriatr Orthop Surg Rehabil*, 1: 6-14.

Schreurs, A-S, Y Shirazi-Fard, M Shahnazari, JS Alwood, TA Truong, CGT Tahimic, CL Limoli, ND Turner, B Halloran, and RK Globus. 2016. 'Dried plum diet protects from bone loss caused by ionizing radiation', *Scientific reports*, 6: 21343.

Seeman, E., and P. D. Delmas. 2006. 'Bone quality--the material and structural basis of bone strength and fragility', *N Engl J Med*, 354: 2250-61.

Sell, D. R., and V. M. Monnier. 1989. 'Isolation, purification and partial characterization of novel fluorophores from aging human insoluble collagen-rich tissue', *Connect Tissue Res*, 19: 77-92.

Silva, M. J., and L. J. Gibson. 1997. 'Modeling the mechanical behavior of vertebral trabecular bone: effects of age-related changes in microstructure', *Bone*, 21: 191-9.

Singh, R., D. Singh, and A. Singh. 2016. 'Radiation sterilization of tissue allografts: A review', *World J Radiol*, 8: 355-69.

Sogaard, C. H., L. Mosekilde, A. Richards, and L. Mosekilde. 1994. 'Marked decrease in trabecular bone quality after five years of sodium fluoride therapy--assessed by biomechanical testing of iliac crest bone biopsies in osteoporotic patients', *Bone*, 15: 393-9.

Suresh, S. 1998. *Fatigue of materials* (Cambridge University Press: Cambridge ; New York).

Tang, S. Y., M. R. Allen, R. Phipps, D. B. Burr, and D. Vashishth. 2009. 'Changes in non-enzymatic glycation and its association with altered mechanical properties following 1-year treatment with risedronate or alendronate', *Osteoporos Int*, 20: 887-94.

Tang, S. Y., U. Zeenath, and D. Vashishth. 2007. 'Effects of non-enzymatic glycation on cancellous bone fragility', *Bone*, 40: 1144-51.

Taylor, A. F., M. M. Saunders, D. L. Shingle, J. M. Cimbala, Z. Zhou, and H. J. Donahue. 2007. 'Mechanically stimulated osteocytes regulate osteoblastic activity via gap junctions', *Am J Physiol Cell Physiol*, 292: C545-52.

Tolia, M., A. Zygogianni, J. R. Kouvaris, C. Meristoudis, N. Margari, P. Karakitsos, I. Kokakis, D. Kardamakis, C. Papadimitriou, K. Mystakidou, N. Tsoukalas, G. Kyrgias, B. Armonis, D. K. Filippiadis, A. D. Kelekis, N. Kelekis, and V. Kouloulias. 2014. 'The key role of bisphosphonates in the supportive care of cancer patients', *Anticancer Res*, 34: 23-37.

Turner, C. H., and D. B. Burr. 1993. 'Basic biomechanical measurements of bone: a tutorial', *Bone*, 14: 595-608.

Turner, J. E. 2007. *Atoms, radiation, and radiation protection* (Wiley-VCH: Weinheim).

Turner, Russell T, Urszula T Iwaniec, Carmen P Wong, Laurence B Lindenmaier, Lindsay A Wagner, Adam J Branscum, Scott A Menn, James Taylor, Ye Zhang, and Honglu Wu. 2013. 'Acute exposure to high dose γ-radiation results in transient activation of bone lining cells', *Bone*, 57: 164-73.

Vestergaard, P. 2007. 'Discrepancies in bone mineral density and fracture risk in patients with type 1 and type 2 diabetes--a meta-analysis', *Osteoporos Int*, 18: 427-44.

Wang, X., X. Shen, X. Li, and C. M. Agrawal. 2002. 'Age-related changes in the collagen network and toughness of bone', *Bone*, 31: 1-7.

Watts, N. B. 2002. 'Bone quality: getting closer to a definition', *J Bone Miner Res*, 17: 1148-50.

Wernle, James D, Timothy A Damron, Matthew J Allen, and Kenneth A Mann. 2010. 'Local irradiation alters bone morphology and increases bone fragility in a mouse model', *Journal of biomechanics*, 43: 2738-46.

Willett, T. L., B. Burton, M. Woodside, Z. Wang, A. Gaspar, and T. Attia. 2015. 'gamma-Irradiation sterilized bone strengthened and toughened by ribose pre-treatment', *J Mech Behav Biomed Mater*, 44: 147-55.

Willey, J. S., E. W. Livingston, M. E. Robbins, J. D. Bourland, L. Tirado-Lee, H. Smith-Sielicki, and T. A. Bateman. 2010. 'Risedronate prevents early radiation-induced osteoporosis in mice at multiple skeletal locations', *Bone*, 46: 101-11.

Willey, J. S., S. A. Lloyd, G. A. Nelson, and T. A. Bateman. 2011a. 'Ionizing Radiation and Bone Loss: Space Exploration and Clinical Therapy Applications', *Clin Rev Bone Miner Metab*, 9: 54-62.

———. 2011b. 'Space Radiation and Bone Loss', *Gravit Space Biol Bull*, 25: 14-21.

Wilson, J. W., M. Kim, W. Schimmerling, F. F. Badavi, S. A. Thibeault, F. A. Cucinotta, J. L. Shinn, and R. Kiefer. 1995. 'Issues in space radiation protection: galactic cosmic rays', *Health Phys*, 68: 50-8.

Woodside, M., and T. L. Willett. 2016. 'Elastic-plastic fracture toughness and rising JR-curve behavior of cortical bone is partially protected from irradiation-sterilization-induced degradation by ribose protectant', *J Mech Behav Biomed Mater*, 64: 53-64.

Yamamoto, E., R. Paul Crawford, D. D. Chan, and T. M. Keaveny. 2006. 'Development of residual strains in human vertebral trabecular bone after prolonged static and cyclic loading at low load levels', *J Biomech*, 39: 1812-8.

Zimmermann, E. A., E. Schaible, H. Bale, H. D. Barth, S. Y. Tang, P. Reichert, B. Busse, T. Alliston, J. W. Ager, 3rd, and R. O. Ritchie. 2011. 'Age-related changes in the plasticity and toughness of human cortical bone at multiple length scales', *Proc Natl Acad Sci U S A*, 108: 14416-21.

Zioupos, P., J. D. Currey, and A. J. Hamer. 1999. 'The role of collagen in the declining mechanical properties of aging human cortical bone', *J Biomed Mater Res*, 45: 108-16.

Appendix A – Supplemental Figures & Tables

The following appendix provides additional figures and tables that supplement the research presented in Chapters 2 to 4.

A.1 Additional Figures for Chapter 2

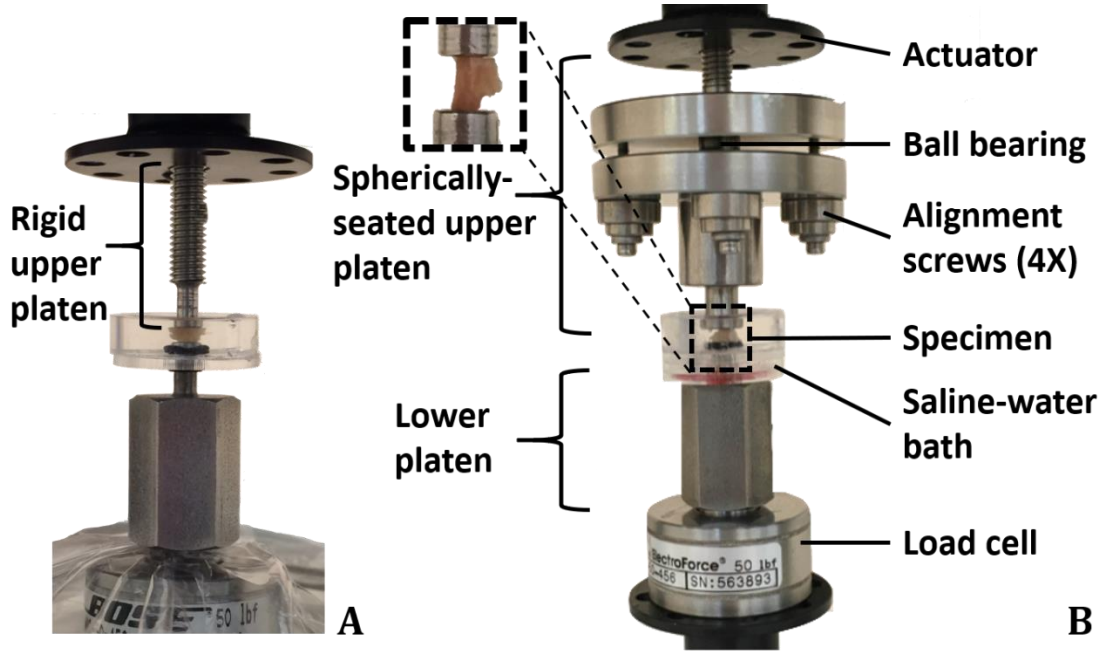

Figure A.6 – Comparison of old and new upper platen designs for mechanical compression testing of mouse vertebral body. (A) Old, rigid upper platen design that was originally used. (B) New, spherically-seated upper platen design that can adjust to mate flush to top surface of specimen ensuring uniform distribution of force applied across surface.

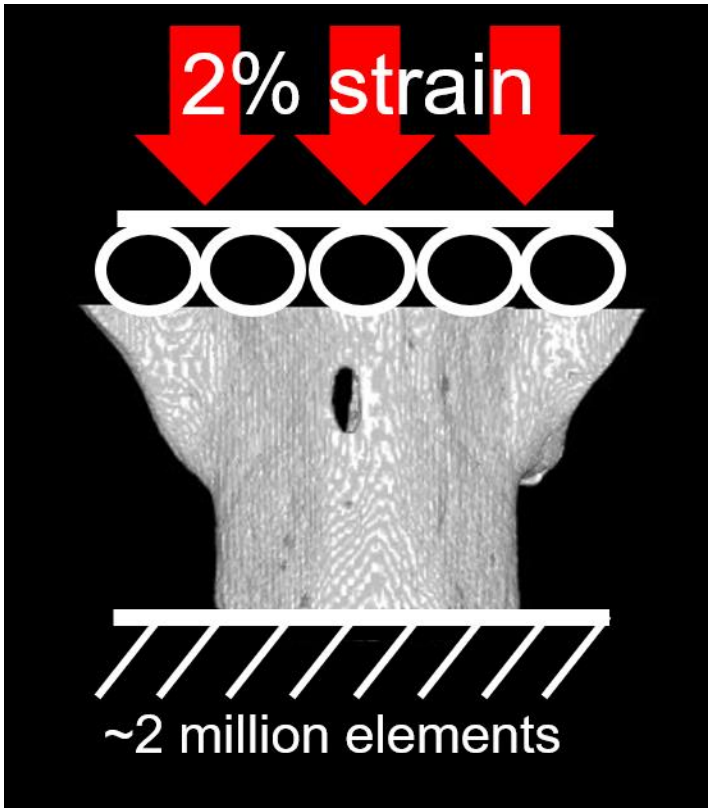

Figure A.7 – Schematic of finite element model with boundary and loading conditions applied.

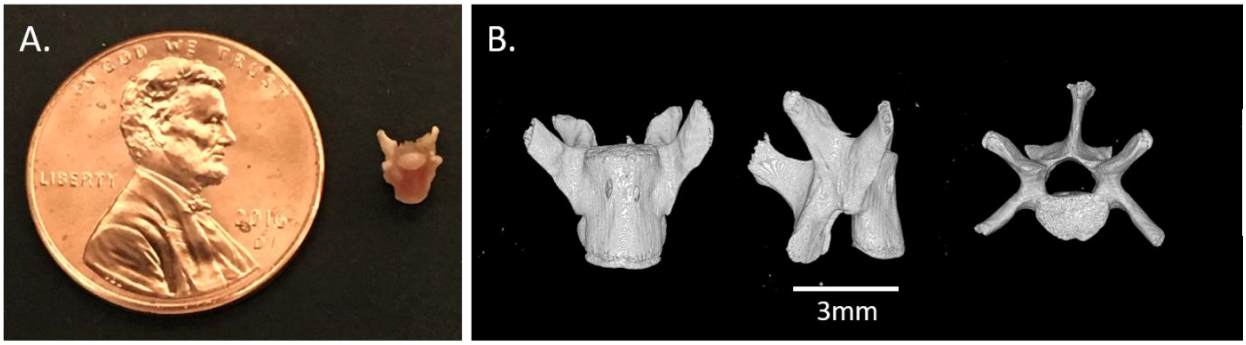

Figure A.8 – Mouse lumbar vertebra (L5) prior to sample preparation. (A) Size comparison of vertebra to a penny. Specimens are ~95% smaller compared to rat vertebrae. (B) Front, right, and top side views of mouse L5.

A.2 Additional Figures for Chapter 3

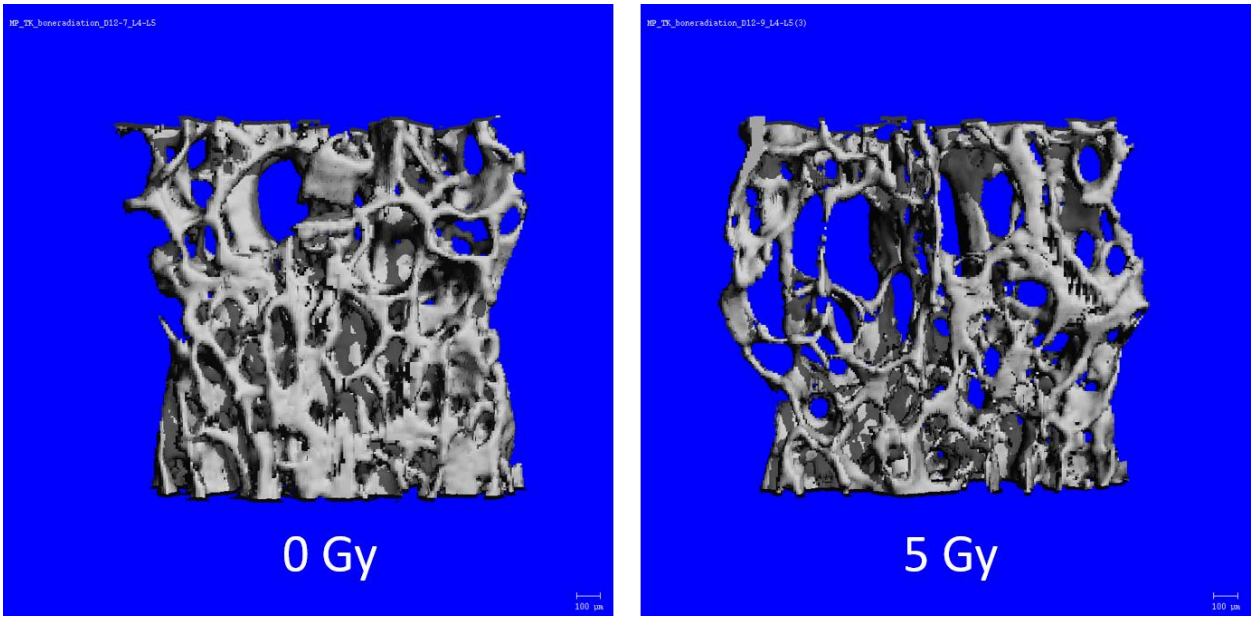

Figure A.9 – Comparison of trabecular compartments from mouse L5 vertebral bodies after 0 Gy (Sham D12.7) and 5 Gy (D12.9) irradiation at 11-days. There was significant loss of bone volume fraction and microarchitecture parameters within 11-days. (Photos courtesy of Alfred Li.)

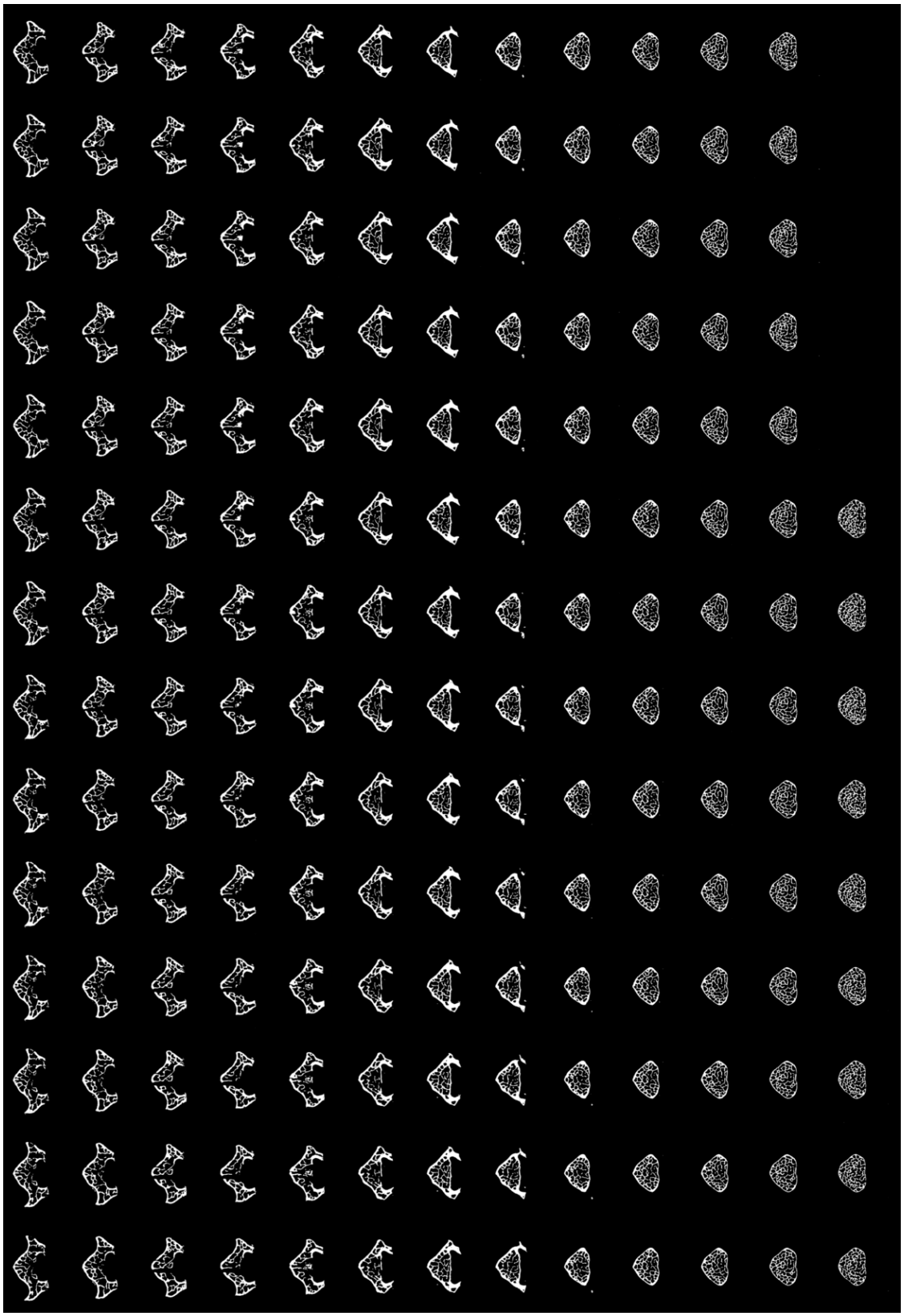

Figure A.10 – Montage generated in ImageJ of micro-CT slices from specimen D12.7 which is from the 0 Gy 11-day group to show the bone quantity and microarchitecture of the control for comparison to the following montage.

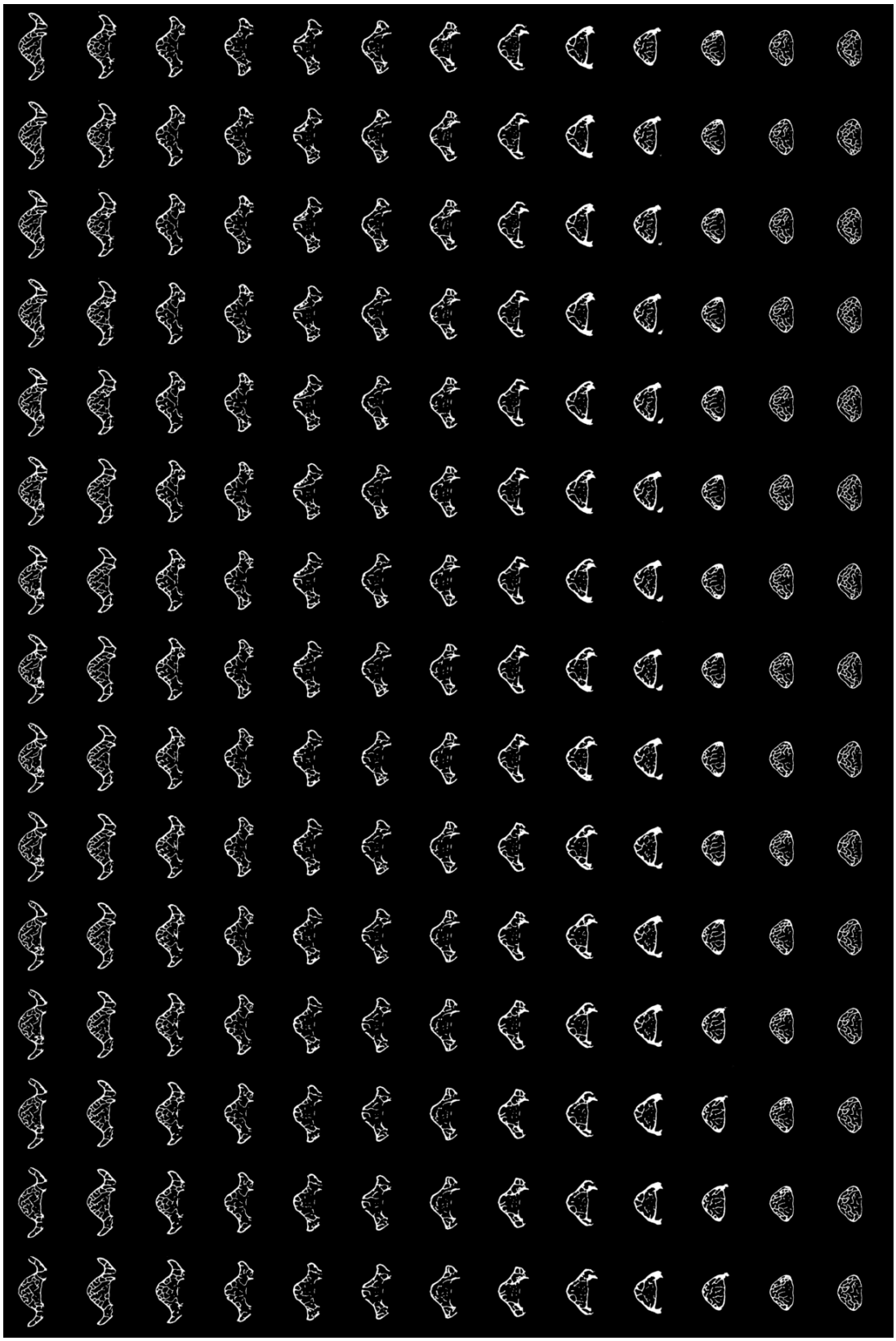

Figure A.11 – Montage generated in ImageJ of micro-CT slices from specimen D12.51 which is from the 5 Gy 12-wk group to show the loss of tissue and microarchitecture.

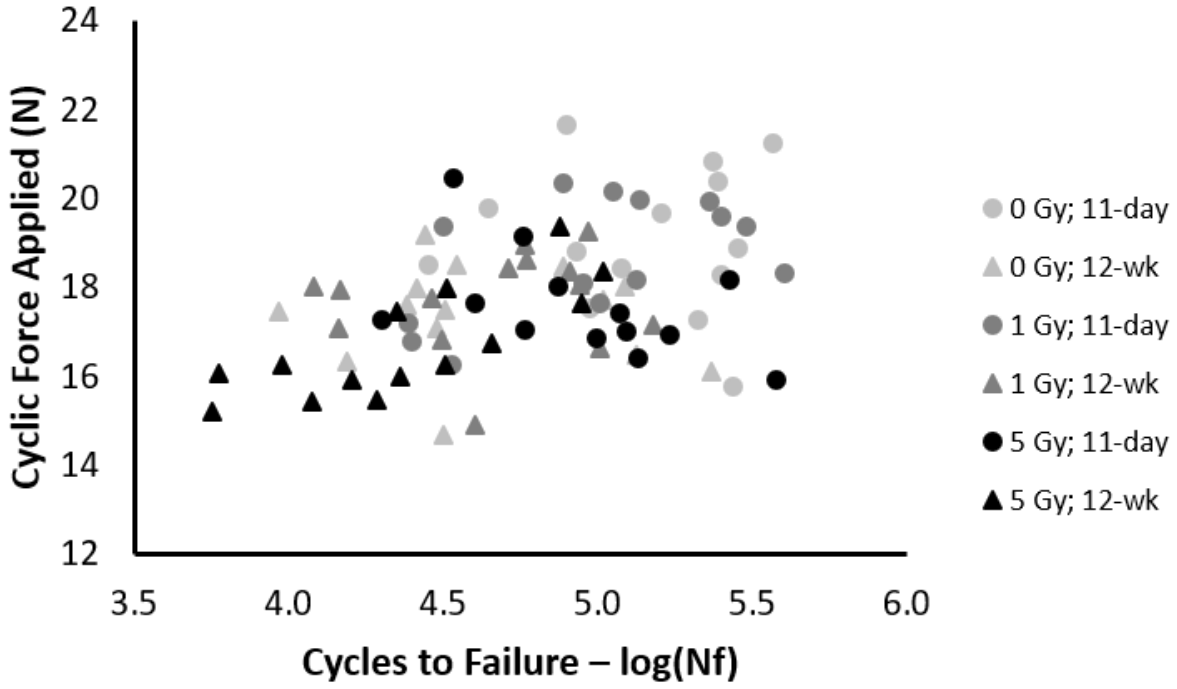

Figure A.12 – S-N "like" plot for all specimens tested in the *in vivo* irradiation study. Instead of stress, the y-axis is the maximum cyclic force applied during fatigue testing versus number of cycles to failure, or fatigue life. Note that the 5 Gy 12-wk specimens have the lowest number of cycles to failure even though they were typically tested at lower forces. The force is prescribed from FEA, and because the specimens had lower BV/TV and degraded microarchitecture the resulting force prescribed was lower.

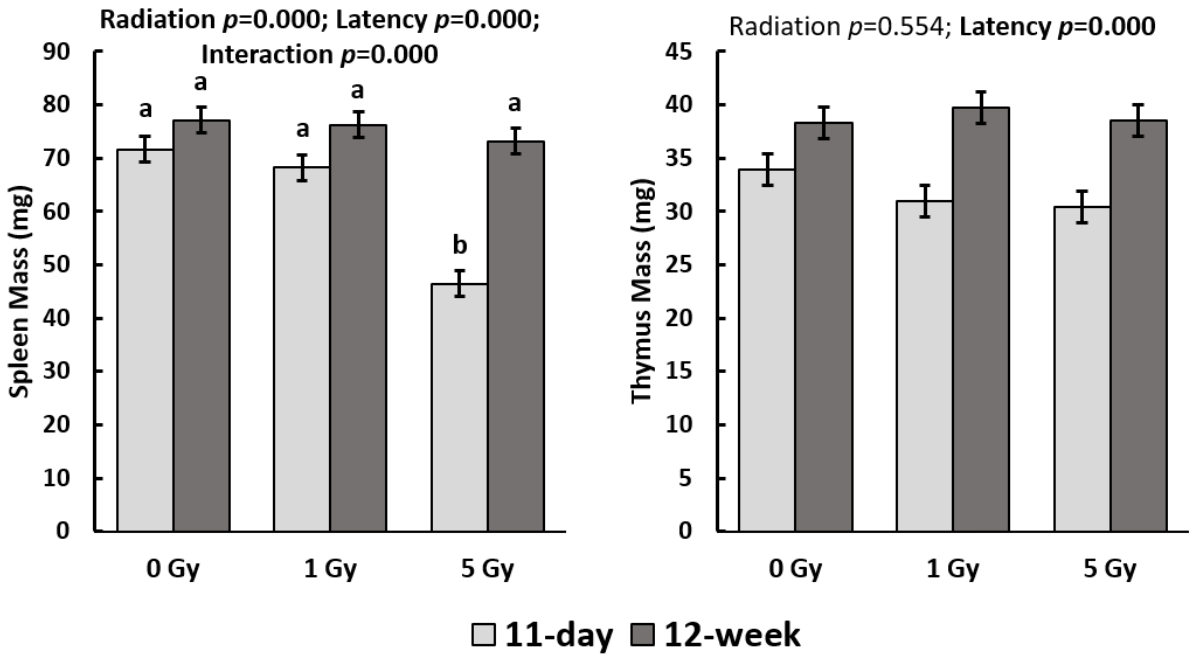

Figure A.13 – Mass of spleen and thymus for mice from *in vivo* irradiation study (Chapter 3). Bars are least squares means with standard error. Bolded terms (latency, radiation, or interaction) were significant ($p < 0.05$). Mass of the spleen and thymus are indications of the animal's overall health and immune response to treatment. For example, a lower spleen mass may indicate poor health of the animal and/or a large immune response of the animal's monocytes, which a large reserve is stored in the spleen. The spleen mass with 5 Gy after-11-days is significantly lower, but recovered by the 12-week timepoint. The thymus mass was higher for all 12-week groups. This is different compared to human, where the thymus decreases in size with age.

Table A.1 – Two-way ANOVA results for key parameters of the *in vivo* irradiation study.

	Radiation						Latency				Interaction (Radiation X Latency)											
Parameter:	0 Gy	1 Gy	% diff.	5 Gy	% diff.	*p*	11-day	12-wk	% diff.	*p*	0 Gy, 11-day	0 Gy, 12-wk	% diff.	1 Gy, 11-day	% diff.	1 Gy, 12-wk	% diff.	5 Gy, 11-day	% diff.	5 Gy, 12-wk	% diff.	*p*
BV/TV (%)	**18.8 a**	**18.3**	**-2.38 a**	**15.6**	**-17.19 b**	**0.00**	17.9	17.20	-4.03	0.07	**19.9 a**	**17.6**	**-11.50 b**	**18.3**	**-7.94 a,b**	**18.3**	**-8.06 a,b**	**15.5**	**-22.32 c**	**15.6**	**-21.58 c**	**0.02**
Tb.Th (mm)	**0.04 a**	**0.04**	**1.33 a**	**0.04**	**6.80 b**	**0.00**	0.04	0.04	-1.05	0.19	0.04 a	0.04	-3.17 a	0.04	-0.55 a	0.04	0.00 a	0.04	5.39 b	0.04	4.81 b	0.16
Tb.Sp (mm)	**0.20 a**	**0.21**	**2.94 a**	**0.24**	**17.13 b**	**0.00**	**0.21 a**	**0.22**	**7.37 b**	**0.00**	0.19 a	0.21	8.04 a,b,c	0.20	5.00 a,b	0.21	9.17 b,c	0.23	16.11 c	0.25	27.57 d	0.27
Tb.N (mm^{-1})	**4.84 a**	**4.72**	**-2.42 a**	**4.21**	**-12.93 b**	**0.00**	**4.79 a**	**4.40**	**-8.17 b**	**0.00**	5.05 a	4.63	-8.49 b,c	4.85	-4.04 a,b	4.60	-9.08 b,c	4.46	-11.78 c	3.97	-21.46 d	0.35
Conn.D ($1/mm^3$)	**235 a**	**221**	**-5.63 a**	**179**	**-23.69 b**	**0.00**	**248 a**	**175**	**-29.52 b**	**0.00**	268 a	201	-25.01 b,c	254	-5.16 a	188	-29.71 c	222	-17.00 b	135	-49.46 d	0.30
SMI	**0.80 a**	**0.84**	**4.52 a**	**1.35**	**67.31 b**	**0.00**	**1.06 a**	**0.93**	**-12.30 b**	**0.00**	**0.75 a**	**0.86**	**15.84 a**	**0.90**	**20.06 a**	**0.79**	**5.55 a**	**1.55**	**107.5 b**	**1.15**	**53.59 b**	**0.00**
CSA (mm^2)	0.64 a	0.63	-2.05 a	0.64	0.86 a	0.13	0.64 a	0.63	-1.18 a	0.32	0.64 a	0.64	-0.35 a	0.63	-1.43 a	0.62	-3.02 a	0.65	1.50 a	0.64	-0.12 a	0.88
Ct.Th (mm)	0.05 a	0.05	-3.17 a	0.05	0.56 a	0.43	**0.05 a**	**0.05**	**-10.50 b**	**0.00**	0.05 a	0.05	-11.05 a,b	0.05	-3.99 a,b	0.05	-13.05 b	0.05	0.52 a	0.05	-10.52 a,b	0.92
Cycles to Failure — $\log(N_f)$	4.88 a	4.81	-1.46 a	4.65	-4.71 a	0.08	**5.02 a**	**4.55**	**-9.41 b**	**0.00**	5.14 a	4.63	-10.03 b,c	4.98	-3.21 a,b	4.65	-9.60 b,c	4.94	-3.92 a,b	4.37	-15.06 c	0.45
Strain at Failure (%)	3.29 a	3.20	-2.72 a	3.30	0.10 a	0.87	3.23 a	3.30	2.33 a	0.64	3.18 a	3.41	7.28 a	3.36	5.69 a	3.05	-4.05 a	3.14	-1.02 a	3.45	8.52 a	0.24
$K_{elastic}$ (N/mm)	1148 a	1147	-0.09 a	1097	-4.39 a	0.20	**1185 a**	**1076**	**-9.17 b**	**0.00**	1216 a	1080	-11.17 b,c	1160	-4.59 a,b	1134	-6.75 a,b,c	1179	-2.99 a,b	1016	-16.47 c	0.08
K_{FEA} (N/mm)	**2037 a**	**2050**	**0.63 a**	**1940**	**-4.78 b**	**0.05**	**2115 a**	**1904**	**-9.99 b**	**0.00**	2180 a	1895	-13.08 c,d	2124	-2.57 a,b	1976	-9.34 b,c,d	2040	-6.40 a,b,c	1840	-15.61 d	0.35
E_{tissue} (GPa)	5.66 a	5.62	-0.73 a	5.65	-0.16 a	0.96	5.63 a	5.66	0.63 a	0.77	5.61 a	5.71	1.86 a	5.48	-2.24 a	5.76	2.63 a	5.79	3.18 a	5.52	-1.65 a	0.17
Stiffness (N/mm)	615 a	599	-2.62 a	595	-3.27 a	0.86	**638 a**	**567**	**-11.10 b**	**0.03**	640 a	590	-7.90 a	632	-1.34 a	566	-11.60 a	643	0.43 a	547	-14.62 a	0.84
Ultimate Force (N)	31.2 a	30.9	-1.08 a	29.0	-7.05 a	0.23	**31.6 a**	**29.1**	**-7.81 b**	**0.03**	32.5 a	29.9	-7.77 a	31.4	-3.41 a	30.4	-6.44 a	30.9	-4.66 a	27.0	-16.67 a	0.56
Ultimate Strain (%)	3.55 a	3.46	-2.41 a	3.34	-5.75 a	0.46	3.49 a	3.41	-2.33 a	0.55	3.63 a	3.47	-4.29 a	3.43	-5.38 a	3.49	-3.63 a	3.42	-5.67 a	3.27	-9.88 a	0.75
AGEs (ng quin. / mg coll.)	**39.0 a**	**36.6**	**-5.99 a**	**63.9**	**63.86 b**	**0.00**	45.4 a	47.6	5.02 a	0.52	36.2 a	41.8	15.64 a	32.9	-9.08 a	40.4	11.81 a	67.1	85.50 b	60.7	67.85 b	0.23
Tb.BMD (mg of HA / cm^3)	1066 a	1071	0.48 a	1064	-0.18 a	0.69	1067 a	1068	0.07 a	0.92	1070 a	1063	-0.62 a	1070	-0.01 a	1073	0.35 a	1062	-0.72 a	1067	-0.26 a	0.75
Ct.BMD (mg of HA / cm^3)	1205 a	1205	0.03 a	1204	-0.05 a	1.00	1207 a	1203	-0.32 a	0.62	1206 a	1203	-0.23 a	1205	-0.12 a	1205	-0.05 a	1209	0.25 a	1199	-0.57 a	0.85
Tb.Th Stand. Dev. (mm)	**0.011 a**	**0.011**	**1.74 a**	**0.013**	**16.5 b**	**0.00**	**0.013 a**	**0.011**	**-14.2 b**	**0.00**	**0.012 a**	**0.01**	**-14.8 c**	**0.012**	**-0.30 a**	**0.01**	**-11.3 c**	**0.014**	**17.6 b**	**0.012**	**-1.79 a**	**0.03**
Spleen Mass (mg)	**74.4 a**	**72.2**	**-2.96 a**	**59.8**	**-19.59 b**	**0.00**	**62.1 a**	**75.5**	**21.6 b**	**0.00**	**71.7 a**	**77.1**	**7.61 a**	**68.2**	**-4.87 a**	**76.2**	**6.34 a**	**46.5**	**-35.2 b**	**73.2**	**2.11 a**	**0.00**
Thymus Mass (mg)	36.09 a	35.35	-2.03 a	34.48	-4.46 a	0.55	**31.7 a**	**38.9**	**22.5 b**	**0.00**	33.9 a,b	38.3	38.3 a	38.3	12.94 b	39.8	17.4 a	30.4	-10.4 b	38.6	13.8 a	0.27

p values listed are from Two-Way ANOVA run with terms of Radiation, Latency, and the Interaction term
Adjusted least squares means shown for radiation at 0 Gy, 1 Gy, and 5 Gy; Also shown as a percent difference compared to 0 Gy
Adjusted least squares means shown for latency at 11-day and 12-wk; Also shown as a percent difference compared to 11-day
Unadjusted least squares means shown for the interaction term (radiation by latency) for 0, 1, and 5 Gy at 11-days and 12-wks
Rows in bold indicate significant parameters ($p < 0.05$) for the the term listed (i.e. Radiation, Latency, or Interaction)
Values with the same letter were not significantly different via a Tukey-Kramer post-hoc analysis (for Radiation and Interaction) or Student's t-test (for Latency)

Table A.2 – Animal information for mice used in *in vivo* irradiation study.

Species - Mouse; Strain - C57BL/6J; DOB - 5/10/16; Sex - male; Vendor - JaxWest

Dissection #	Dose	Cage #	Dissection Date	Mass (g) on arrival to NASA 9-week old (7/14/16)	Mass (g) Day of Radiation (9/9/16) or (9/10/16)	Mass (g) at euthanization (date varies)	continued...						
D12.7	0 Gy	84	11-day 9/19/16	24.6	30.6	31.0	D12.49	0 Gy	17	12-wk 12/01/16	25.4	30.9	34.4
D12.8	1 Gy	15	11-day 9/19/16	25.3	28.9	29.3	D12.50	1 Gy	14	12-wk 12/01/16	23.5	29.8	34.3
D12.9	5 Gy	64	11-day 9/19/16	25.4	25.7	26.4	D12.51	5 Gy	34	12-wk 12/01/16	25.3	28.3	30.8
D12.10	0 Gy	60	11-day 9/19/16	23.3	26.7	27.8	D12.52	0 Gy	65	12-wk 12/01/16	25.3	27.6	29.8
D12.11	1 Gy	66	11-day 9/19/16	25.4	30.0	30.3	D12.53	1 Gy	13	12-wk 12/01/16	26.1	28.5	32.8
D12.12	5 Gy	61	11-day 9/19/16	25.6	27.2	27.2	D12.54	5 Gy	77	12-wk 12/01/16	25.6	27.5	31.7
D12.13	0 Gy	1	11-day 9/19/16	24.3	28.8	28.7	D12.55	0 Gy	78	12-wk 12/01/16	25.1	27.3	29.3
D12.14	1 Gy	6	11-day 9/19/16	26.4	30.5	30.9	D12.56	1 Gy	70	12-wk 12/01/16	23.9	30.1	35.3
D12.15	5 Gy	19	11-day 9/19/16	22.7	26.5	27.1	D12.57	5 Gy	43	12-wk 12/01/16	24.4	26.0	28.2
D12.16	0 Gy	53	11-day 9/19/16	25.3	24.8	25.4	D12.58	0 Gy	28	12-wk 12/01/16	26.7	30.1	35.6
D12.17	1 Gy	38	11-day 9/19/16	23.8	24.4	25.3	D12.59	1 Gy	25	12-wk 12/01/16	25.7	27.4	29.6
D12.18	5 Gy	37	11-day 9/19/16	25.2	25.8	26.1	D12.60	5 Gy	32	12-wk 12/01/16	24.8	30.5	35.0
D12.19	0 Gy	52	11-day 9/19/16	25.5	28.1	28.5	D12.61	0 Gy	45	12-wk 12/01/16	27.4	29.7	32.2
D12.20	1 Gy	21	11-day 9/19/16	24.7	27.5	28.3	D12.62	1 Gy	10	12-wk 12/01/16	27.3	27.5	29.7
D12.21	5 Gy	42	11-day 9/19/16	25.2	29.8	29.7	D12.63	5 Gy	87	12-wk 12/01/16	24.0	27.9	28.4
D12.22	0 Gy	80	11-day 9/19/16	25.9	27.6	28.4	D12.64	0 Gy	51	12-wk 12/01/16	27.8	26.5	28.2
D12.23	1 Gy	74	11-day 9/19/16	27.3	24.8	25.8	D12.65	1 Gy	22	12-wk 12/01/16	24.7	26.3	29.4
D12.24	5 Gy	50	11-day 9/19/16	25.2	29.5	28.5	D12.66	5 Gy	26	12-wk 12/01/16	25.4	28.8	32.7
D12.25	0 Gy	73	11-day 9/19/16	26.5	27.4	28.9	D12.67	0 Gy	58	12-wk 12/01/16	27.3	29.4	32.5
D12.26	1 Gy	35	11-day 9/19/16	23.9	27.4	27.9	D12.68	1 Gy	49	12-wk 12/01/16	23.2	26.0	28.8
D12.27	5 Gy	3	11-day 9/19/16	24.0	26.2	27.2	D12.69	5 Gy	75	12-wk 12/01/16	26.8	26.7	29.6
D12.28	0 Gy	88	11-day 9/20/16	24.3	28.9	29.5	D12.70	0 Gy	44	12-wk 12/02/16	25.9	27.8	29.1
D12.29	1 Gy	39	11-day 9/20/16	23.9	29.0	29.4	D12.71	1 Gy	11	12-wk 12/02/16	25.0	29.9	30.8
D12.30	5 Gy	89	11-day 9/20/16	22.6	25.4	24.8	D12.72	5 Gy	46	12-wk 12/02/16	26.0	30.9	30.7
D12.31	0 Gy	82	11-day 9/20/16	23.1	28.3	29.4	D12.73	0 Gy	20	12-wk 12/02/16	24.3	27.0	29.1
D12.32	1 Gy	33	11-day 9/20/16	24.6	31.5	32.1	D12.74	1 Gy	48	12-wk 12/02/16	24.4	27.8	29.8
D12.33	5 Gy	2	11-day 9/20/16	24.6	29.5	28.9	D12.75	5 Gy	36	12-wk 12/02/16	25.3	29.6	31.0
D12.34	0 Gy	57	11-day 9/20/16	25.1	28.5	28.5	D12.76	0 Gy	67	12-wk 12/02/16	23.9	27.8	30.7
D12.35	1 Gy	4	11-day 9/20/16	23.1	31.0	28.5	D12.77	1 Gy	23	12-wk 12/02/16	24.3	27.7	30.3
D12.36	5 Gy	81	11-day 9/20/16	25.4	28.7	27.9	D12.78	5 Gy	56	12-wk 12/02/16	25.7	29.4	28.1
D12.37	0 Gy	29	11-day 9/20/16	23.5	26.0	26.3	D12.79	0 Gy	40	12-wk 12/02/16	27.0	30.5	34.1
D12.38	1 Gy	31	11-day 9/20/16	24.6	27.9	29.0	D12.80	1 Gy	85	12-wk 12/02/16	24.2	31.3	36.2
D12.39	5 Gy	72	11-day 9/20/16	27.0	27.8	26.5	D12.81	5 Gy	27	12-wk 12/02/16	24.2	28.6	30.5
D12.40	0 Gy	30	11-day 9/20/16	23.6	27.5	27.9	D12.82	0 Gy	9	12-wk 12/02/16	24.1	27.2	29.6
D12.41	1 Gy	68	11-day 9/20/16	25.7	25.9	26.6	D12.83	1 Gy	55	12-wk 12/02/16	25.7	29.6	34.6
D12.42	5 Gy	59	11-day 9/20/16	22.0	25.9	26.4	D12.84	5 Gy	18	12-wk 12/02/16	24.0	26.8	28.9
D12.43	0 Gy	76	11-day 9/20/16	23.8	29.6	29.0	D12.85	0 Gy	69	12-wk 12/02/16	26.7	27.0	29.6
D12.44	1 Gy	12	11-day 9/20/16	27.0	30.2	29.4	D12.86	1 Gy	63	12-wk 12/02/16	25.8	29.7	33.1
D12.45	5 Gy	41	11-day 9/20/16	26.8	27.7	27.9	D12.87	5 Gy	83	12-wk 12/02/16	23.4	26.7	29.5
D12.46	0 Gy	62	11-day 9/20/16	26.0	29.0	29.3	D12.88	0 Gy	54	12-wk 12/02/16	25.0	27.7	29.5
D12.47	1 Gy	47	11-day 9/20/16	26.8	26.8	26.9	D12.89	1 Gy	5	12-wk 12/02/16	23.6	28.2	32.1
D12.48	5 Gy	7	11-day 9/20/16	23.9	27.4	26.5	D12.90	5 Gy	79	12-wk 12/02/16	25.9	28.9	29.0

Gray-scale color indicates groups euthanized on different dates, see date listed

Table A.3 – Tissues collected and preserved from the *in vivo* irradiation study.

Order	Tissue	Purpose	Tissue Used?	Summary of Task	Initial 24 hours fixative and temperature	Final Preserve
1	Blood	AGEs crosslinks Pentosidine	No	Collect via cardiac puncture, Flush into serum separator tubes. 30 min @ RT	N/A	N/A
2	Left Femur	AGEs via Total Fluorescence	No	Flush with 200 µL PBS (-/-) keep pellet (Use new flush approach: Cut mid-diaphysis and flush outwards, try to preserve trabecular tissue at epiphysis). After collecting Bone Marrow flush until clean. Put in Lysis buffer with protease inhibitors (8 mL RIPA with 80 µL protease inhibitors) 1:100 ratio protease inhibitor:RIPA	N/A	-20C
	Left Femur Marrow	Bone Marrow Cells (BMC) for RNA	No	Spin pellet 5 min @ 1000 RPM. Resuspend with 350 µL RIPA, Flash freeze.	Flash freeze in Liquid Nitrogen @ -80C	-80C
4	Left Tibia	Bone for Protein	No	Flush with 200 µL PBS (-/-) keep pellet. After collecting Bone Marrow flush until clean. Put in Lysis buffer with protease inhibitors (8 mL RIPA with 80 µL protease inhibitors) 1:100 ratio protease inhibitor:RIPA	Dry Ice	-80C
5	Left Tibia Marrow	Bone Marrow Cells (BMC) for RNA	No	Spin pellet 5 min @ 1000 RPM. Resuspend with 350 µL RIPA, Flash freeze.	Flash freeze in Liquid Nitrogen @ -80C	-80C
6	Right Tibia	MicroCT & IHC	No	4% PFA	4% PFA at 4C for 24 hours.	Transfer to cold 70% EtOH (1.5 mL) & wash on rocker for 0.5-1 hr @ 4C. Then transfer to a new set of tubes with fresh, cold 1.5 mL of 70% EtOH. Store at 4C.
7	Right Femur	Mechanical Testing	No	Wrap in PBS soaked gauze	N/A	-20C
8	**Spleen**	**Animal Health**	**Yes**	Measure and record mass	N/A	N/A
9	**Thymus**	**Immune Response**	**Yes**	Measure and record mass	N/A	N/A
10	**L1-L2**	**Collagen Fragmentation**	**Yes**	Wrap in PBS soaked gauze	N/A	-20C
11	**L3**	**IHC**	**Yes**	4% PFA	4% PFA at 4C for 24 hours.	Transfer to cold 70% EtOH (1.5 mL) & wash on rocker for 0.5-1 hr @ 4C. Then transfer to a new set of tubes with fresh, cold 1.5 mL of 70% EtOH. Store at 4C.
12	**L4**	**MicroCT & Monotonic Testing**	**Yes**			
13	**L5**	**MicroCT & Fatigue Testing**	**Yes**	PBS soaked gauze	Wet ice and then -20C	-20C
14	**S1**	**Collagen MW**	**Yes**	Flush with PBS (-/-). No need to collect bone marrow. Put in Lysis buffer with protease inhibitors (8 mL RIPA with 80 µL protease inhibitors) 1:100 ratio	Dry ice	-80C
15	Carcass	Future tissue if needed	No	N/A	Wet ice and then -20C	

21 Total mice per dissection ~8 hrs
Tissues in bold were tested and the results are presented in this dissertation
Remaining tissues were collected and are stored at NASA Ames Research Center Bone & Signaling Lab under Exp 12 with PI: Joshua Alwood

A.3 Additional Figures for Chapter 4

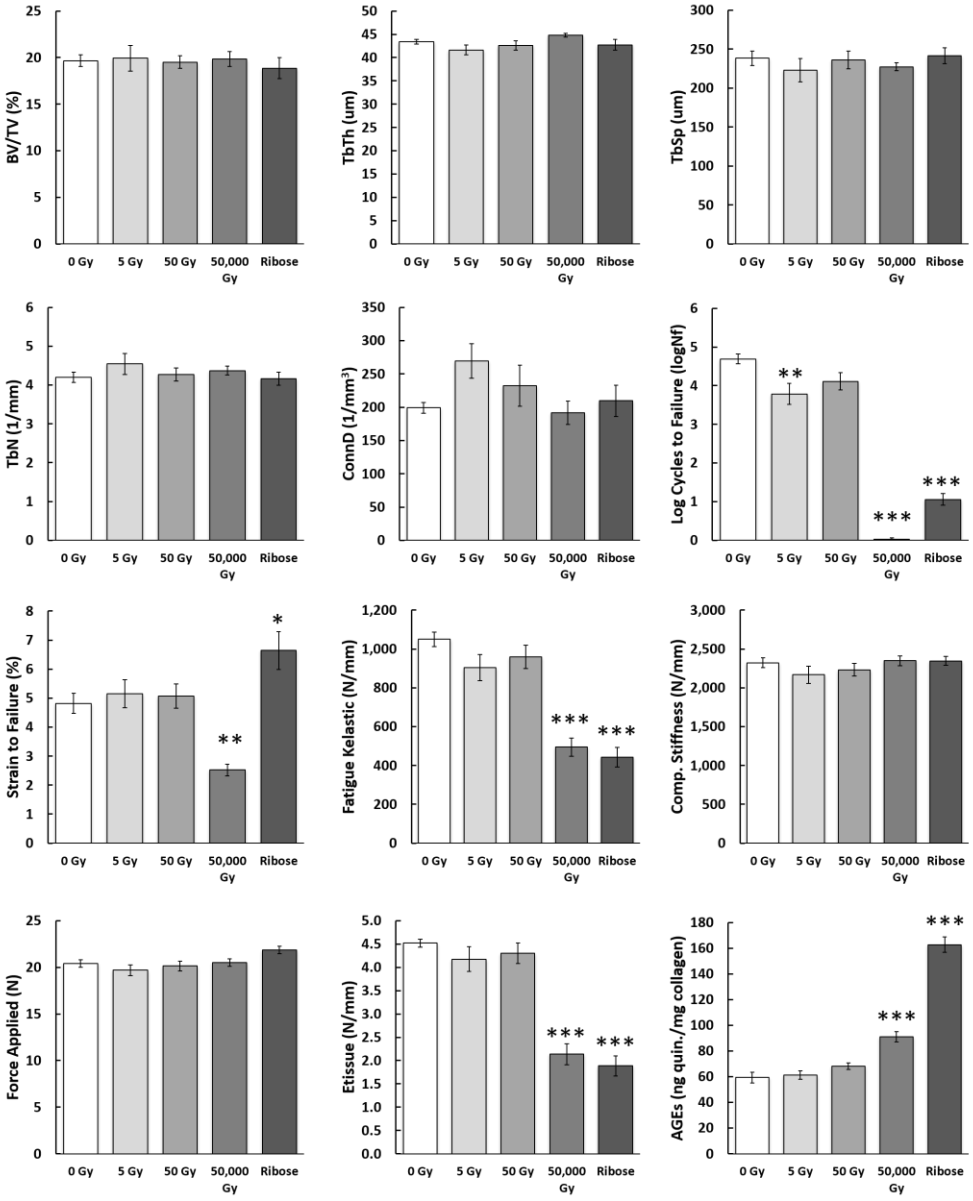

Figure A.14 – Results from micro-CT, mechanical and biochemical testing for *ex vivo* irradiation of mouse vertebra. These were tested prior to the specimens presented in Chapter 4. Irradiation groups were 0, 5, 50, and 50,000 Gy and a ribose treated group. Ribose treated specimens were soaked in a D-ribose solution for 14 days (1X PBS with pH ~7.4 with 0.1% sodium azide and 100 mg/ mL of D-ribose at 37°C). Microarchitecture results confirm there were no differences in size, shape, or structure of the L4 and L5 specimens used in mechanical testing. (There was no monotonic testing conducted for this study because both L4 and L5 specimens were tested in fatigue. The fatigue parameters shown combined L4 and L5 because there were no significant differences between groups found.) The 50,000 Gy specimen could not withstand even one cycle, likely due to collagen fragmentation. Ribose AGEs are nearly 3X the control amount and 2X the 50,000 Gy group, which may account for the reduced fatigue life observed for this group. The reduced fatigue life shown for 5 Gy may have been an artifact of poor specimen preparation and not removing enough of the angled-caudal endplate. This improved in future studies including the *in vivo* irradiation and future *ex vivo* irradiation studies presented in Chapters 3 and 4. Results shown are least squares means with 95% confidence intervals. * represents $p < 0.05$, ** represents $p < 0.01$, and *** represents $p < 0.001$.

Appendix B – Standard Operating Procedures & Engineering Drawings

The following appendix provides detailed standard operating procedures for various assays and analyses performed during this research. It also contains engineering and assembly drawings for any parts that were designed and built for this research: 3D-printed fixture, spherically-seated upper platen, lower platen, and water bath.

B.1 Standard Operating Procedure for specimen preparation of a mouse lumbar vertebrae

University of California, Berkeley
Berkeley Biomechanics Lab
Standard Operating Procedure

Specimen Preparation for Mouse Lumbar Vertebrae

SOP, Version 3
Date: 06/26/2018

Author(s): Shannon R. Emerzian & Megan M. Pendleton
Principal Investigator: Tony M. Keaveny

Summary: This protocol outlines the steps needed to isolate a vertebral body from an L4 or L5 mouse vertebra. It ensures plano-parallel surfaces for uniaxial compression testing (monotonic or cyclic loading).

Key Words: mouse, vertebral body, mechanical testing, sample preparation

Materials (for 3 samples):

- 3 3-D printed fixture
- 1 pin gauge/drill bit (to measure spinal canal/support vertebrae during potting)
- 1 curved tip syringe
- 1 small mixing cup (e.g. mini solo cups)
- 1 popsicle stick
- 4 mL PMMA powder
- 2 mL PMMA liquid
- 2 Plastic graduated centrifuge tubes (~15mL; to measure PMMA)
- 1 Funnel (to pour PMMA into graduated tubes)
- PBS 1X
- Disposable transfer pipettes
- Gauze
- Scalpel

Equipment:

- Benchtop vice
- Diamond Saw Microtome (Leica SP1600)

Steps:

1. Fixture prep
    a. 3D print fixtures ("DiamondSawFixture_Swept5_most recent.stl") Which can be found under Resources on the Berkeley Biomechanics website http://oconnell.berkeley.edu/resources/
    b. Label each fixture with its corresponding sample number and level (e.g. D11.23 L4)
    c. Measure inner diameter (ID) of spinal canal with a pin gauge or a drill bit, the shank side, not the cutting edge (measure cranial to caudal). Look for a snug fit that prevents the vertebrae from easily or freely rotating about the gauge. Record this value.
    d. Drill out support pin hole in 3D printed fixture to be 0.001" larger (or one drill bit size larger) than the measured spinal canal ID
2. Potting the specimen
    a. Place drill bit through the spinal canal of the vertebrae. Double check that the vertebrae does not freely slide or rotate - the fit should be snug.
    b. Secure the drill bit and vertebrae in the fixture (see video for proper alignment).
    c. Cut approximately 2 mm of the tip of the syringe off. Ensure the tip is open.
    d. Measure 4 mL of PMMA powder (using a funnel to pour into a 15 mL graduated centrifuge tube, or similar). Separately, measure 2 mL of PMMA liquid catalyst. **Note: 4 mL powder + 2 mL liquid will be enough to pot 3 samples**
    e. In a small mixing cup, combine the PMMA components. Stir with a popsicle stick or equivalent until the powder is completely dissolved.
    f. Quickly, suck up PMMA mixture in curved tip syringe.
    g. Beginning on the caudal side, inject a layer of PMMA until it just wicks to the bone. Do the same from the cranial side. Repeat for each sample. Once the first layer has been placed for each sample, go back and retouch as needed. Ensure the processes are adequately secured in the PMMA.
    h. Once you have finished with the PMMA, dispose of the syringe, mixing cup, and mixing stick.
    i. Cover the vertebrae with several drops of PBS while the PMMA sets.
    j. Once the PMMA has completely set, gently slide the drill bits out of the fixtures.

Figure B.15 – Mouse lumbar vertebrae with posterior processes potted in PMMA

3. Cutting plano-parallel surfaces with microtome

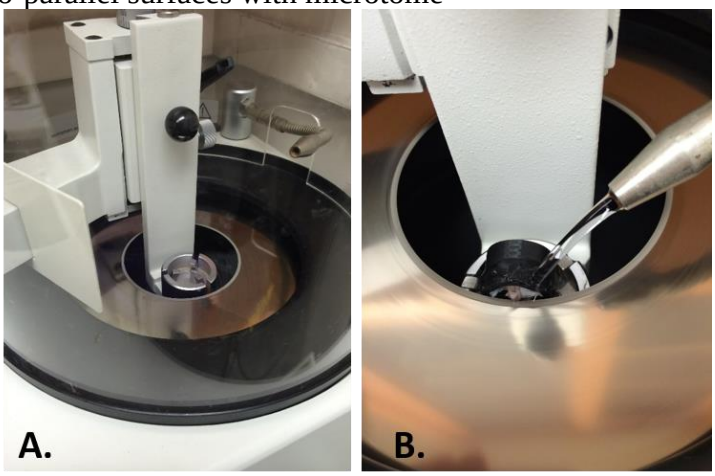

Figure B.16 – (A) LeicaSP1600 diamond-saw microtome without sample loaded. (B) 3D fixture in place with potted vertebrae undergoing cut with internal blade under irrigation. 3D fixture was printed in black during early designs.

a. General Instructions: Using the Leica SP1600 Saw Microtome, cut two parallel cuts (caudal side, then cranial). Ensure your cut removes all of the intervertebral disc, as well as the end plate, on each end of the vertebral body.
b. **NOTE**: You must be trained on safe use of this saw and approved by Candice/Ruth before operating without supervision.
c. **PPE**: You must wear a face shield and hearing protection while using the diamond saw.
d. **NOTE:** wear and tear on the machine is a possibility, I have had to replace the motor belts before located on the underside of the microtome, so if you hear/see anything unusual check to see if parts need replacing
e. Mounting:
    i. Pick up the object holder by its black knob and raise the object mount out of the cutting area.
    ii. Secure the 3D printed fixture into chuck, oriented cranial end up. Ensure the chuck (knurled wheel) is well tightened.
f. Setting the height
    i. Holding the black knob, lower the object holder and bone into the cutting area.
    ii. Align the blade to cut just below the endplate and intervertebral disc on the cranial end of the vertebral body.
    iii. Note: Alignment can be checked by allowing the object arm to be moved closer to the blade (without touching the blade!) while the saw is off.
g. Cranial Cut
    i. Turn on the water tap and adjust the water flow with the valve located at the back of the machine. Align the nozzle so that the water jet lands on the edge of the saw blade.
    ii. Turn on the motor with the switch.
    iii. Unclamp the object by pulling the stop pin. To save time, the speed of the object feed can be increased while the object is guided towards the edge of

the blade. To do this, turn the knurled knob on the left-hand side of the machine clockwise.

iv. Once the sample is close to the blade, reduce the arm speed down to 8. Ensure the speed is set to 8 before cutting to ensure a smooth and even cut.
v. Allow the saw to cut entirely through the vertebral body.
vi. After the object has passed through the saw, turn the object arm back as far as it will go. It clicks into place audibly.
vii. Press the switch to turn off the motor.

h. Caudal Cut
   i. First set the scale ring (bottom ring) to 0 (a height adjustment is not yet made).
   ii. To set the section thickness, turn the knurled knob at the top anticlockwise approximately 4.5 full rotations. Note: Every division on the scale represents 10 µm. When setting section thickness, the thickness of the saw blade (approx. 300 µm) must always be taken into account. For example, a setting of 400 µm is necessary to obtain a 100 µm thick section.
   iii. Stop at the chosen specimen height. Again, check alignment by allowing the object arm to be moved closer to the blade (without touching the blade!) while the saw is off.
   iv. Switch on the motor.
   v. Then release the object arm clamp. Set the feed to the maximum rate until the object has almost reached the saw blade. Use a slower speed
   vi. for cutting (see above, 3.6.5 - speed should be 8 while cutting).
   vii. Once the cut has completely passed through the vertebral body, turn the motor and water off, raise the object arm above the blade, and loosen the chuck to allow the fixture to be removed.

4. Remove vertebral body from fixture
   a. Returning to a lab bench, secure the 3D printed fixture in a vice, with the vertebral body oriented vertically.
   b. Using a scalpel, in a gentle sawing motion cut behind the vertebral body, over the spinal canal along the processes.
   c. Once the sample has been removed from the fixture, gently remove any soft tissue and the cut disc + endplate.
   d. Store in PBS soaked gauze in the freezer.
   e. Optional: Your samples are now ready for *ex vivo* treatment (radiation, ribose, etc.).

B.2 Standard Operating Procedure for image processing needed prior to FEA

University of California, Berkeley
Berkeley Biomechanics Lab
Standard Operating Procedure

Image Processing of Mouse Vertebrae

SOP, Version 1

Date: 07/14/2017

Author(s): Shannon R. Emerzian and Megan M. Pendleton
Principal Investigator: Tony M. Keaveny

Summary: This protocol guides you through the image processing steps needed to go from the original micro-CT scans to the final stack needed later for the FEA model. This protocol does not include steps for the mesh and FEM. The original micro-CT images were taken by Alfred Li at the Bone Imaging Core Facility (SFVA and UCSF; PI is Prof. Wenhan Chang). The details of the micro-CT scanning are listed just prior to the image processing steps.

Key Words: ImageJ, micro-CT, thresholding, reorientation

Materials:

- Original DICOM or TIFF stack of images from micro-CT
- Software: ImageJ or Fiji with pluggin 3D Viewer
- Software: DataViewer
- Data collection sheets (for tracking progress)

Equipment:

- External Hard Drive (because multiple stacks will add up to large amounts of data rather quickly)

Micro-CT details:

- Scanning medium: 1X PBS
- Loading notes: Thaw for 30 minutes, orient cranial end on top, load L3-L4-L5 in succession; After scanning, wrap in PBS-moistened gauze and store at -20C
- Instrument: Scanco Medical µCT 50 specimen scanner
- Holder: 35mm
- FOV: 15mm
- Region of scan: region spanning three vertebrae
- Slices: variable
- X-ray settings: 55kVP potential, 109µA current
- Voxel size: 10µm
- Integration time: 500ms
- Projections: 1000 per 180 degrees

Steps (Image Processing):

1. Fiji/ImageJ Part I - this begins from the original DICOM stacks made from micro-CT

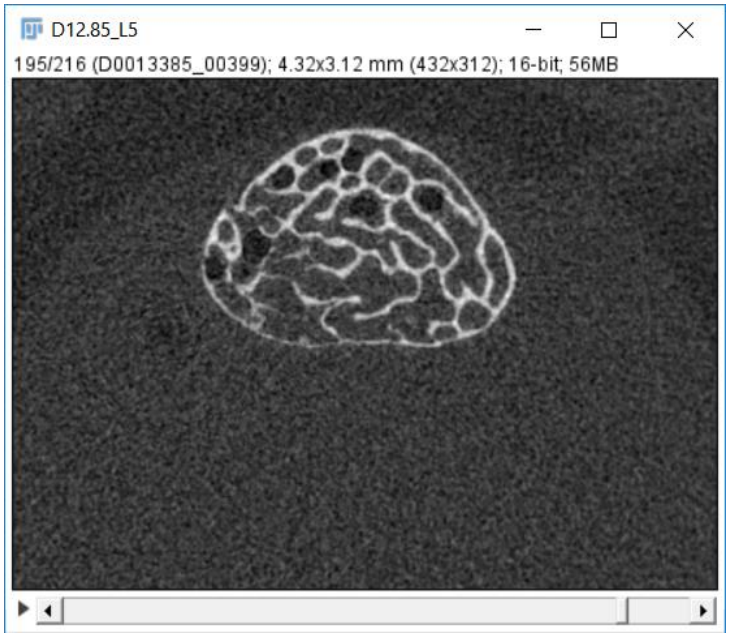

Figure B.17 – Original DICOM image of a caudal cross section of mouse vertebral body opened in ImageJ or Fiji.

a. Install Fiji (this is just ImageJ, but with plugins - including 3D viewer; BoneJ is not included, but it is ImageJ with different plugins).
b. Open Fiji on your computer.
c. File->Import ->Image Sequence. Click on the first DICOM file of the series of DICOM files. Press OK. Image sequence will open in Fiji.
d. Visually inspect the file to separate L4/L5. Scroll through images and record the slice numbers making up each vertebra in lab notebook. Note: L4 will always be on top, both L4 and L5 will be oriented cranial to caudal.
e. Quick visual inspection:
    i. Quickly threshold (you will not be saving this) through Image>Adjust>Threshold. Make sure "dark background" and "stack histogram" are checked. Use "Default" threshold mode. Click Apply.
    ii. New window will pop up called "Convert Stack to Binary". Ensure everything is unchecked except "Black background (of binary masks)"
    iii. Open in 3D viewer (Plugins>3D Viewer>OK) to visually inspect vertebrae; make notes of any irregularities, concerns, etc.
    iv. Close 3D viewer

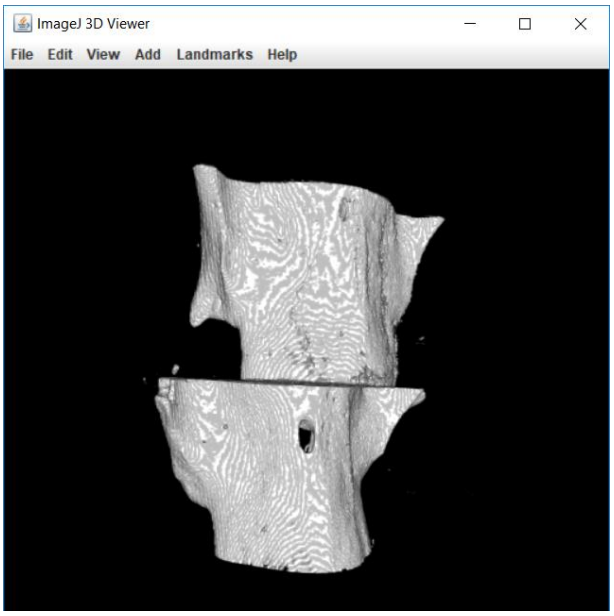

Figure B.18 – L4 and L5 mouse vertebral bodies imaged with micro-CT and opened in 3D Viewer.

f. Create two separate folders (D11b.X_L4, D11b.X_L5), and copy and paste the DICOM files for each level into their respective folders.
g. Close stack - reopen L4 or L5 stack only. (File>Import>Image Sequence> L5 folder double click on first image, OK)
h. Scroll over a slice that has bone in it (choose a caudal region)
i. Image -> Adjust -> Threshold (also ctrl+shift+t). MAKE SURE "DARK BACKGROUND" is checked. Check "Stack Histogram" to threshold for ALL slices. Use "Default" threshold mode (drop down menu). "Apply".

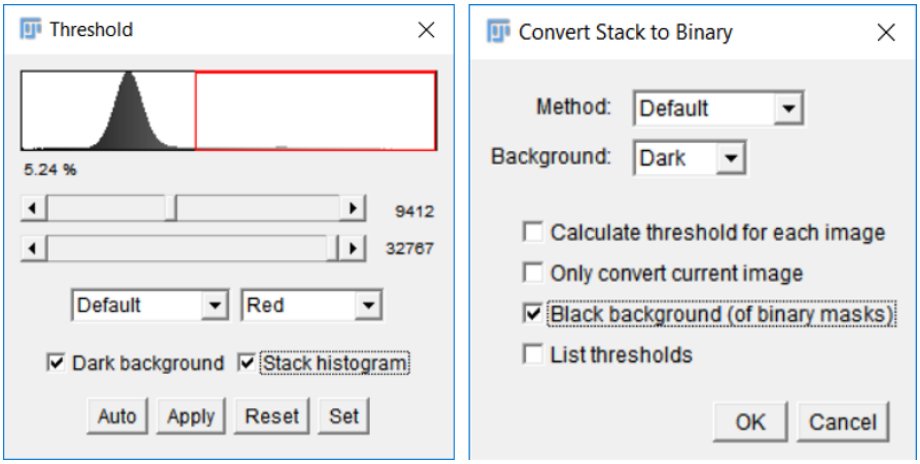

Figure B.19 – Thresholding settings in ImageJ. The bounding values will differ between samples.

j. Ensure the only thing checked on the new window is "Black background (of binary masks)". "OK" Image is now in black and white.
k. Document the threshold values (numbers at top slider bar and bottom slider bar). Click Apply.

l. Save what you have so far. File -> Save As -> Image Sequence. Save as BMP format and press OK. Then make a new folder in your computer directory to put all your processed files. (D11b.X_L5_Thresh1_BMPs) Note: In the future for image processing, it is best to hold thresholding until the very last step. Simply save the grayscale images as BMPs so they can be opened by DataViewer. DataViewer is going to change the images back to grayscale after saving the file, this is why we must repeat the threshold after the DataViewer steps (see below).

2. DataViewer
    a. Download DataViewer (Bruker micro-CT Software Downloads)
    b. Open DataViewer and import the file with the thresholded images (Actions>Open>Open Dataset, find your folder and double click on first image). Click "Load for 3D Viewing" icon (third button from left)
    c. Input the pixel size from the scan (10 um/vox in this case, for both x and y) Note: this value will change if your scans are done at a lower/high resolution (e.g. the rat vertebrae scanned in LKS at UC Berkeley are typically 20.7 um)
    d. Select a cranial region of the bone for reorientation (bottom slice)
    e. Reorient the three images.
        i. To change the plane, drag the horizontal and vertical axes bars.
        ii. To reorient, hold down ctrl and drag
        iii. Make sure to take a cut down the middle of the bone cross section. (Look at the top view to get the planes in the correct locations)
        iv. Reorient the frontal view (right bottom image) so that the top and right edges of the bone make a 90-degree angle. The bottom of the bone should be as close to horizontal as possible.

v. Tilt the bottom left image so that the tip look to be pointing up, and the bottom appears “flat”

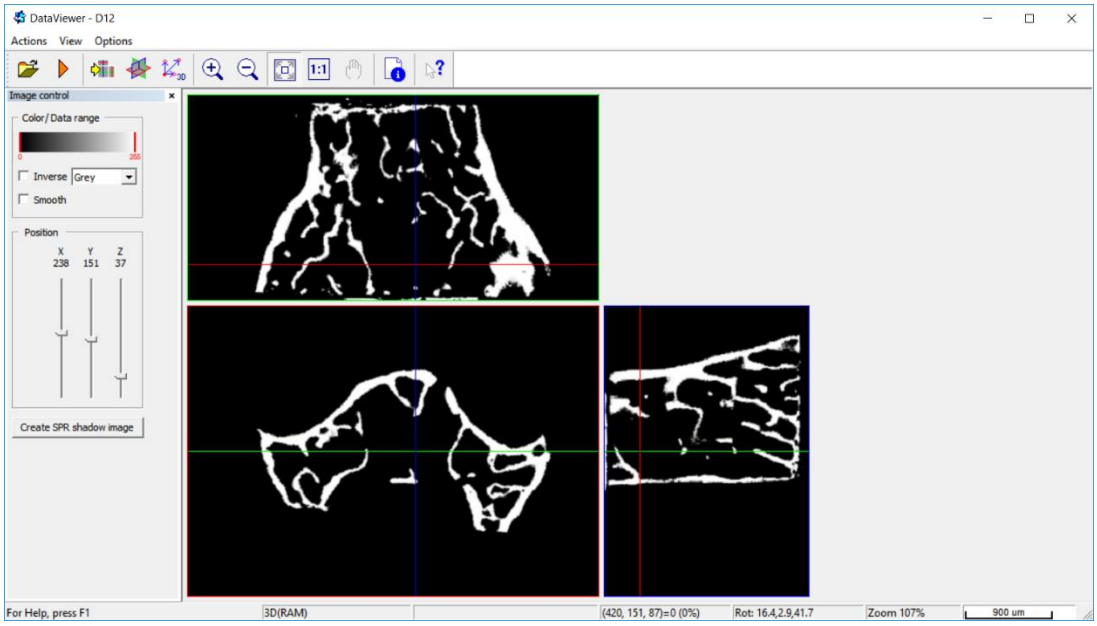

Figure B.20 – Reorient samples along the z-axis by using DataViewer

f. Actions→ Save→ Transaxial (X-Y) Image as a dataset
g. Save as a new folder (D11b.X_L5_Reorient).
h. While still open in DataViewer, now mark down which slices to remove. Click Z axis so you can adjust one slice at a time. Anything with “grey” do NOT take! Mark down which slices to remove on either end.
i. Go into “Reorient” folder and take the slices only. Copy and paste into Reorient_Truncate folder.
j. Delete slices to remove on either end.

3. Fiji/ImageJ Part II
   a. File > Import > Image Sequence (Open “reorient truncate” folder)
   b. These files are back in greyscale (even if it doesn’t look like it).
   c. Do a quick threshold (stack histogram, black background, apply) and open in 3D viewer. Inspect for anything to erase (extra pieces, broken pieces of bone, from other vertebrae, etc.)
   d. Close everything and reopen image sequence - still in greyscale!
   e. Use arrows to scroll through stack to find pieces to erase
   f. Eraser - double click to adjust brush width and color (black)

g. Threshold (ctrl + shift + T). Check “Stack Histogram”. Write down threshold numbers BEFORE hitting apply! “Apply” “Black Background” “Okay”

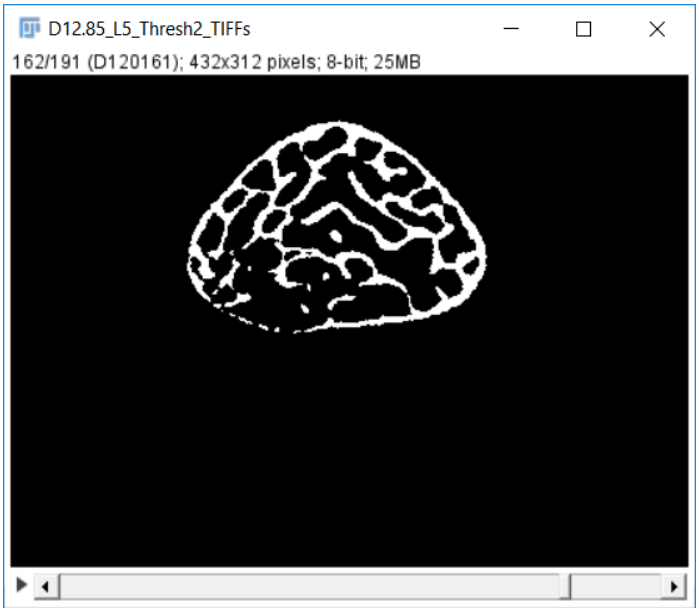

Figure B.21 – Representative image after thresholding in ImageJ

h. Record specimen height: write down total number of slices, multiply by voxel size.
i. File > Save As > Image Sequence > TIFF > OK (save in folder D11b.x_L5_Thresh2_TIFFs) IMPORTANT: Be sure to save files as D11b.X_L5 and allow the auto index to immediately follow (e.g. D11b.1_L50000, D11b.1_L50001, etc.) or you will have to edit a file in the FEA steps for each sample.
j. Note: This final TIFF stack will be used to continue with the mesh and model steps needed for FEA.

B.3 Standard Operating Procedure for monotonic compression testing of mouse vertebra

University of California, Berkeley
Berkeley Biomechanics Lab
Standard Operating Procedure

Monotonic Compression Testing of Mouse Vertebral Body

SOP, Version 1
Date: 06/31/2017

Author(s): Megan M. Pendleton & Shannon R. Emerzian
Principal Investigator: Tony M. Keaveny

Summary: This protocol outlines the steps to conduct a monotonic (loaded once to failure) compression test of an L4 mouse vertebral body. (See Specimen Preparation protocols for how to prep these samples.) This mechanical test is conducted on the TA ElectroForce 3200 (previously Bose ELF). *It is very important that you set appropriate and tight displacement and force limits for the test, and have the correct tuneIQ parameters, if not, this will lead to load cell damage which will have to be replaced and recalibrated.* Watch the videos in the Keaveny SOP folder on fatigue testing to become familiar with the equipment.

Key Words: mechanical testing, monotonic compression, mouse, vertebrae

Materials:

- Bone (e.g. L4 mouse vertebral body)
- KimWipes
- Gauze
- 1X PBS

Equipment:

- TA ElectroForce 3200
- 225 N load cell
- Load cell allen wrench
- Spherically-seated upper platen
- Lower platen
- Platen allen wrench
- Water bath (optional, because test is short)
- WinTest7 software

Steps:

A. Starting up computer and machine

1. Bose Computer username: user1, password: user1
2. Turn on signal conditioner and amplifier (switches on back side). Note: These have a 30-minute warm up!
3. Open software: WinTest7 (no username/password - just hit enter) Note: if the software won't open, restart the computer
4. Project file has limits etc. set - you can open different test files within project file (monotonic test, or fatigue test)
5. File > Open > From unsecure workspace > Project -- open project file 12-373 [this is the most recently calibrated file]
6. Displacement (reading from LVDT inside crosshead) and load are displayed (relevant), 225 N load cell is not hooked up, axial command displays voltage control of displacement (how much voltage is added to get to set displacement) Note: if all windows are black, voltage control; blue for displacement or load in displacement control
7. Monotonic test will be in displacement control
8. Before you turn on the power: adjust mover> control channel > direct command (safe way to start)

9. Under Specimen PreTest Setup,
    a. Adjust Mover>Control Channel: 6 parameters (P, I, D, 3 proprietary Bose gain values). For this test, we only want PID, proprietary values are zero.
    b. Presets: displacement or load - reading that channel but running in voltage control. Usually one is 0 and one is preload (-0.8 N). Rate in V/s (usually 0.1)
10. Under Waveform Setup
    a. Waveform Setup > Ramp
        i. Control channel: Disp
        ii. Move type: Relative (or absolute)
        iii. Ramp parameters: Level mm (-0.4), Rate mm/s (0.01)
        iv. Hit OK to save!
11. Test Limits > Limits
    a. Disp: min -3, max 6.5, controlled stop (this is set under waveform set up, waveform actions, controlled stop action -- position 0.191 V (0.2mm) <<- just remember to start sample testing at zero to make sure if it fails it goes above the sample)
12. When tuning - tune without upper platen! But we are going to manually insert controller values, so this isn't necessary, but if you need to tune...first, turn on (mover power > on) In Waveform setup, sine > Cyclic parameters (0, -1) > TuneIQ Run -- now switched into displ control, click preset 1, goes back to voltage control and returns to 0 mm
13. When mover power is turned off and on, it moves back to almost 0, but not quite (set voltage) - to avoid it from moving, put the crosshead at 0 and movement will be minimal

B. First Sample of the Day

1. Connect upper platen to actuator; connect load cell to bottom.
2. Specimen PreTest > adjust mover > control channel > displacement. Check controller values but return to direct command if power is on. If you want to change the values, turn mover power off and move to displacement control.
3. Once in displ control Mover > set axial tuning
    a. P = .4
    b. I =0 .009
    c. D = -1.7
4. Before turning on, return to direct command Specimen PreTest > adjust mover > control channel
5. Mover Power on.
6. Click preset 1: 0 mm to return to 0
7. Ready to test!
8. Submerge bone in PBS once at room temp
9. Double check limits - we care mostly about minimums
    a. Leave load limit at -60 N, 50 N

b. Displacement max will be 6.5
c. Displacement min will start at -3mm -- this will change once we set the specimen

10. Verify PID controller is okay: adjust mover > control channel
11. Check axial displacement > ramp -- disp control, relative, min level -0.4 and rate 0.01 mm/s -- Note: make sure you go back to "Ramp", then click "Ok"
12. Preset 1 to disp = 0 mm, Preset 2 to load = -0.8 N (right click > preset properties)
13. Click Preset 1 (displacement is 0)
14. Data Acquisition > Standard Timed Data
    a. Scan Points = 1000
    b. File Info, set destination folder , browse... C: > Bose > WinTest > Unsecure Workspace > TestData > Shannon > Project folder
    c. File Info, set filename: *note: you cannot use periods* D11bpoint(##)_L4_mono
    d. Click SAVE
15. Check and make sure load cell is at zero, but do not tare the displacement. To tare load cell: right click > properties > auto
16. When untightening upper platen: 1-2 rotations per screw, unscrew diagonally
17. Put a small amount of PBS on bottom platen surface to hold bone in place. Use forceps to position. Anterior left, posterior to right; caudal up, cranial down. Try to place bone in the middle of platen.
18. Once bone is in position, raise bottom platen until bone is nearly touching the top. Use allen wrench to lock into place (tightly).
19. Preload to -0.8 N using Preset 2
20. Tighten upper platen using tiny allen wrench (tighten diagonally).
21. Recheck waveform setup (-0.3mm at 0.01 mm/s)
22. Calculate limits. (e.g. if disp is now at -0.46mm, we will add -0.35 = - 0.81 mm as minimum limit). Reset new lower displacement limit (ENSURE this is negative)
23. Now, preload to - 1N by resetting Preset 2. Click Preset 2.
24. Wait 30 seconds. If running another sample, place it in room temp PBS to soak.
25. Record data: standard timed data > start (now it is collecting data)
26. Manage Test > Run > Zero Start
27. Once test has finished, Preset 1 and return to 0mm (get off bone)
28. Go to folder - verify 2 files show up. CSV (use to plot) and TDF (binary output - we don't use this).

C. Second Sample of the Day

1. Next sample should be soaking in room temp PBS
2. Remove previous sample by lowering bottom platen (large allen wrench to loosen), use little allen wrench to loosen spherically seated platen (usually one turn each time the first time, then do it again).

3. Check platen alignment by putting bottom platen up near upper platen - move upper platen slightly as needed.
4. Computer
    a. Limits → change max displacement back to -0.99 mm
    b. Reset Preset 2 to -0.8 N
    c. Click Preset 1 (0 mm)
    d. Standard Timed Data, "set filename" to sample number, click save
5. Tester
    a. Wet top of bottom platen surface with PBS - put one drop and dab with kimwipe (don't need a lot of PBS, just want enough to get sample to stick)
    b. Use forceps to remove any soft tissue above two testing surfaces
    c. Use forceps to place sample in center of bottom platen: caudal up, cranial down, anterior to the left, posterior to the right.
    d. Raise bottom platen - place allen wrench in, but do not yet tighten - raise until sample is just barely touching upper platen surface and tighten
6. Computer
    a. Click Preset 2 (-0.8N)
7. Tester
    a. Once preloaded to -0.8, use small allen wrench to finger tighten the set screws on the upper platen -- just until the nut is flush with the platen -- do not overtighten or platen will be off of the sample
8. Computer
    a. Take whatever displacement you are at (e.g. -0.31) and subtract 0.35 (want 0.3 displacement, plus margin of 0.05, e.g. -0.31 + -0.35 = -0.66mm)
    b. Change max displacement limit to number calculated above (e.g. -0.66mm)
    c. Change Preset 2 to -1N, and click
    d. ** To give time to settle, take next sample out and put next sample in PBS
    e. Standard Timed Data, start (to collect data)
    f. Click "Run" and then "Zero Start"
    g. Let test run - watch displacement/load - you'll see test finish at top
    h. Click Preset 1 (0 mm) to get off sample

D. Finished for the Day

1. Move back to 0 mm
2. Turn Mover Power Off

B.4 Standard Operating Procedure for cyclic compression testing of mouse vertebra

University of California, Berkeley
Berkeley Biomechanics Lab

Standard Operating Procedure

Cyclic (Fatigue) Compression Testing of Mouse Vertebral Body

SOP, Version 1
Date: 06/31/2017

Author(s): Megan M. Pendleton & Shannon R. Emerzian
Principal Investigator: Tony M. Keaveny

Summary: This protocol outlines the steps to conduct a fatigue (loaded cyclically to failure) compression test of an L5 mouse vertebral body. (See Specimen Preparation protocols for how to prep these samples.) This mechanical test is conducted on the TA ElectroForce 3200 (previously Bose ELF). This is a load-controlled test. *It is very important that you set appropriate and tight displacement and force limits for the test, and have the correct tuneIQ parameters, if not, this will lead to load cell damage which will have to be replaced and recalibrated.* Watch the videos in the Keaveny SOP folder on fatigue testing to become familiar with the equipment and this test.

Key Words: mechanical testing, monotonic compression, mouse, vertebrae

Materials:

- Bone (e.g. L4 mouse vertebral body)
- KimWipes
- Gauze
- 1X PBS

Equipment:

- TA ElectroForce 3200
- 225 N load cell
- Load cell allen wrench
- Spherically-seated upper platen
- Lower platen
- Platen allen wrench
- Water bath (optional, because test is short)
- WinTest7 software

Steps:

A. Computer Start-Up (if previously off)

1. Turn on
2. Log into Bose Computer username: user1, password: user1
3. Turn on signal conditioner and amplifier (switches on back side). Note: These have a 30-minute warm up!
4. Open software: WinTest7 (when popup comes to enter username password, there is no username/password - just hit enter) Note: if the software won't open, restart the computer

5. Blank screen - it's okay!
6. File > Open > From unsecure workspace > Project > 12-373 (PRJ file) [opens project file]
7. Test File > Open > Test for Group 1 > MeganPendleton > FatigueVertebraeCompressionProtocol_MMP_20160120 [opens test file]
8. Limits; Note: Limits are always set to "Controlled Stop" and the user must be sure to set the controlled stop value to a voltage that will ensure the platen comes up and off the sample
    a. Disp: Minimum = -0.8mm
    b. Load: Minimum = slightly larger than F_max (e.g. 23.22 N max, set to 23.5 N)
9. Presets
    a. Preset 1: change to displacement, 0 mm, 0.1 V/s
    b. Preset 2: load, -1 N, 0.1 V/s
10. Mover Power must be OFF!
11. Since we will be running in load control, must make sure we are in load control. Adjust Mover > Control Channel > Load > Ok (you can verify this switch -- if you look at load window to right, it will be in blue for load control)
12. Mover > Set Axial Tuning: *Important Note: The tuneIQ parameters listed are highly unstable to allow for such agile cyclic testing. Do NOT raise the platen off the sample unless using a preset (voltage controlled). If so, the actuator will look for something hard to press down on, and slam into the load cell below and likely break it.*
    a. This will show values from the most recent TuneIQ -- we are now changing for load control
    b. TuneIQ 1 = 0.090512
    c. TuneIQ 2 = 0.026045
    d. TuneIQ 3 = 0
    e. TuneIQ 4 = 266
    f. TuneIQ 5 = 0.054584
    g. TuneIQ 6 = 20.996632
    h. Click Ok to apply
13. Adjust mover > control channel > DirCmd (to get back into direct command mode) > Ok
14. Check to see if Current Command = 0.191. If not, 0.191 > Apply > Ok
15. Waveform Setup
    a. Click the Sine tab
    b. Control Channel: Load
    c. Move Type: Absolute
    d. Cyclic Parameters: Level 1 (F_min = -2.32), Level 2 (F_max = -23.22)
    e. Frequency = 8
    f. Cycle Count = 1,000,000

g. Start and finish parameters -- these do not have any bearing on the test EXCEPT Initial Cycles = 0
h. Click Ok (to make sure it saves)

16. Standard Timed Data
    a. Channels: Make sure Disp, Load and Axial Command are checked
    b. Scan Points: 1000
    c. First Scan Info: Immediate
    d. Subsequent Scan Info: 1 sec between scans
    e. File Close info: all three boxes are checked
    f. Set file to save in (Shannon, D11b Fatigue), change file name (D11bpointX_L5)
    g. Click Save

B. Setting Up a Sample

1. Secure adjustable platen to top
2. Secure load cell and water bath to base

Figure B.22 – Experimental set-up with spherically-seated upper platen, lower platen, water-bath, and load cell all in place. Water-saline solution has not been added yet.

3. Turn Mover Power ON
4. Load bone onto bottom platen - lock into place with top platen just touching top of bone. Ensure the bone is centered on the platens in all direction.
5. Apply -1N preload
6. Lock top fixture into place
7. Fill water bath with PBS
8. Update Preset 2 to F_min
9. Click Preset 2
10. Write down reference displacement (e.g. -0.29mm)
11. Limits: check to make sure they are tight!
    a. Min load should be around -1N on top of F_max
    b. Disp min = tight! Set to be -0.3mm + reference disp (e.g. -0.6mm)

12. Standard Timed Data > Start (data collection)
13. Run > Zeroed Start
14. Record where the displacement immediately jumped to (e.g.- 0.32mm)
15. Adjust displacement minimum limit to be
    a. 10% of sample height + 'jumped to' displacement (e.g. height = 1.75mm, then we want 1.75*0.1 + 0.32 = 0.495mm ← make sure you put this in negative)

C. After Test is Complete

1. Record cycle at failure (Nf)
2. Unscrew bottom platen
3. Remove bone sample
4. Discard PBS

D. Conducting Another Sample

1. Change limits (load and disp)
    a. Disp: Minimum = -0.8mm
    b. Load: Minimum = -30
2. Waveform Setup
    a. Click the Sine tab
    b. Control Channel: Load
    c. Move Type: Absolute
    d. Cyclic Parameters:
        i. Level 1 (F_min, e.g. -2.32)
        ii. Level 2 (F_max, e.g. -23.22)
    e. Frequency = 8
    f. Cycle Count = 1,000,000
    g. Start and finish parameters -- these do not have any bearing on the test EXCEPT Initial Cycles = 0
    h. Click Ok (to make sure it saves)
3. Presets: 1 = 0mm, 2 = -1N
4. Standard Timed Data→ change file name > Save
5. Apply Preset 1 (0 mm); ensure load is at 0N (if not, zero by right clicking and selecting "Auto")
6. Load bone onto bottom platen - lock into place with top platen just touching top of bone. Ensure the bone is centered on the platens in all direction.
7. Apply -1N preload
8. Lock top fixture into place
9. Fill water bath with PBS
10. Update Preset 2 to F_min
11. Click Preset 2

12. Write down reference displacement (e.g. -0.29mm)
13. Limits: check to make sure they are tight!
    a. Min load should be around -1N on top of F_max
    b. Disp min = tight! Set to be -0.3mm + reference disp (e.g. -0.6mm)
14. Standard Timed Data > Start (data collection)
15. Run > Zeroed Start
16. Record where the displacement immediately jumped to (e.g.- 0.32mm)
17. Adjust displacement minimum limit to be
    a. 10% of sample height + 'jumped to' displacement (e.g. height = 1.75mm, then we want 1.75*0.1 + 0.32 = 0.495mm ← make sure you put this in negative)

B.5 Standard Operating Procedure for analyses of bone structure with ImageJ

University of California, Berkeley
Berkeley Biomechanics Lab
Standard Operating Procedure

Analysis of Micro-CT Mouse Vertebrae Images with ImageJ

SOP, Version 1
Date: 05/01/2018

Author(s): Megan M. Pendleton & Shannon R. Emerzian
Principal Investigator: Tony M. Keaveny

Summary: This protocol outlines steps on how to find the height, minimum tissue or total area, average tissue or total area, and BV/TV of the sample from the micro-CT scans using ImageJ. Other trabecular microarchitecture parameters (i.e. Tb.N, Tb. Sp, Conn.D) were evaluated with SCANCO software by Alfred Li at the Bone Imaging Core Facility (SFVA and UCSF; PI is Prof. Wenhan Chang). The parameters used for this SCANCO analysis can be found at the bottom of the protocol. This document assumes that you have already followed the steps from another SOP referring to image processing with micro-CT, which outlines thresholding and reorientation of the original DICOM scans and saving them as a TIFF stack. Before you start these methods make sure that you have the correct software downloaded (listed below), and you know the resolution of the scans. (e.g. 10um/voxel or 20.7um/voxel).

Key Words: mechanical testing, monotonic compression, mouse, vertebrae

Materials:

- Original DICOM or TIFF stack of images from micro-CT
- Software: ImageJ or Fiji with pluggins from BoneJ; notes below
- Data collection sheets (for tracking progress)

Software Notes:

A. Fiji (which is just package of ImageJ); this must be the version that uses Java6; you can download this at the following link: https://imagej.net/Fiji/Downloads install the Java6 "Life-Line" version of Fiji. This is because the BoneJ pluggin is only compatible with Java6. They are working on upgrading this, so Java8 or another version may work in the future.
B. Java6; you must have Java6 SRE version downloaded on your computer. Here is the link to where you can download it from: http://www.oracle.com/technetwork/java/javase/downloads/java-archive-downloads-javase6-419409.html , (Look under the second heading called "Java SE Runtime Environment 6u45" which means version 6, update 45. And if you have a PC, get the "jre-6u45-windows-x64.exe") and if you need additional instructions on how to download it these are found here: https://it.uoregon.edu/reverting-java-windows you will need to make a Oracle account.
C. Save the BoneJ.jar to the pluggins folder in Fiji, this can be found here: http://bonej.org/
D. Even with the 3D Viewer pluggin that is automatically included when you download Fiji, you still need to download Java 3D 1.5.1 for the BoneJ to work. This can be found here: http://www.oracle.com/technetwork/java/javasebusiness/downloads/java-archive-downloads-java-client-419417.html (for PC users download the Java3d-1_5_1-windows-amd64.exe under the Java 3D 1.5.1 heading). Again use the second link shown in step 2 above, if you need more explicit help on successfully downloading the .exe file.

Steps:

1. Heights
    a. Open Fiji (aka ImageJ)
    b. File >>Import>>Image Sequence>>(go to folder with specimen TIFF files)>>(double click on first image)>>Click OK
    c. Note in the stack of images it shows what image you are on out of the total number of slices (e.g. 1/231). This means there are 231 slices.
    d. Multiply the resolution by the number of slices and convert to mm to find the specimen height. (e.g. 10um x 231 slices x .001 = 2.31mm)
2. Tissue Area (min or average)
    a. Open Fiji (aka ImageJ)
    b. File >>Import>>Image Sequence>>(go to folder with specimen TIFF files)>>(double click on first image)>>Click OK
    c. Ctrl+Shift+i to invert the image colors (for some reason, the area function only seems to work on black particles)>>Click Yes
    d. Analyze>>Analyze Particles>>(do not change anything, as shown below)>>Click OK>>Click Yes

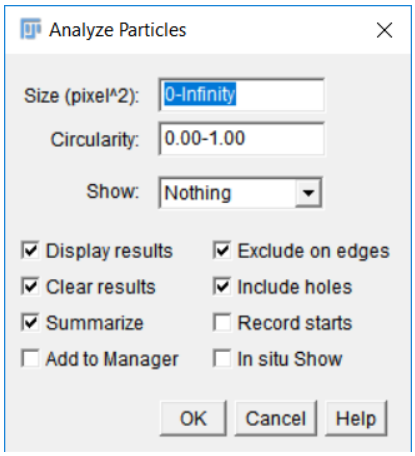

Figure B.23 – Analyze Particles window from ImageJ

e. The following table will be populated Click File>>Select All>>File>>Copy

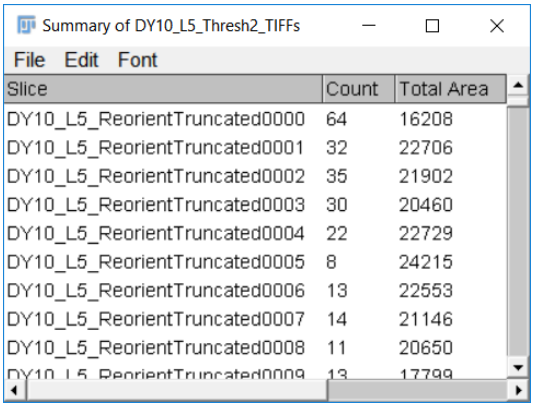

Slice	Count	Total Area
DY10_L5_ReorientTruncated0000	64	16208
DY10_L5_ReorientTruncated0001	32	22706
DY10_L5_ReorientTruncated0002	35	21902
DY10_L5_ReorientTruncated0003	30	20460
DY10_L5_ReorientTruncated0004	22	22729
DY10_L5_ReorientTruncated0005	8	24215
DY10_L5_ReorientTruncated0006	13	22553
DY10_L5_ReorientTruncated0007	14	21146
DY10_L5_ReorientTruncated0008	11	20650
DY10_L5_ReorientTruncated0009	13	17799

Figure B.24 – Table containing the total area per image listed in pixels.

f. Paste this table in an excel sheet make sure to put a heading in the first line. The column listed as "Total Area" is really the area of black pixels per slice. The percentage area column is calculated from taking the number and dividing it by the total pixels in image, which can be found by looking at the image stack and multiplying the width x height (428*399 = 170772).

g. Use excel to find the minimum of the total area column and average of the total area column and convert these to mm again depending on the resolution of the scan. Be careful that the minimum area is not the first or last slice in the stack just because of an image processing error.

3. Total Areas
   a. Open Fiji (aka ImageJ)
   b. File >>Import>>Image Sequence>>(go to folder with specimen TIFF files)>>(double click on first image)>>Click OK

c. Plugins>>BoneJ>>Fit Ellipsoid>>Click OK (this brings up the ROI manager)

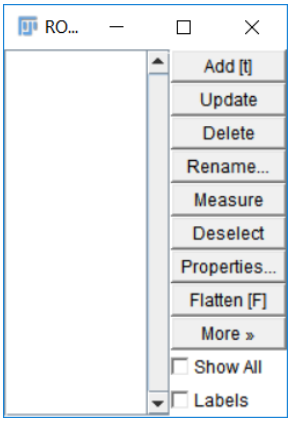

Figure B.25 – RIO Manager from BoneJ pluggin

d. Click on the "Freehand selection" from the toolbar, it looks like a weird heart shape
e. Use this tool to draw an outline around just the bone as best you can and click "Add" in the ROI manager (YOU MUST DO THIS FOR THE FIRST & LAST IMAGE)
f. Scroll ~5 to 10 slices until the image changes and draw a new boundary, Click "Add", continue to do this for the whole stack.
g. In the ROI manager, click "More">>"Interpolate ROIs" (this will add additional boundaries for all of the slices between the ones that you drew
h. In the ROI manager, click "More">>"Fill" (this will fill in all of the slices with white)
i. Save this stack as a TIFF or BMPs for example D12.7_L5_ColoredIn (now you are going to follow the same directions as in the section for "Tissue Area" starting at letter 'c'. (also listed below)
j. Ctrl+Shift+i to invert the image colors (for some reason, the area function only seems to work on black particles)>>Click Yes
k. Analyze>>Analyze Particles>>(do not change anything, as shown in **Figure B.9**)>>Click OK>>Click Yes
l. A summary table (see **Figure B.10**) will be populated Click File>>Select All>>File>>Copy
m. Paste this table in an excel sheet make sure to put a heading in the first line. The column listed as "Total Area" is really the area of black pixels per slice. The percentage area column is calculated from taking the number and dividing it by the total pixels in image, which can be found by looking at the image stack and multiplying the width x height (428*399 = 170772).
n. Use excel to find the minimum of the total area column and average of the total area column and convert these to mm again depending on the resolution of the

scan. Be careful that the minimum area is not the first or last slice in the stack just because of an image processing error.

4. BV/TV
    a. Beginning note: if the softwares listed above are not installed the BoneJ pluggin will not work, and generating BV/TV values will not be possible.
    b. Open Fiji (aka ImageJ)
    c. File >>Import>>Image Sequence>>(go to folder with specimen TIFF files)>>(double click on first image)>>Click OK
    d. Plugins>>BoneJ>>Fit Ellipsoid>>Click OK (this brings up the ROI manager)
    e. Click on the "Freehand selection" from the toolbar, it looks like a weird heart shape
    f. Use this tool to draw an outline around just the bone as best you can and click "Add" in the ROI manager
    g. Scroll ~5 to 10 slices until the image changes and draw a new boundary, Click "Add", continue to do this for the whole stack.
    h. In the ROI manager, click More>>Interpolate ROIs (this will add additional boundaries for all of the slices between the ones that you drew
    i. Plugins>>BoneJ>>Volume Fraction>>Click OK (this will give you the BV/TV value to record) Note that the higher the resolution is on the stacks, the more accurate this value is going to be.

Evaluation of trabecular microarchitecture parameters via SCANCO software are listed below:

- Software: Scanco Medical µCT Evaluation Program v6.5
- Analysis: trabecular evaluation of vertebral body
- Evaluation script: lower threshold of 300, Gaussian sigma 0.5, Gaussian support 2
- Script file (if available): 31

B.6 Standard Operating Procedure for *ex vivo* irradiation at LBNL

University of California, Berkeley
Berkeley Biomechanics Lab
Standard Operating Procedure

Ex vivo Irradiation at Lawrence Berkeley National Labs

SOP, Version 1
Date: 09/08/2016

Author(s): Megan M. Pendleton & Shannon R. Emerzian
Principal Investigator: Tony M. Keaveny

Summary: This protocol outlines the steps used to irradiate the *ex vivo* vertebrae with x-rays at LBNL. Contact Dula Parkinson at LBNL who runs line 8.3.2 at the Advanced Light Source in building 6. This is a Synchrotron-based Hard X-ray Micro-Tomography beamline, which is typically used for imaging (i.e. nano-CT), but we have been using it for *ex vivo* irradiation of bone for high doses which would take too long on a lower energy beam.

Key Words: ionizing radiation, x-ray, *ex vivo*, mouse vertebrae

Materials (for 3 samples):

- Bone sample (used for mechanical and biochemical testing)
- Plenty of ice packs in styrofoam container to keep cold
- Kapton Tape
- PBS 1X
- Disposable transfer pipettes
- Gauze
- Scissors
- Gloves
- Forceps (sharp-tipped)
- Blue pad for clean surface

Steps:

1. Calculate dose rate and beam time needed to achieve dose
    a. Parameters used for dose rate calculation
        i. Bone thickness: $l = 2.5$ mm or 0.25 cm
        ii. Bone density: $\rho = 1.85$ g/cm^3
        iii. Energy of beam: $E = 20$ keV
        iv. Flux Density: $\varphi = 83{,}000$
        v. Area of beam (actually bone): $a =$ (0.25 cm)(0.2 cm) = 0.05 cm2 = 5,000,000 μm^2
        vi. Mass of bone: $m = 10$ mg = 0.00001 kg
        vii. Mass attenuation coefficient for bone @ 20 keV: $\mu = 4$ cm2/g
    b. Equations needed to calculate dose rate with values
        i. $T = I/I_0 = e^{(-\mu\rho l)} = e^{(-4*1.85*0.25)} = 0.1572$
        This is an ideal calculation of T, however it was measured on the beam with a sample in place to be 0.9, meaning most of the photons are passing through the material, likely because it is mostly cancellous tissue and empty space, instead of bone. Therefore, for the remainder of the equations we assumed T to equal 0.9
        ii. $A = 1 - T = 0.1$
        iii. $E_\rho = \varphi E(1.6 * 10^{-19}) = (83000)(20000)(1.6 * 10^{-19}) = 2.66 * 10^{-10}$ J/(sec*μm^2)

iv. $\dot{D} = \left(AE_{\rho}\rho a/m\right) = (0.1)(2.66 * 10^{-10})(5000000)/0.00001 = 13.28$ Gy/sec

c. Use dose rate to calculate time to reach full dose
   i. e.g. to reach 50,000 Gy
   ii. 50000/13.28 = 3765 sec = 62.75 min
   iii. Note: this would not be achievable in "two-bunch" mode for the sterilization doses (1000s of Gy). psi changes to 5800 and the dose rate is only 0.925 Gy/sec which would take 13.9 hrs to achieve 50,000 Gy!

2. Thaw specimens to room temperature and prepare them for the beamline, try and time this so that the specimen spend as little time at room temperature as possible

3. Align specimens in a row on a small, square piece of gauze (a line of 5-6 vertebra), get them as straight as possible

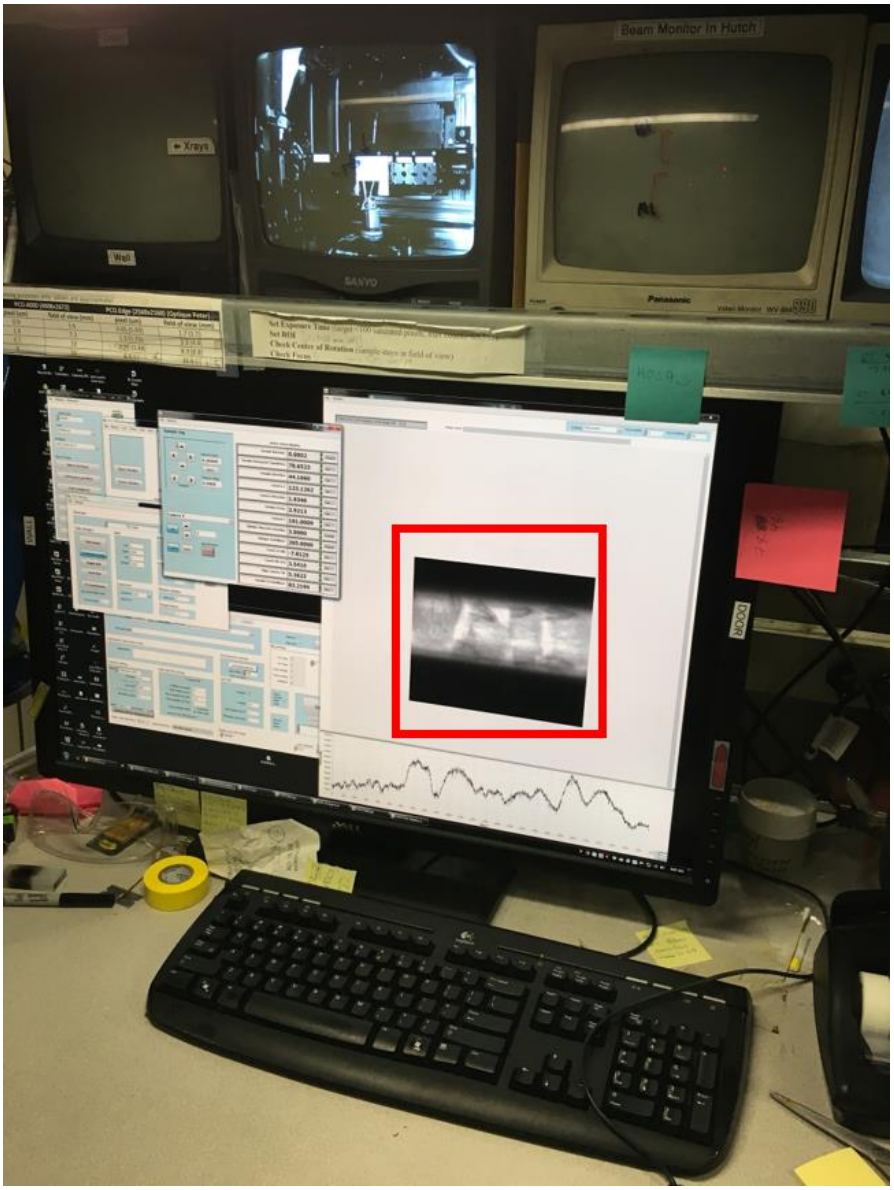

Figure B.26 – Operating station for beamline 8.3.2 at LNBL ALS. Row of specimens are being exposed to x-rays which is visible on the computer screen (boxed in red).

4. Apply PBS and wrap/fold gauze to cover specimen, re-apply more PBS
5. Tape the gauze to an index card or post-it note (index cards work better because they are more rigid). Make note on the card about what order the samples are in
6. Place index card in the beam fixture, with a binder clip. Note: to make the process go faster for the following samples, mark where the binder clip should be held and where the gauze is positioned, this will make placing it back into the beam line faster the next round

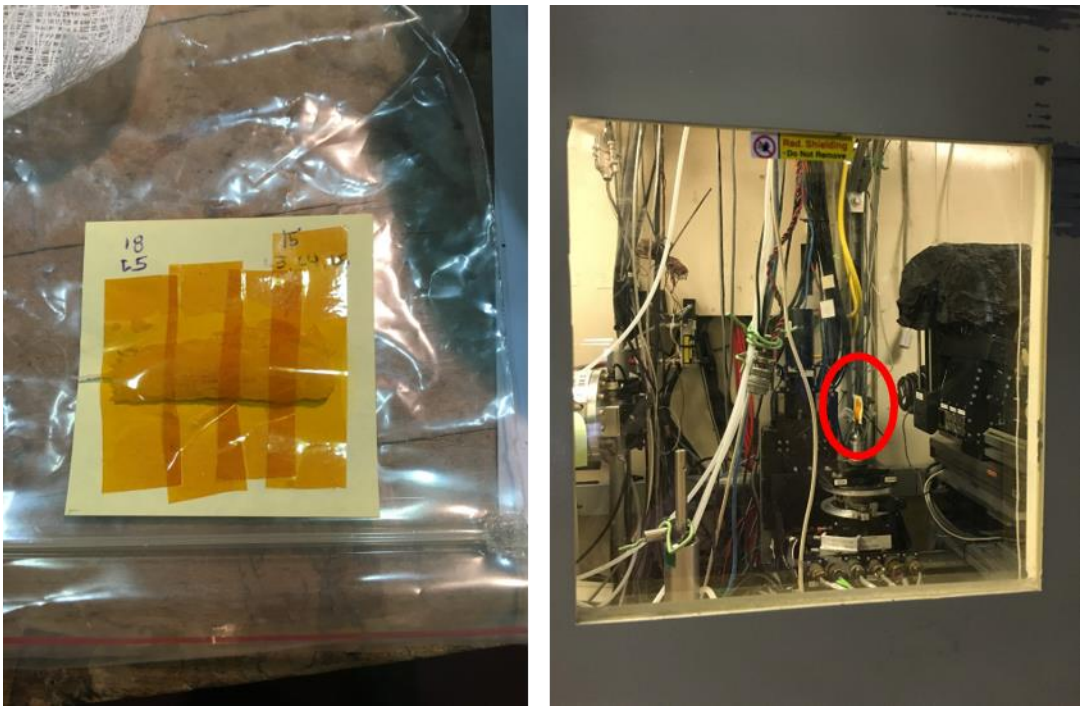

Figure B.27 – (Left) Row of five to six specimens are wrapped in saline-soaked gauze and taped to sticky note (index card works best). (Right) Sticky note (highlighted in red) is mounted upright within x-ray beam with a binder clip connected to the mounting fixture inside hutch.

7. Follow protocol for turning on beam (you can raise an aluminum shield in place to block most of the photons, but still be able to see them enough to align the specimen)
8. Align the specimen in the middle of the beam. Note: If they are not in a row, you may have to try once again to align them in a row.
9. Remember to remove the aluminum if it was put in place
10. Set timer and leave in beam for calculated time
11. Carefully remove specimens, place in fresh gauze, apply PBS (damp gauze, do not soak!), and put back on ice packs
12. These will then go back into the -20C freezer until micro-CT. Be sure to remind the person conducting micro-CT to be gentle with tissue.

For *ex vivo* irradiation conducted at NASA (5 Gy), the beam area is much larger. Therefore, all specimens at RT were wrapped in saline-soaked gauze and taped with kapton tape to box cover.

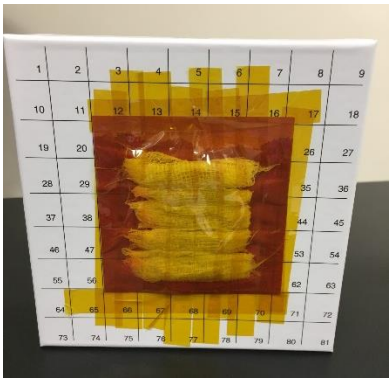

Figure B.28 – Specimens prepared for *ex vivo* irradiation at NASA ARC in saline-soaked gauze and taped to box lid with Kapton tape. Specs on this ^{137}Cs gamma-radiator can be found in Chapter 3. The results presented in Chapter 4 were only irradiated with x-ray at LBNL.

B.7 Standard Operating Procedure for collagen fragmentation assay with Bioanalyzer

University of California, Berkeley
Berkeley Biomechanics Lab
Standard Operating Procedure

Collagen Fragmentation Bioanalyzer Assay

SOP, Version 1
Date: 08/31/2017

Author(s): Megan M. Pendleton
Principal Investigator: Tony M. Keaveny

Summary: This assay measures the molecular weight of collagen using Agilent Technologies Bioanalyzer. The bioanalyzer is an automated form of electrophoresis, so instead of a gel, we load protein onto a chip. This SOP outlines how to extract the collagen from bone and briefly discusses how to prepare and run the bioanalyzer chip, with more details provided in the Agilent Protein 230 Kit manual. Note: this protocol does not have a procedure for evaluating the total collagen in each sample. Ideally this step should be added in the future, and could be accomplished with a hydroxyproline assay kit. (Materials and equipment commonly found in a wetlab are not listed, so be sure to read protocol carefully to ensure you have the necessary equipment in your lab.)

Key Words: collagen fragmentation, molecular weight, bioanalyzer, electrophoresis

Acknowledgements: Dr. Thomas Willett and Dr. Brianne Burton for providing an SDS-PAGE protocol to work from, and Dr. Elumalai Rangasamy from Agilent Technologies for training on the bioanalyzer.

Materials:

- Bone (e.g. L3 mouse vertebrae will provide enough collagen to run this assay)
- EDTA (2Na): Sigma Aldrich #E5134-500G
- EDTA (4Na): Sigma Aldrich #ED4SS-500G
- DI water
- Chloroform
- Methanol
- Liquid nitrogen
- 0.5 M acetic acid
- Pepsin from porcine gastric mucosa: Sigma Aldrich #P6887-250MG
- 5M NaOH
- pH paper
- 1M HCl
- NaCl
- 1X PBS
- Agilent Technologies Protein 230 kit (including reagents and chips) #5067-1517
- Rat Tail Collagen standard: Sigma Aldrich #C7661-25MG

Equipment:

- Desiccator
- Small ceramic mortar and pestle
- Lyophilizer (VirTis AdVantage Plus Benchtop Freeze Dryer XL Model, SP Scientific, Stone Ridge, NY)
- Rocker
- Bioanalyzer (set-up to run protein, not RNA)

Steps:

1. Demineralize bone tissue in 0.5M EDTA for 3 weeks at room temperature. Individual vertebrae are housed in 1.5 mL centrifuge tubes with 1 mL of EDTA solution added to each tube and changed every 2-3 days. Note: After demineralization, if we were not ready to begin collagen extraction, the specimen were rinsed thoroughly with 1X PBS and stored in saline-damp gauze at -20C until we were ready to continue. Note: Times can vary for demineralization on different size bones, so you can check via imaging (i.e. x-ray) or by poking the tissue with a 21-gauge needle to see if it goes through easily.
    a. Depending on the number of samples, and accounting for changing the solution every couple of days, calculate the total amount of EDTA to make (e.g. 1 L)
    b. Calculate grams of salt, two salts are needed: EDTA (2Na) & EDTA (4Na)
        i. Molecular weight of EDTA (2Na) is 372.24 g/mol
        ii. (372.24 g/mol)(0.25 mol/L) = 93.06 g/L
        iii. Molecular weight of EDTA (4Na) is 416.20 g/mol
        iv. (416.20 g/mol)(0.25 mol/L) = 104.05 g/L

v. Remember to scale these amounts if you are making less than 1 L

c. Weigh out the grams of salts calculated in weigh boats.
d. In a larger enough beaker, add 600 mL of DI water. Place beaker on a stir plate with a magnetic stir bar.
e. Add salts while stirring and then add remaining DI water needed to reach 1L.
f. Stir until salts are completely dissolved ~30 min (when solution no longer looks cloudy) and check that pH is between 7.4 and 8.0.

2. Defat specimen overnight for 24 hours. Soak in 1:1 chloroform:methanol solution
    a. We used 1.5 mL centrifuge tubes. Note that these chemicals will dissolve some plastics, so it is recommended to use a glass pipette tips and a glass waste container. The microcentrifuge tubes will be fine for the 24 hrs needed.
3. Soak specimen in 100% methanol for 1 hr.
    a. Also used 1.5 mL tubes
    b. After 1 hr, empty methanol into appropriate waste containers
4. Place specimen within their tubes (caps open) into desiccator, under the hood and allow to dry overnight.

Figure B.29 – Specimens arranged inside desiccator with microcentrifuge tube lids open such that specimens can dry.

5. Crush bone specimen into fine powder using small ceramic mortar and pestle. Note: Do not use the NASA Ames “bone crusher”. This will only work for larger specimen and does not get a fine enough powder for this assay.
    a. Label 1.5 mL tubes and weigh them
    b. Place mortar and pestle into container and pour N2 all over to get them very cold (N2 has a hard time evaporating when the mortar is cold, this is how you can tell)
    c. Drop specimen into N2 to flash freeze, wait ~30 sec
    d. Crush specimen into powder (looks brownish)
    e. Use a small spatula to carefully scrape powder into the labeled tube
    f. Cover the open cap tube with parafilm and poke with 5 evenly spaced tiny holes using sharp-tipped forceps
    g. Measure weight of tubes after process to get an approximate powder mass per tube

Figure B.30 – Bone crushing set-up. (Left) Containment ice bucket housing the mortar and pestle with liquid nitrogen to keep cold. (Middle) Mortar and pestle with crushed sample highlighted in red. (Right) Bone powder scraped into microcentrifuge tube using spatula.

6. Lyophilize (i.e. freeze-dry) bone powder, process takes ~25 hrs in total
    a. Place tubes in a plastic microcentrifuge tube rack
    b. Put rack(s) in the lyophilizer (VirTis AdVantage Plus Benchtop Freeze Dryer XL Model, SP Scientific, Stone Ridge, NY). At NASA Ames this is located in Sergio Santa Maria's Lab Room 112
    c. "Recipe 01" includes the following steps in order: -38C for 180 min; -38C at 120 mTorr for 90 min; -20C at 770 mTorr for 900 min; -10C at 930 mTorr for 270 min; 23C at 120 mTorr for 55 min
7. Solubilize (i.e. digest) bone powder for a total of 72 hours (24 @ RT and 48 @ 4C) Note: We typically use 1 mg of pepsin per 10 mg of bone. Most 1.5mL tubes had
    a. Make 0.5M acetic acid, make sure to perform under the hood
        i. Calculate needed volume of 0.5 M acetic acid
        ii. (60 samples)(1.5mL) = 90 mLs; usually make extra ~100mLs
        iii. Calculate volume of pure glacial acetic acid needed to make the solution
        iv. Known: MW is 60.05 g/mol; for 0.5M multiply *0.5 = 30.025 g/mol
        v. Known: Density 1.05 g/cm3
        vi. Unknown: Volume = mass/density (30.025/1.05) = 28.6 cm3 or 28.6 mLs (this is the amount you would add to 1 L)
        vii. Scaling this for 100 mLs is 2.86 mLs
    b. After making the 0.5 M acetic acid, add 60 mg of pepsin to solution in a beaker and stir on plate for 2-4 hours until pepsin is dissolved Note: The mass will change depending on the amount of bone. (e.g. most powder samples weighed between 5-16 g, therefore we used 1 g of pepsin per sample). 60 g is calculate for 90 mLs of acetic acid, this would be slightly different for the 100 mLs.
    c. Add 1.5 mLs of solution to each tube
    d. Tape tubes to rocker
    e. 24 hours on rocker at room temperature (the digestion will occur more quickly at higher temperatures, but you risk bacterial growth)
    f. 48 hours on rocker at 4C (it is usually best to err on the side of more or longer digestion times)

Figure B.31 – Specimens taped to rocker for digestion and precipitation steps.

8. Neutralize the digestion reaction with 5M NaOH to pH between 6 to 8; Note: If comfortable using phenol red as an indicator try this to use the color to tell pH (must have used clear tubes). pH paper will also work, but will take a little more time. pH paper worked best for me.
    a. Add ~140 µL 5 M NaOH to the 1.5mL tube with pepsin solution
    b. Vortex to mix
    c. Add 10 µL to pH strip (cut lengthwise in half to conserve paper) to check pH is between 6 to 8.
    d. If you overshoot and are basic, add some 1M HCl ~15 µL at a time to try and reach a pH of 6 to 8
    e. Spin down tubes for 30 min at 13,000 RPM to collect the insoluble collagen/tissue in a pellet
    f. Transfer supernatant (liquid part) to a new tube, this contains the soluble collagen, usually about 1.3 to 1.5 mLs of supernatant liquid; Note: ideally you would weigh tubes prior to adding the supernatant here, so you can later measure the weight of preserved collagen, but this was difficult to do because much of the weight also comes from liquid left on the pellet. It would be best to use a hydroxyproline assay to estimate the total collagen extracted from each sample.
    g. Discard pellet
9. Precipitate out soluble collagen using NaCl
    a. Add 2M NaCl to new tubes
        i. Either make bulk 2M NaCl, or directly add salt to tubes; e.g. below
        ii. (2 mol/L)(58.44 g/mol) = 116.88 g/L or 0.1169 g/mL
        iii. 0.1169 g NaCl per 1 mL solution, solve for g needed in 1.5 mL solution
        iv. Measure mass of salt and add to tube
        v. Vortex to dissolve; Note: more than 0.36 g NaCl per 1 mL at RT will not dissolve, see solubility tables online for NaCl
    b. Tape tubes to rocker and rock at 4C for 24 hrs
10. Recover precipitate that contains the extracted collagen
    a. Spin samples for 30 min at 13,000 RPM

b. Look carefully for the pellet at the bottom of the tube; Note: Sometimes this is difficult to see. Look at the tube under a ceiling light and try to find a cloudy substance at the bottom rim of the tube, this is the pellet.

Figure B.32 – Pellet is sometimes difficult to identify. Hold sample under light and look for cloudy substance at the bottom rim of microcentrifuge tube. Black arrow drawn on tube to show where the pellet is located.

c. Remove remaining liquid with pipette and discard
d. Add 200 µL of 0.5 M acetic acid to resuspend the pellet in solution. Sometimes using the pipette to aspirate will be sufficient, but vortexing often was necessary. Note: 200 µL depends on the mass of the pellet; we assumed a pellet of 2 mg, adjust accordingly.

11. Lyophilize
    a. Cover tube caps with parafilm and poke 5 tiny holes with sharp-tipped forceps
    b. See Step 6 to repeat procedures; process takes ~25 hrs
    c. At this point you can freeze the tubes at -20C until you are ready to run them on the bioanalyzer.
12. Prepare the sample solutions to run on the bioanalyzer (for further details or clarification on the following steps, refer to the Agilent Protein 230 Kit manual)
    a. Prepare the Gel-Dye mix
        i. Allow dye and gel matrix to reach RT ~30 min; protect from sunlight by wrapping vial in aluminum foil
        ii. Vortex and spin dye
        iii. Add 25 µL of dye directly to tube of matrix (tube contains 650 µL of gel matrix)
        iv. Vortex well ~10sec and Spin ~15sec to ensure solution is fully mixed
    b. Prepare the Destaining Solution
        i. Transfer 650 µL (all) of gel matrix to spin filter tube
        ii. Spin for 15 minutes at RT at 2500 Gs or 5200 RPM
    c. Prepare the Denaturing Solution
        i. Thaw one of the sample buffer tubes from kit (should be at RT for 10 min)
        ii. Vortex and spin
        iii. Add 7 µL of 1M Dithiothreitol (DTT) solution to the original 200 µL vial of sample buffer
        iv. Vortex and spin to mix
    d. Solubilize Collagen extract from lyophilized state

i. Add 200 µL of 1X PBS to each tube (even if some of these had a little more bone mass than others)
ii. Vortex ~15 sec (did not need to spin)
iii. Put in 50C water bath for 20-30 min (this will help the collagen go into solution, proteins will sometimes look "cloudy" or "clumpy" and it needs some time and warmth to dissolve) Use tube racks that float to place the tubes in the water bath without tipping over

e. Prepare Samples, Standard, and Ladder; Note: for many samples this is easiest to do in a PCR plate with many 0.5 mL tubes together, but double check that this plate will fit into the heating block you plan to use! Or else you will have to transfer them.
i. Organize samples in an order you understand for loading the chips
ii. Transfer 2 µL of denaturing solution into all of the 0.5 mL tubes needed
iii. Transfer 4 µL of sample solution into its respective tube
iv. Transfer 4 µL of standard (Rat Tail Collagen) into 2 to 3 tubes, depending on how many chips you are running, each chip will need a standard
v. Add 6 µL of ladder solution to 2 tubes as well
vi. Each tube should have a total of 6 µL
vii. Important Notes: Put the pipette tip all the way at the bottom of the tube and release liquid there, avoid getting solution on the wall of the tube. Also, use the pipette to GENTLY mix the denaturing solution and sample solutions. The denaturing solution will generate bubbles if mixed vigorously and this will cause problems when running on the chip. Do NOT vortex to mix.

f. Heating block to denature collagen
i. Put PCR rack in heating block for 5 min at 95C; Note: be sure to cover the tubes or some evaporation could occur, and avoid using an aluminum sticker for capping because they are difficult to remove. Also, do not heat for more than 5 min
ii. Cool for 10 sec
iii. Spin for 15 sec

g. Add DI water to samples
i. Add 84 µL of DI water to samples/standard/ladder (helps to use a multi-tip pipette)
ii. Vortex (or simply mix solution with the pipette, do this several times but gently)

13. Prepare the chip (for further details or clarification on the following steps, refer to the Agilent Protein 230 Kit manual)
a. Place chip in priming station (stage)
b. Add 12 µL of gel-dye mix to first well in the top-right corner
c. Pressurize using syringe
i. Ensure syringe starts at 1mL with plunger up
ii. Close stage until you hear a click
iii. Press plunger down until it clips (the silver level will hold position)
iv. Wait 1 min
v. Release plunger (pull up on silver lever)

vi. Wait 10 sec for plunger to rise, finish by pulling it back to 1 mL mark
vii. Open stage

d. Add 12 µL of gel-dye mix to three other wells marked "G"
e. Add 6 µL of the appropriate samples to wells #1-9
f. Add 6 µL of rat tail collagen standard to well #10
g. Add 6 µL of ladder
h. Important Note: When adding these solutions to the well, place pipette tip at the bottom of well, not on the side

14. Run chip in bioanalyzer
    a. Place chip in bioanalyzer
    b. Close lid
    c. Click on Assay Protein 230
    d. Click Start, do not open lid until green light quits blinking, indicating the test is complete
    e. Place a chip with cleaning water in the wells into the bioanalyzer in between each run to clean the electrode tips. Add chip, close lid, wait 10 sec, and remove.
15. Analyze using "2100 Expert Software"
    a. Need to set the upper and lower bounds, see Agilent Technologies manual for further help with analysis

B.8 Engineering Drawing for 3D-printed fixture for specimen preparation of mouse vertebra

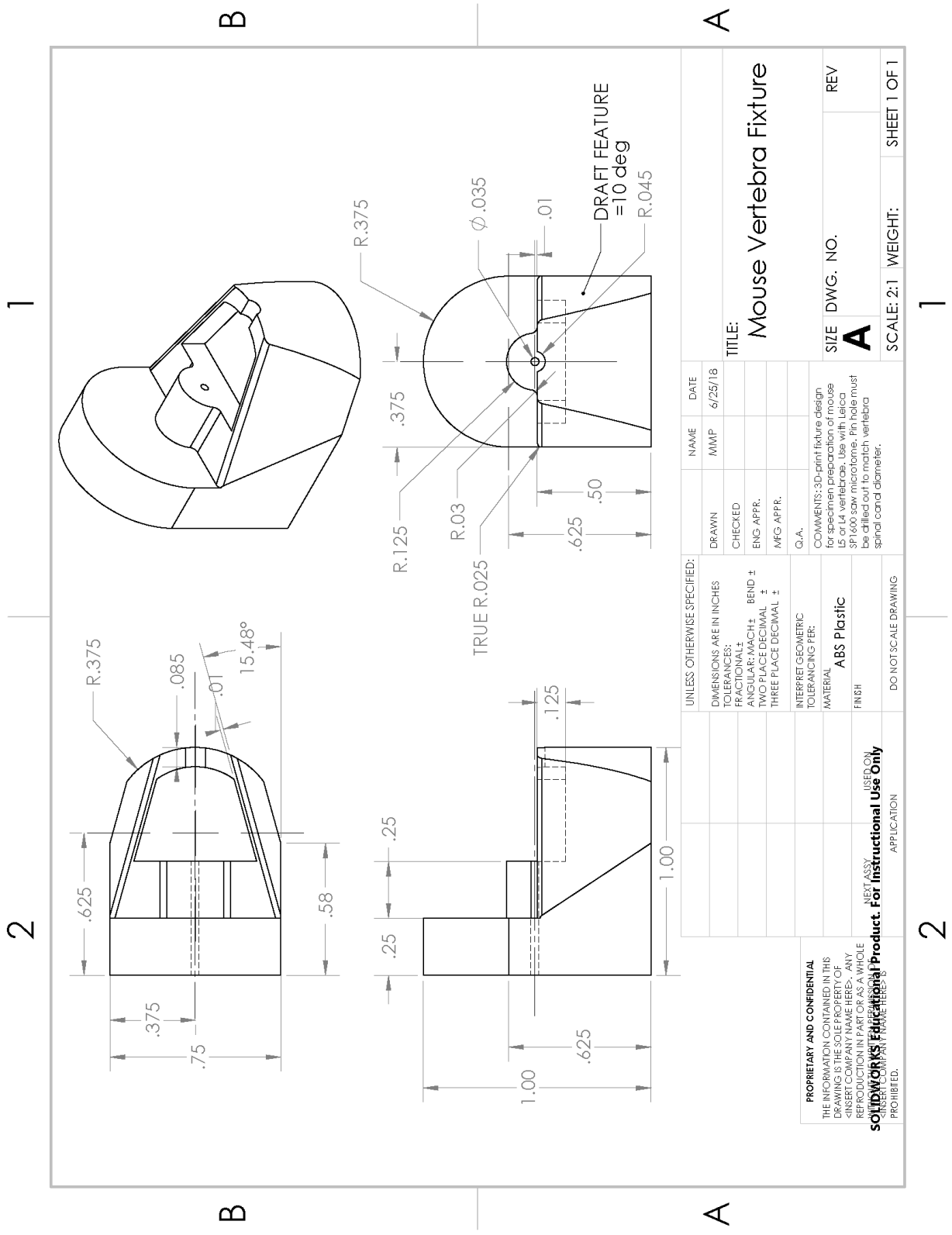

B.9 Engineering Drawing for top-half of spherically-seated upper platen

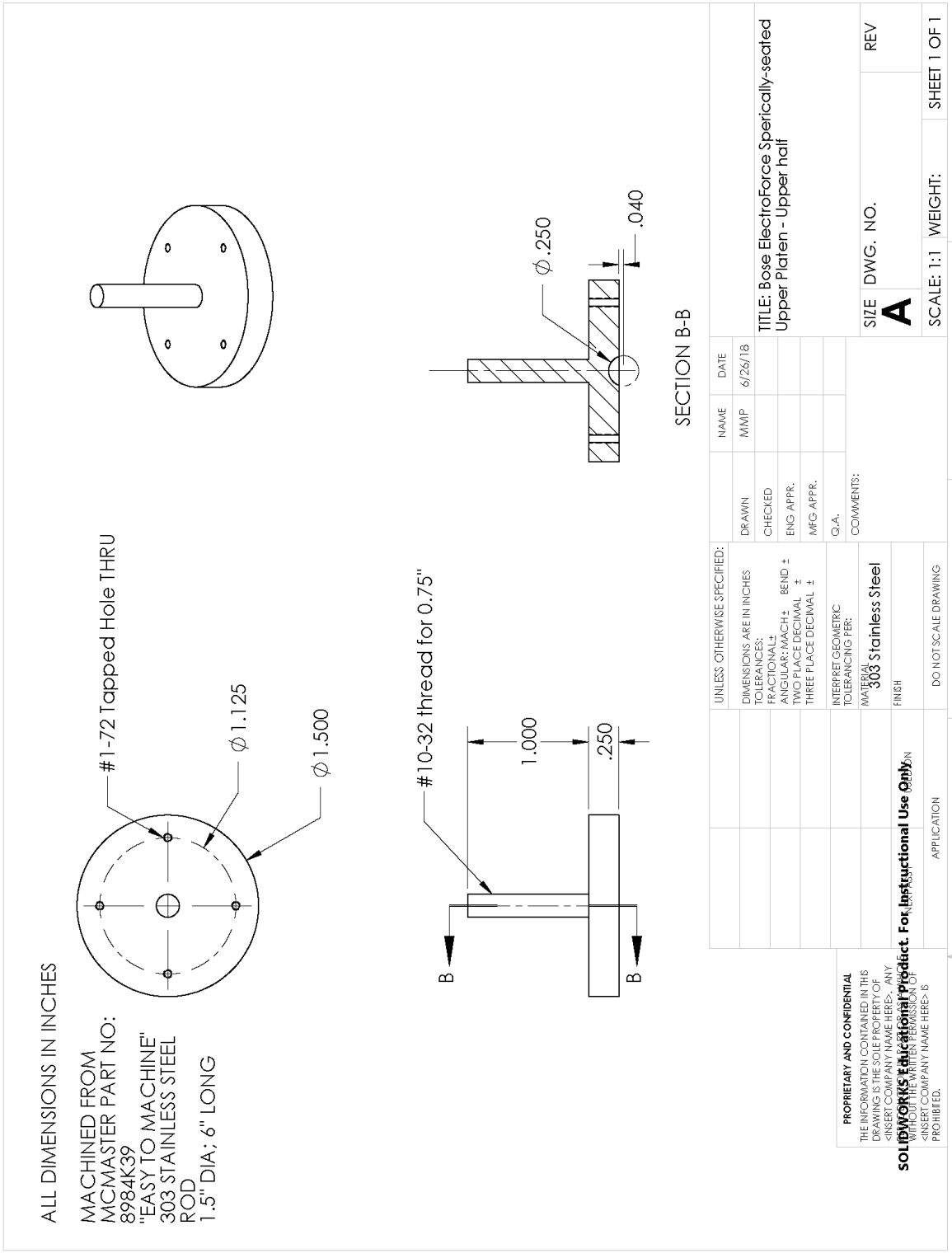

B.10 Engineering Drawing for bottom-half of spherically-seated upper platen

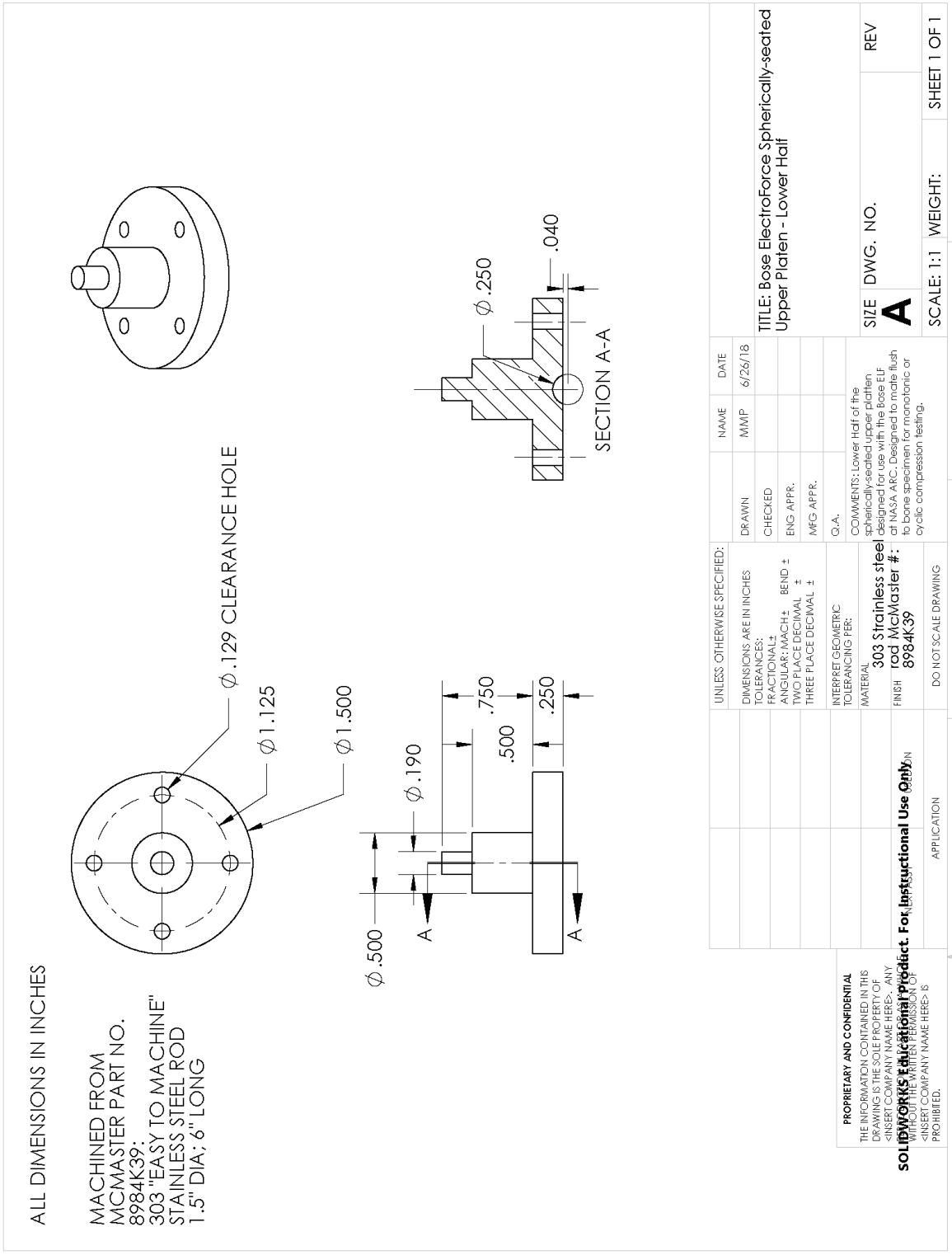

B.11 Engineering Drawing for lower platen

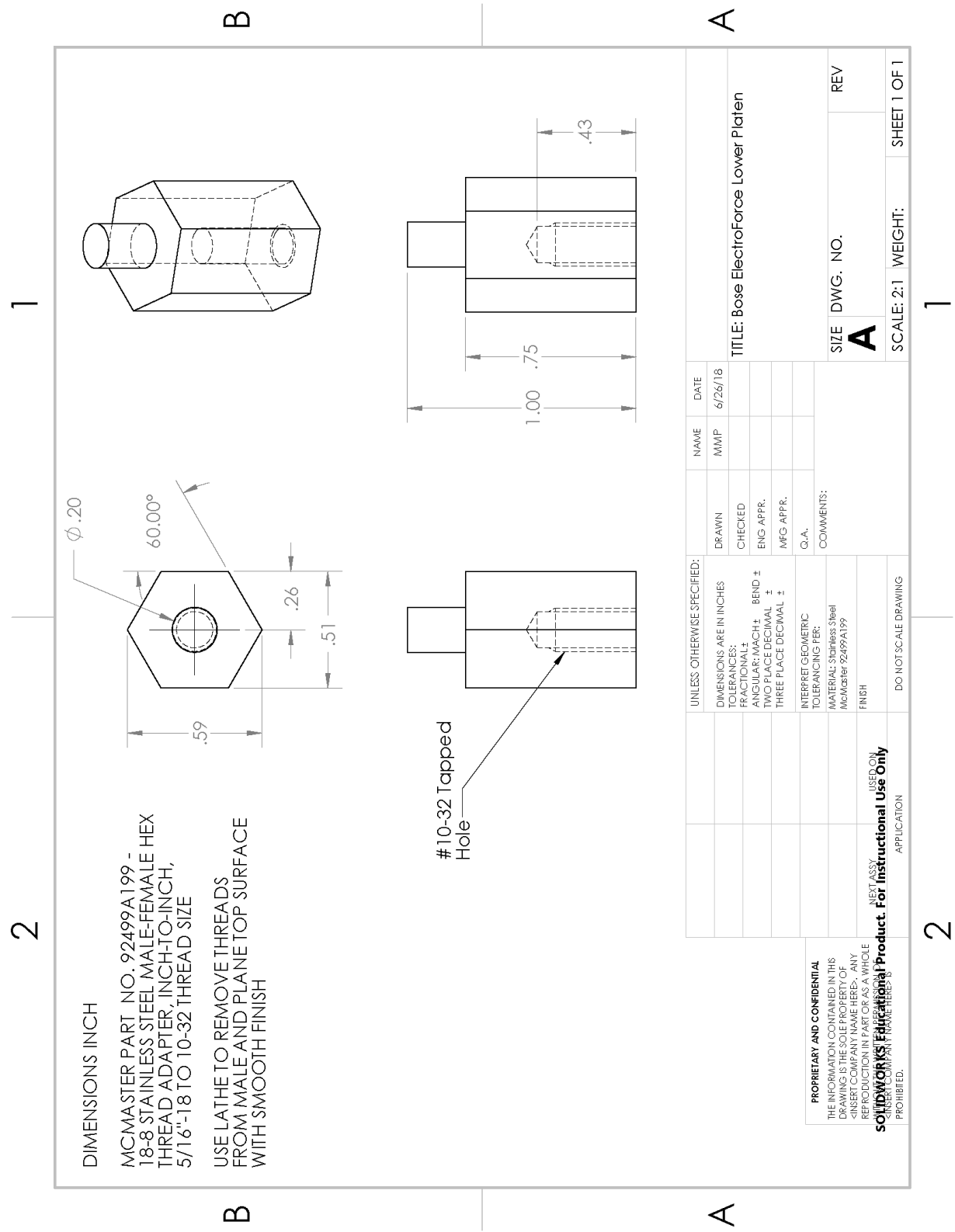

B.12 Assembly Drawing for upper and lower platens

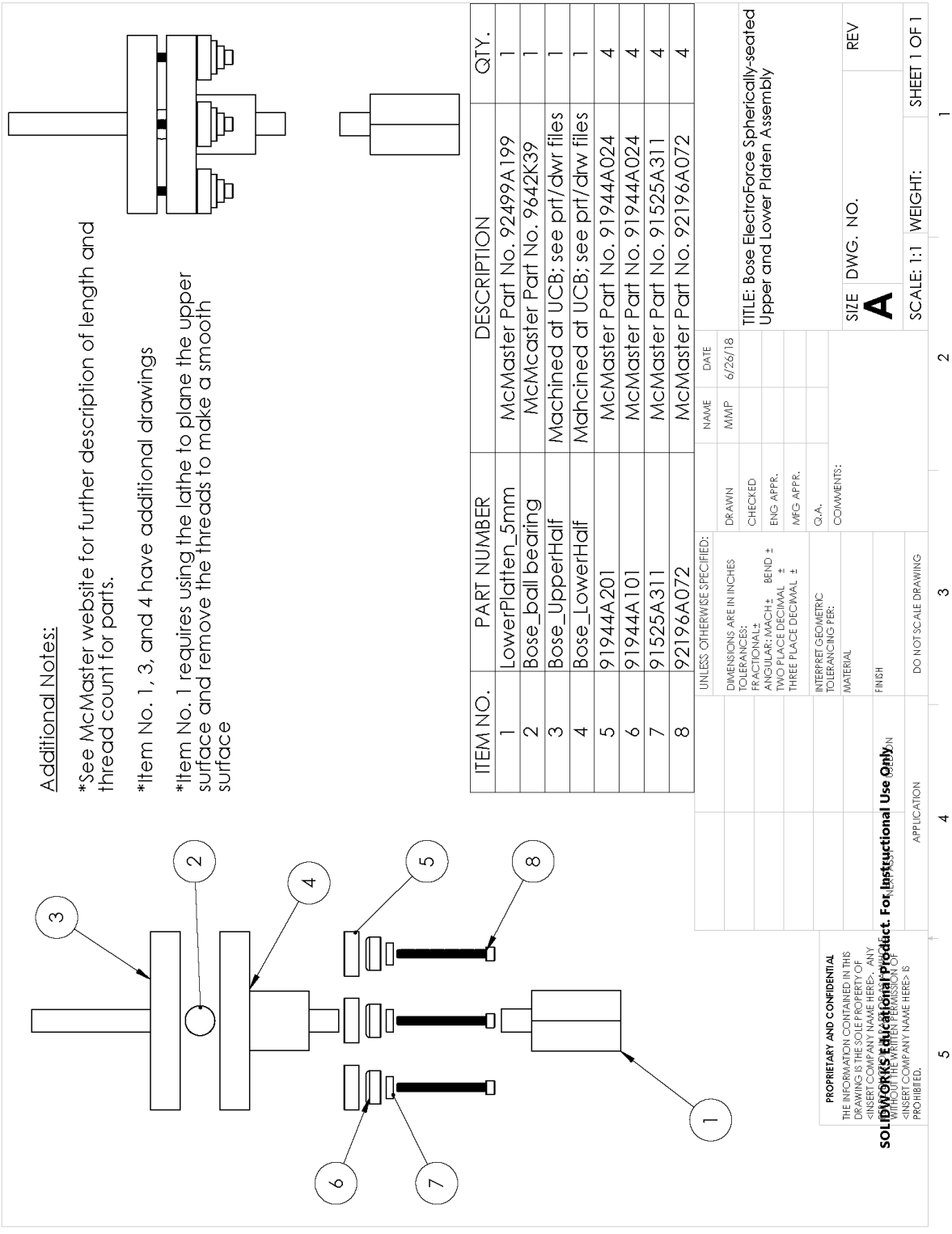

B.13 Engineering Drawing for saline-water bath